

DRL No. 216  
DRD No. SE-4

DOE/JPL-956831-86/1  
9950-1232

ARCO Solar, Inc.

Final Report

PULSED EXCIMER LASER PROCESSING  
FOR COST-EFFECTIVE SOLAR CELLS

JPL Contract No. 956831

Reporting Period: May 1984 - December 1985

Prepared for

California Institute of Technology  
Jet Propulsion Laboratory  
4800 Oak Grove Drive  
Pasadena, California 91109

Submitted by

ARCO Solar, Inc.  
P. O. Box 2105  
Chatsworth, California 91313

(NASA-CR-180528) PULSED EXCIMER LASER  
PROCESSING FOR COST-EFFECTIVE SOLAR CELLS  
Final Report, May 1984 - Dec. 1985 (ARCO  
Solar, Inc.) 143 p

CSCL 10A

N87-21413

Unclas  
G3/44 43559

1N-44

69374

p. 143

DRL No. 216  
DRD No. SE-4


DOE/JPL 956831  
Distribution Category UC-63

PULSED EXCIMER LASER PROCESSING  
FOR COST-EFFECTIVE SOLAR CELLS

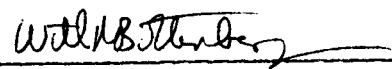
Final Report No. 1

May 1984 - December 1985

Prepared By

  
D. Wong  
Principal Investigator

Approved By

  
W. R. Bottenberg  
Program Manager

ARCO Solar, Inc.  
P. O. Box 2105  
Chatsworth, California 91313

The JPL Flat-Plate Solar Array Project is sponsored by the U.S. Department of Energy and forms part of the solar Photovoltaic Conversion Program to initiate a major effort toward the development of low-cost solar arrays. This work was performed for the Jet Propulsion Laboratory, California Institute of Technology, by agreement between NASA and DOE.

This work was performed for the Jet Propulsion Laboratory, California Institute of Technology, and was sponsored by the U.S. Department of Energy through an agreement with the National Aeronautics and Space Administration.

This report was prepared as an account of work sponsored by an agency of the United States Government. Neither the United States Government nor any agency thereof, nor any of their employees, makes any warranty, express or implied, or assumes any legal liability or responsibility for the accuracy, completeness or usefulness of any information, apparatus, product or process disclosed, or represents that its use would not infringe privately owned rights.

Reference herein to any specific commercial product, process, or service by trade name, trademark manufacturer, or otherwise, does not necessarily constitute or imply its endorsement, recommendation, or favoring by the United States Government or any agency thereof. The views and opinions of authors expressed herein do not necessarily state or reflect those of the United States Government or any agency thereof.

## ABSTRACT

The application of excimer laser in the fabrication of photovoltaic devices has been investigated extensively. Processes included junction formation, laser assisted CVD metallization, and laser assisted CVD surface passivation. Results demonstrated that implementation of junction formation by laser annealing in production is feasible because of excellent control in junction depth and quality. Both metallization and surface passivation, however, were found impractical to be considered for manufacturing at this stage.



## CONTENTS

1.0 Introduction and Summary.....	1-1
2.0 Selection of Process Sequence.....	2-1
3.0 Laser Process Experimental Details.....	3-1
3.1 Excimer Lasers.....	3-1
3.2 Laboratory Layout.....	3-1
3.3 Optical Systems for Small Scale Laser.....	3-4
3.3.1 Initial Laser Annealing Setup.....	3-4
3.3.2 Small Scale Excimer Laser with Optical Beam Homogenizer.....	3-6
3.3.3 Optical Arrangement for Metallization and Passivation Process Steps.....	3-11
3.4 Laser Diagnostics.....	3-16
3.4.1 Laser Pulse Energy Measurements.....	3-16
3.4.2 Pulse Duration and Temporal Waveforms.....	3-17
3.4.3 Spatial Intensity Distribution Measurements...	3-17
3.5 Experimental Measurements.....	3-18
3.5.1 Junction Formation by Excimer Laser Annealing.....	3-19
3.5.1.1 Laser Pulse Duration and Waveform.....	3-20
3.5.1.2 Spatial Distribution of Intensity.....	3-23
3.5.1.3 Laser Repeatability.....	3-30
3.5.1.4 Wafer Processing.....	3-32
3.5.2 UV Laser Metallization.....	3-47
3.5.2.1 Excimer Laser Characteristics.....	3-47
3.5.2.2 Gas Supply Procedure.....	3-49
3.5.2.3 Wafer Processing.....	3-49
3.5.3 UV Laser Passivation.....	3-51

## CONTENTS (continued)

4.0 Solar Cell Experimental Investigations.....	4-1
4.1 Junction Formation.....	4-1
4.1.1 Liquid Dopant and Surface Morphology.....	4-1
4.1.1.1 Textured Surface.....	4-1
4.1.1.2 Chemically Polished Surface.....	4-4
4.1.2 Ion Implanted Emitter and Laser Uniformity....	4-5
4.1.2.1 Conventional Mass Analyzed $31\text{p}^+$ Ion Implant.....	4-5
4.1.2.2 Effects of Damage by 5 keV Ion Implant.....	4-8
4.1.2.3 Effects of "Neutrals" on Mass Analyzed Ion Implantation.....	4-11
4.1.2.4 Non-Mass Analyzed Molecular Ion Implantation.....	4-13
4.1.2.5 $62\text{p}_2^+$ Ion Implantation.....	4-14
4.2 Laser Parameters.....	4-16
4.2.1 Large Laser ("Lucy").....	4-17
4.2.2 Improved Small Laser EXC-1 with Single Lens Focusing.....	4-21
4.2.2.1 p-Type Substrate with $31\text{p}^+$ Ion Implant Dopant.....	4-21
4.2.2.2 n-Type Substrate with $11\text{B}^+$ Ion Implant Dopant.....	4-29
4.2.2.3 Small Laser With Double Focus Lens.....	4-29
4.3 Surface Conditions.....	4-32
4.3.1 Cleaning Procedure.....	4-32
4.3.2 Effects of DI Water.....	4-35
4.4 Finalized Annealing Process.....	4-38

## CONTENTS (continued)

4.4.1 Dopant Source and Methodology.....	4-38
4.4.2 Surface Preparation.....	4-39
4.4.3 Laser Parameters.....	4-39
4.5 Cell Characterization.....	4-40
4.6 Laser Assisted Metallization.....	4-41
4.6.1 Tungsten on Silicon (Batch 1) From WF <sub>6</sub> Gas.....	4-43
4.6.2 Tungsten on Silicon 250-500 Shots (Batch 2).....	4-44
4.6.3 Aluminum on Silicon (Batch 8) from TMAL Gas.....	4-44
4.6.4 Silver Neodecanoate.....	4-47
4.6.5 Direct Writing onto Ti-Pd-Ag Film.....	4-48
4.7 Surface Passivation.....	4-48
5.0 Discussion.....	5-1
5.1 Junction Formation.....	5-1
5.2 Laser Assisted Metallization.....	5-2
5.3 Surface Passivation - LCVD SiO <sub>2</sub> .....	5-2
6.0 Economic Analysis.....	6-1
7.0 Conclusions.....	7-1
References.....	8-1
Acknowledgments.....	9-1

## CONTENTS (continued)

### Tables

3-1.	Excimer laser annealing parameters.....	3-33
3-2.	Fine line metallization by laser photodeposition, laser pulse repetition rate, 2 Hz.....	3-52
3-3.	Fine line metallization by laser photodeposition.....	3-55
3-4.	Fine line metallization by laser sintering and photodecomposition.....	3-56
3-5.	Laser photodeposition of SiO <sub>2</sub> .....	3-58
4-1.	Textured Cz p-type wafer with spin-on source laser annealed.....	4-2
4-2.	Cells fabricated from polished Cz p-type wafer with spin-on source laser annealed.....	4-4
4-3.	Cell performance of thermally diffused caustic polished Cz wafer with spin-on source as dopant.....	4-5
4-4.	Results of laser annealing caustic polished Cz wafer.....	4-7
4-5.	Results of laser annealing on chem-mech polished FZ wafers.....	4-7
4-6.	Average performance of Batch 35 cells.....	4-11
4-7.	Cz p-type material subjected to molecular ion implant.....	4-14
4-8.	FZ material ion implanted with 62P <sub>2</sub> <sup>+</sup> .....	4-16
4-9.	Electrical measurements on B54 and B55.....	4-19
4-10.	First experimental result with the larger laser.....	4-20
4-11.	Results of annealing by the larger laser.....	4-20
4-12.	Electrical performance of large laser processed Cz cells.....	4-21
4-13.	Laser annealing by improved small laser on ion-implanted Cz wafers.....	4-23
4-14.	Sheet resistivity of wafers.....	4-26

## CONTENTS (continued)

4-15. Electrical performance of B24 cells.....	4-27
4-16. Small laser (EXC-1) annealing of Cz and FZ wafers.....	4-28
4-17. ASEC-coated Cz cells.....	4-31
4-18. n-type substrates processed by small laser.....	4-32
4-19. Typical experimental result with laser beam double-focused.....	4-34
4-20. Wafers cleaned without and with 0.2 micron filter.....	4-38
4-21. Electrical performance of the batch-processed cells.....	4-41
4-22. Results of passivation by sputtered oxide.....	4-48
4-23. Electrical measurements of SiO <sub>2</sub> passivated cells.....	4-53
4-24. Deposition parameters and electrical results for cells passivated at higher temperatures.....	4-53
6-1. Baseline thermal diffusion IPEG cost summary.....	6-4
6-2. Excimer laser annealing IPEG cost summary.....	6-4

## CONTENTS (continued)

### Figures

2-1.	Laser annealing process sequences used in the early stages of the program.....	2-1
2-2.	Second phase process sequence.....	2-2
3-1.	Initial laboratory arrangement for excimer laser processing of silicon wafers.....	3-2
3-2.	Laboratory layout for large excimer laser annealing process.....	3-3
3-3.	Excimer laser annealing facility.....	3-5
3-4.	Scan patterns.....	3-8
3-5.	Optical layout for laser annealing of wafers using small excimer laser and beam homogenizer.....	3-9
3-6.	Photograph of laser annealing optical arrangement showing excimer laser at right and 4" square wafer on x-y table at left.....	3-10
3-7.	Optical systems studied by ray tracing. Distances indicated are in millimeters.....	3-11
3-8a.	Spot diagram at kaleidoscope exit plane.....	3-12
3-8b.	Case 1: Single 13 mm lens.....	3-12
3-9a.	Case 2: Results obtained with two biconvex lenses.....	3-13
3-9b.	Case 3: Spot diagram at image plane.....	3-13
3-10.	Scale drawing of optical assembly for metallization....	3-14
3-11.	Isometric view of optical assembly of metallization....	3-15
3-12.	Application of reticon array to intensity profile measurement of single mode HeNe beam.....	3-19
3-13.	Laser pulse shapes used in first phase of laser annealing process studies.....	3-21
3-14.	Excimer laser pulse waveforms.....	3-22
3-15.	Excimer laser pulse waveforms.....	3-23

## CONTENTS (continued)

3-16. Excimer laser pulse waveforms with modified driver and preionizer circuits.....	3-25
3-17. Laser pulse waveforms during annealing of ion-implanted wafers.....	3-26
3-18. Intensity vs time from large x-ray preionized excimer laser using XeCl at 308 nm.....	3-27
3-19. Optical setup for kaleidoscope testing.....	3-27
3-20. Beam profiles.....	3-28
3-21. Beam profiles.....	3-29
3-22. Laser energy vs shot number for 1000 shots at 20 Hz repetition rate.....	3-30
3-23. Monitor of laser pulse energy during laser annealing of 4" diameter wafer.....	3-31
3-24. Laser pulse waveforms measured after Batch 9, and after laser repair following Batch 5.....	3-48
3-25. WF <sub>6</sub> absorption cross section.....	3-50
4-1. 500x SEM photos of textured wafers.....	4-3
4-2. Light and dark I-V curves of a thermally diffused n+ cell.....	4-6
4-3. Laser annealing on 5 keV, $2 \times 10^{15}$ atoms/cm <sup>2</sup> ion implanted surfaces.....	4-9
4-4. Process sequence for Batch 35.....	4-10
4-5. Depth profiles of Batch 35 cells.....	4-12
4-6. Spreading resistance depth profiles.....	4-17
4-7. Typical microscopic defects on wafer surface.....	4-19
4-8. Laser scan showing incomplete surface annealing.....	4-24
4-9. Surface damage revealed by etching.....	4-25
4-10. I-V curves of best cell from B26-2.5E.....	4-30
4-11. Spectral response of best cell from B26-2.5E.....	4-31

## CONTENTS (continued)

4-12. Depth profiles of B27N and B29N.....	4-33
4-13. Defects formed after 1.3 J/cm <sup>2</sup> annealing.....	4-34
4-14. Comparison of surface preparation techniques.....	4-35
4-15. Wafers cleaned in-house and then laser annealed.....	4-36
4-16. Wafer cleaned by vendor after ion implant.....	4-37
4-17. Surface cleaning process.....	4-39
4-18. Final processing sequence.....	4-40
4-19. I-V and quantum efficiency.....	4-42
4-20. Overall photograph of tungsten lines.....	4-43
4-21. Surface profile on tungsten lines.....	4-44
4-22. Auger analysis and profile of CVD W on Si.....	4-45
4-23. Laser CVD Al on Si.....	4-46
4-24. Grid pattern for silver neodecanoate metallization.....	4-47
4-25. Remains of pattern after dissolving film.....	4-47
4-26. AES analysis indicating SiO <sub>2</sub> compound has less than 5% nitrogen.....	4-50
4-27. AES profile suggesting oxide thickness about 150Å.....	4-50
4-28. I-V curves before and after passivation.....	4-51
5-1. Best efficiency of laser annealed Cz cell and comparison with space cell.....	5-3
6-1. Proposed excimer laser process.....	6-2
6-2. Comparison of junction formation processes.....	6-3



## SECTION 1.0 INTRODUCTION AND SUMMARY

The objective of the overall program described in this report was to develop a solar cell process sequence that incorporates three process steps which use pulsed excimer lasers, to verify that this sequence yields high efficiency cells at a low cost, and to document the feasibility of carrying this technology from the laboratory bench scale to factory scale. The three process steps are: junction formation, surface passivation, and front metallization. Since the processes chosen for investigation have been described previously in the literature, the program was intended to be an application study instead of a research study.<sup>1</sup> It was found, however, that many different parameters had to be investigated. As a result, the exploratory experimental matrix covered here was far more extensive than originally planned.

For the junction formation process step, dopant application by both ion-implant and spin-on techniques was studied, using wafers that were either texture etched or chemical-mechanically polished. The pulsed excimer laser was used to drive in the dopant, anneal damage out of the silicon, and activate the dopant in the junction. For the surface passivation process step, a thin oxide layer was deposited on the silicon surface using excimer laser-assisted chemical vapor deposition. For the metallization process step, narrow metallic lines were deposited on the silicon surface using excimer laser-assisted chemical vapor deposition and photodecomposition of metallic gases.

Two experimental facilities were assembled, one for junction formation and one for laser chemical vapor deposition (CVD). The junction formation process used an XeCl laser at 308 nm, a beam homogenizer, and a computer controlled x-y motorized table assembly that moved the wafer. The laser CVD processes used an ArF laser at 193 nm, an optical mirror and line focus assembly that traveled on an x-y motorized table, and a stationary wafer process chamber and gas handling system. Gases studied were WF<sub>6</sub> and Al(CH<sub>3</sub>)<sub>3</sub> for metallization, and SiH<sub>4</sub> plus N<sub>2</sub>O for passivation. A liquid spin-on material, silver neodecanoate, also was investigated in the laser metallization process study. All of the equipment operated satisfactorily.

The principal question studied in the laser junction annealing experiments was how to produce a uniform, shallow junction that was fully activated and had no residual deep crystal damage or surface damage and was not contaminated by impurities. This high quality junction required a uniform laser beam, optimum laser pulse duration (25 to 30 nsec), 50% beam overlap in both the x and y directions to overcome effects of laser beam edge nonuniformities, and an energy density of 1.5 J/cm<sup>2</sup>, with little overlap margin on either side. Also, the wafers had to be handled very carefully to keep them extremely clean and free of

dust before and during laser processing.

It was concluded from these investigations that excimer laser junction annealing can be applied to large area wafers and yield high efficiency solar cells (15.5% to 16.0% on 2 cm by 2 cm cells). However, much care is required in processing to prevent the molten wafer surface from being contaminated or distorted, making this process step too costly for a factory process.

The principal question studied in the laser CVD metallization experiments was how to deposit the desired material so that it was bonded to the substrate, did not affect the underlying junction, and was deposited rapidly enough to be economical in a factory process. Gridlines of both W and Al that were about 1000Å thick were successfully deposited, and some of these passed the tape adherence test. However, analysis of the deposits using Auger spectroscopy revealed that both the W and Al deposits consisted of metal oxides. In addition, the process time of 1000Å per minute per gridline was definitely not adaptable for production.

Similar to laser-assisted metallization, the objective of the surface passivation study was to deposit silicon oxide film onto silicon solar cells in order to improve the  $V_{oc}$  by deactivating the surface states. Main concerns included the deposition rate, purity of the film, adhesion, and effect on passivation. Satisfactory results were obtained in all areas except that the data were insufficient to prove effectiveness in passivation, a topic that is likely to respond to future investigation.

## SECTION 2.0 SELECTION OF PROCESS SEQUENCE

Three parallel processes were used in the early stage of the program: one with ion implantation as the dopant source, the other with spin-on liquid dopant (Fig. 2-1). P-type substrates grown in-house were predominantly used because of their availability, their well-characterized properties, and because they represented typical production quality substrate material. Both n-type and p-type Czochralski substrates were used based on 3-in. and 4-in. round slices as well as 4-in. squares. Float zone material was also used occasionally as a control sample material.

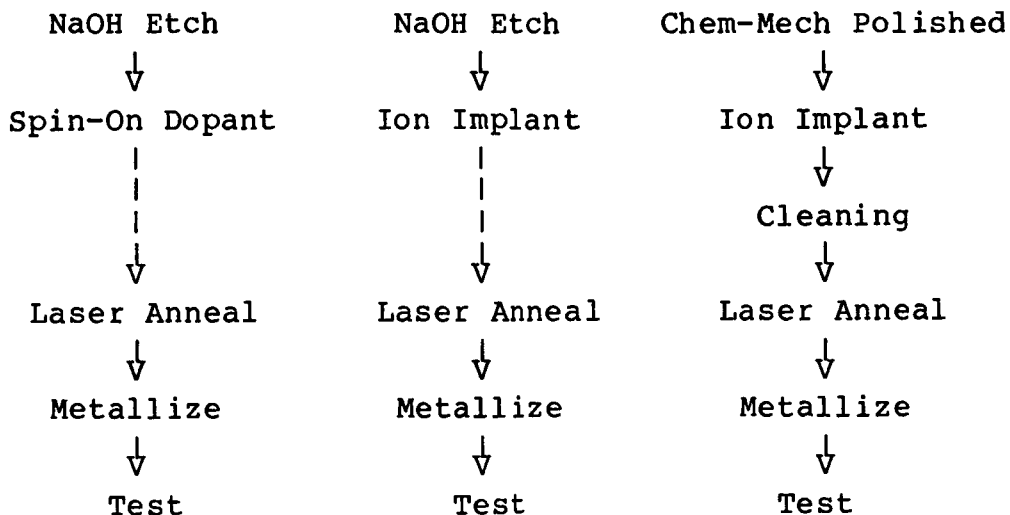
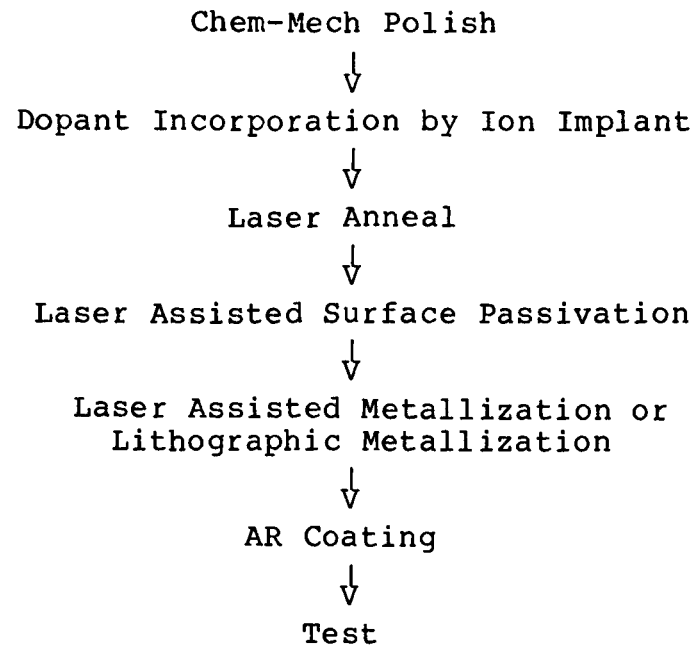


Fig. 2-1. Laser annealing process sequences used in the early stages of the program.

After a series of experiments using liquid dopant sources without promising results, the process was discontinued. Instead, ion implantation was substituted for n<sup>+</sup> deposition on mechanically polished wafers as baseline experiments.

Optimized laser annealing parameters were derived by an iterative method. Variables include laser energy density, pulse duration time, beam uniformity overlap percentage, and substrate temperature. Wafer cleaning and cell fabrication followed conventional methods, such as organic solution rinses, acid rinsing, and evaporated contacts.

In the later stages of the program, laser-assisted pattern writing for front grid lines and surface oxide growth for passivation were investigated. The second phase of the laser annealing process is shown in Fig. 2-2.



**Fig. 2-2.** Second phase process sequence.

## SECTION 3.0 LASER PROCESS EXPERIMENTAL DETAILS

### 3.1 EXCIMER LASERS

Two laser facilities were utilized for the excimer laser process studies. One facility was based on a small-scale commercially-available laser, the EXC-1 produced by Spectra-Physics, that provided about 20 mJ per pulse at 308 nm or at 193 nm at repetition rates up to 100 Hz. The second facility, used only for laser annealing studies, was based on a large scale x-ray preionized discharge laser that provided 1.5 J per pulse, but was limited to a low-repetition rate of about 30 pulses per hour. Both laser facilities were equipped with x-y translation tables for wafer motion and with diagnostics to determine laser pulse energy and waveform. The pulse duration of the small laser was varied from 6 nsec to 40 nsec, whereas that of the large laser was about 90 nsec. The beam size of the small laser was 1 cmx1 cm square, which was reduced optically to about 1 mmx1 mm for laser annealed junction formation, and to 1 cmx0.1 mm for laser CVD metallization. The beam size of the large laser was 3 cmx3 cm and was reduced optically to about 1 cmx1 cm for laser annealing.

### 3.2 LABORATORY LAYOUT

The initial layout of the laboratory area for the small laser is shown in Fig. 3-1. Two processing stations are shown, the excimer laser annealing facility, and the laser photodeposition facility that was used for surface passivation and fine grid metallization studies. A five foot square exhaust hood was installed as well as a separate exhaust port to vent exhaust gases from the scrubber, from the excimer laser, and from the laser annealing process station. The scrubber, the low pressure process chamber, the gas cabinet, and the control console were built during the course of the project.

The initial laboratory layout for the small excimer laser shown in Fig. 3-1 was modified several times throughout the program to accommodate placement of optical components between the excimer laser and the wafer location. The optical arrangements are described in Section 3.3.

A high energy x-ray preionized excimer laser, located in another laboratory, also was used for experiments on laser annealed junction formation. The laser was designed for experimental research on various excimer lasers, and was adapted to the laser annealing experiments reported here with minimal changes. The laboratory set-up for the large laser is shown schematically in Fig. 3-2.

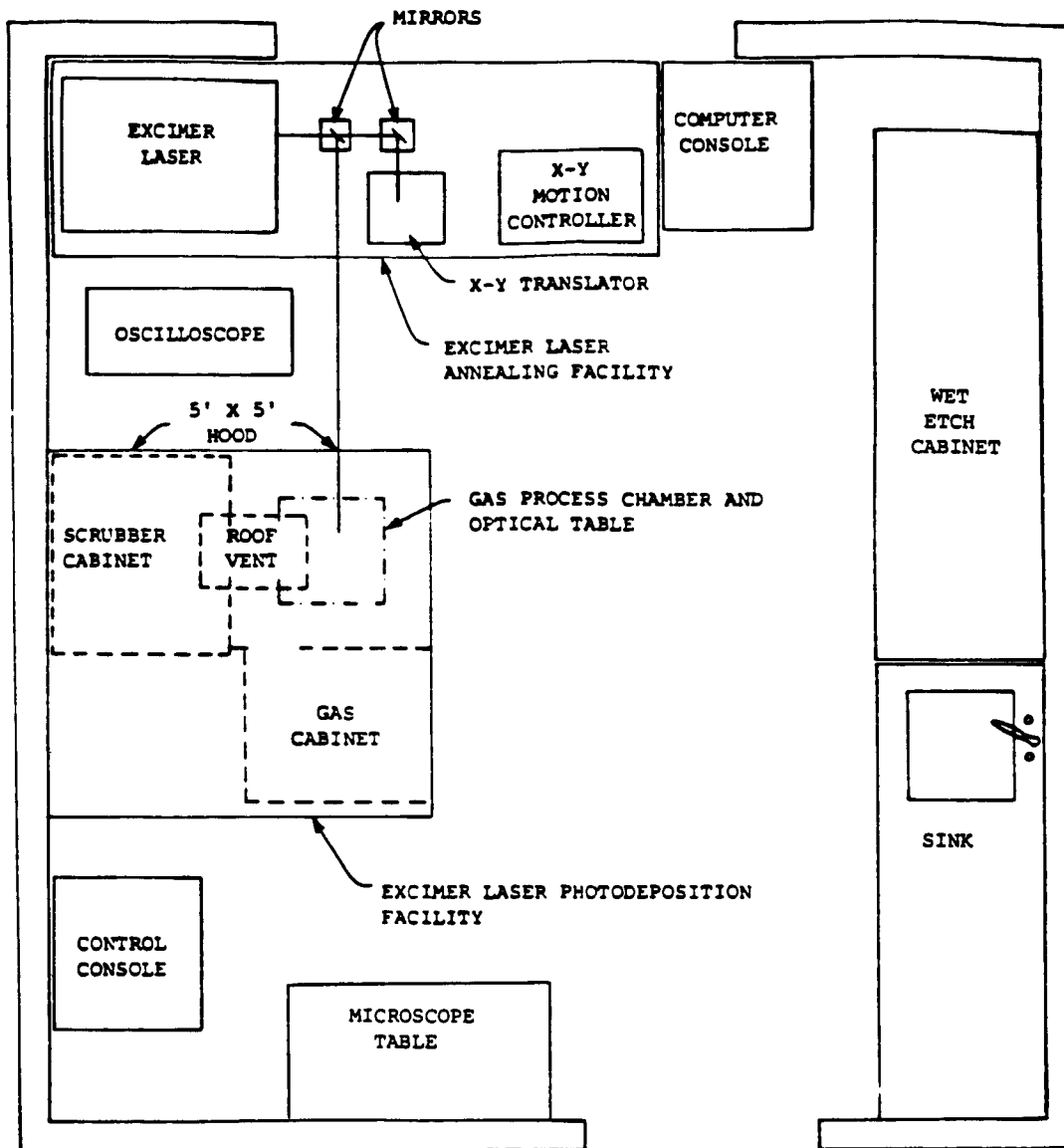


Fig. 3-1. Initial laboratory arrangement for excimer laser processing of silicon wafers.

The laser and energy storage supplies occupied the central area of the room. The control panels and screen room for diagnostics were located well away from the regions of high voltage, high gas pressure, and high laser intensity. Regular monitoring of the x-ray generation by the device was done in order to maintain a safe working environment for personnel. The output of the laser was transported to the x-y translation table by a dielectric coated UV reflective mirror that permitted passage and return of a He-Ne alignment laser.

The excimer laser discharge chamber was made of Lucite with a Teflon liner, supporting two aluminum electrodes. One of the

electrodes was milled very thin (~1.5 mm) to transmit x-rays with very little loss. The electrodes were pulse charged to just below the self-break voltage, and the x-ray preionizer acted as the switch, ionizing the laser gas and causing voltage breakdown. A dielectric pulse forming line then provided current to the discharge at its self-sustaining voltage for about 75 nsec. The discharge volume was 75 cm long by 4 cm between electrodes by 3.5 cm wide. The laser chamber included 4" diameter AR coated windows at each end. An external 20 m radius of curvature total reflector and a 30% reflective flat output coupler formed the optical cavity. To provide sharp beam edges, a rectangular aperture was located adjacent to the output coupler.

A focusing lens was positioned to form an image of the laser aperture at the wafer, and to provide a size reduction of about 3 to 1. The lens could be adjusted axially to vary the spot size, thereby providing variation in energy density on the wafer.

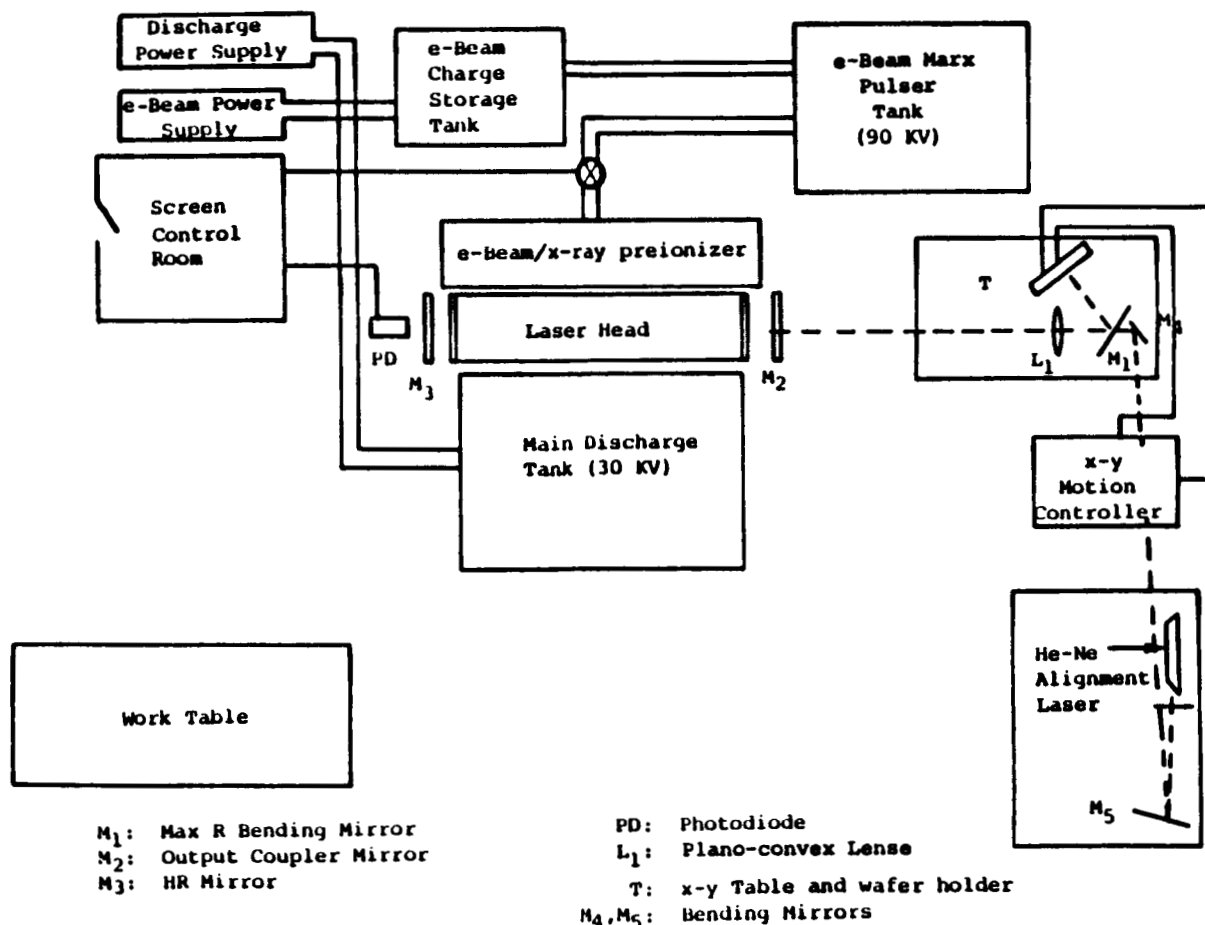


Fig. 3-2. Laboratory layout for large excimer laser annealing process.

Since the large laser was originally fabricated for single pulse experiments the construction materials limited the gas lifetime. The laser output remained constant (within 10%) for about 30 pulses, before requiring replacement of a portion of the gas to bring the energy per pulse back to its original value. A period of 1 to 2 minutes was required to recharge the electrical power supplies between laser pulses.

The large laser processing station used a two-axis, DC motor driven table that held the wafer vertically. The table position was sensed by an integrated shaft encoder, and direction, speed (feedrate), and position were determined by a programmable controller. The motion controller was not interfaced to an external computer as in the case of the small excimer laser processing station, and both table positioning and firing of the large laser were performed manually. To avoid the possibility of electronic damage to the controller during the high voltage electrical discharge of the large laser, the controller was turned off during laser firing. The battery backed-up internal memory of the controller permitted the operator to return the table to the last position processed and then to advance to the next area to be annealed.

### **3.3 OPTICAL SYSTEMS FOR SMALL SCALE LASER**

#### **3.3.1 Initial Laser Annealing Setup**

The following description of the first optical system used for laser annealing of silicon wafers by the small scale EXC-1 laser refers to Fig. 3-3. The laser source, optical train components, x-y motorized stage, and ancillary components were located on a 3' by 8' table with a magnetic top surface. The optical component holders were secured to the table with magnetic bases.

The laser source was an EXC-1 excimer laser which provided 6 to 40 nsec (FWHM) duration output pulses at repetition rates up to 100 Hz. The output wavelength used for laser annealing was 308 nm and the average laser output energy per pulse was about 20 mJ. The output beam had a square cross section of 1x1 cm. The light output was essentially incoherent and thus interference effects at the work surface were absent. The beam divergence was approximately 10 mrad full angle.

The excimer laser output beam was steered to the proper height with the beam elevator consisting of mirrors M1 and M2 shown in Fig. 3-3. The mirrors were coated with a dielectric multilayer stack selected for high reflectivity and independence of reflectivity with polarization at the design wavelength and angle of incidence (45°). Thus the originally unpolarized light remained unpolarized. A square aperture (not shown) was placed between the laser and the subsequent optical elements to create an image at the work surface with sharp edges. Aperture insertion loss was 20% to 50% depending on aperture size. The light was directed to an overhead support stand (not shown) which





3-5

chance of foreign material being deposited on the surface during annealing.

Two stepper motor controlled stages and a stepper motor sequencer and power supply were used and were automated using an LSI-11 based computer as master controller along with appropriately designed electronics for control of laser triggering and table motion. The control program used the parallel interface for I/O control of the sequence and laser firing. The control program was written in Macro-11 assembly language to optimize timing and execution speed.

The control program executed several distinct scan patterns designed for round and square wafer geometries, as shown in Fig. 3-4. The first pattern is a standard raster scan with user selectable pulse overlap in both directions. Both table speed and wafer size were selectable. Based upon the input values of effective spot size and table speed, the computer controlled and fired the laser at the correct frequency and allowed for table acceleration time. The total number of scan lines required to cover a given annealed area was also computed and used to control the scan. User input to the program was over the serial interface to the terminal as shown in Fig. 3-3. A given scan also could be aborted from the keyboard if desired. The annealed area resulting from the first scan pattern is square or rectangular. For circular wafers, to anneal as large an area as possible with minimum process time, a diagonal type annealing pattern (shown in Fig. 3-4) was employed. Control of all experimental parameters was available through the terminal. The control signals sent by the computer to the sequencer are shown in Fig. 3-3. A single power supply was used for both motors by multiplexing the sequencer output using relays in the control box. The scan patterns did not require that both motors be operated concurrently, so this scheme was quite satisfactory.

### 3.3.2 Small Scale Excimer Laser with Optical Beam Homogenizer

Initial laser annealing tests using the small laser indicated that the spatial intensity distribution was quite nonuniform. Beam profile measurements, described later, confirmed that the intensity was high in the center, decreasing toward the edges. To improve the spatial uniformity of the laser spot on the wafer, the optical system was modified to incorporate a fused silica beam homogenizer, also known as a kaleidoscope. Three small rectangular (~1.7x1.7x100 mm) kaleidoscopes were purchased. One was mounted in a five-axis (three-translation plus two angles) holder; the other two kaleidoscopes were set aside as spares.

The holder was designed to support the kaleidoscope on thin wires near each end of the kaleidoscope. This resulted in the correct index of refraction conditions for total internal reflection along the entire length of the kaleidoscope and hence optimal light throughput. A section of rectangular channel tubing surrounded the kaleidoscope and served to protect three of its

long optical surfaces. Propagation of the beam through the kaleidoscope could be observed by fluorescence seen through the one exposed surface and the exposed ends.

The optical arrangement that incorporated the beam homogenizer is shown in Fig. 3-5. Alignment was performed using the same HeNe laser beam that was used to align the excimer laser cavity, thus ensuring colinearity. The light throughput using this setup was measured and found to be 78% with the input beam focused very close to the front surface of the light pipe. This throughput was measured for a single input lens and kaleidoscope, or a total of four optical surfaces. The theoretical value based on Fresnel losses is 81.5%, indicating a close approximation of the maximum expected value. For reasons to be discussed, such optimal focusing could not be implemented during high repetition rate laser operation because of observed damage to the kaleidoscope. Thus the actual throughput used for wafer processing was 65% for both lenses and kaleidoscope (the best value expected would be 73%). A photograph of this optical arrangement is shown in Fig. 3-6, and is the setup used for laser annealing of wafers to produce twenty-five 4 square cm cells at more than 15.5% efficiency.

Major damage to the kaleidoscope was observed when the beam was focused too near the front surface of the kaleidoscope or the laser pulse repetition rate was too high. One kaleidoscope was fractured, and a second one exhibited small cracks and bubbles at the input end indicating light absorption leading to thermal fracture and melting of the glass. Three strategies were implemented to overcome these difficulties: lowering the repetition rate of the laser to reduce thermal loading; moving the focus of the input lens further from the front surface of the kaleidoscope (with about 10% loss of intensity throughput); and taking care to keep the input end of the kaleidoscope clean. The third kaleidoscope operated satisfactorily for three months, and the two damaged kaleidoscopes were repaired.

The necessity of lowering the laser repetition rate to assure survival of the kaleidoscope required that the table speed be reduced appropriately. Previously the control program required user determination and entry of table speed. Since the table speed was controlled by a very non-linear potentiometer, accurate determination of this parameter was time consuming. Consequently, this operation was placed under computer control. The computer used the given row length and software timed length between indexing and completion pulses to determine the table speed to an accuracy of about 0.1%. This value was then used to determine laser repetition rate.

The propagation of the excimer beam through the kaleidoscope and complete lens system was studied using a ray-trace code. The purpose of this study was to determine the expected beam uniformity and its dependence on lens design and demagnification. This code was specifically written to allow entire planes of rays

to be propagated through the optical system in three dimensions. An additional feature of this code included the ability to output spot diagrams of the beam at user selected planes in the optical system. These diagrams proved very useful in evaluating optical distortion, spot size, and distribution of rays in the plane.

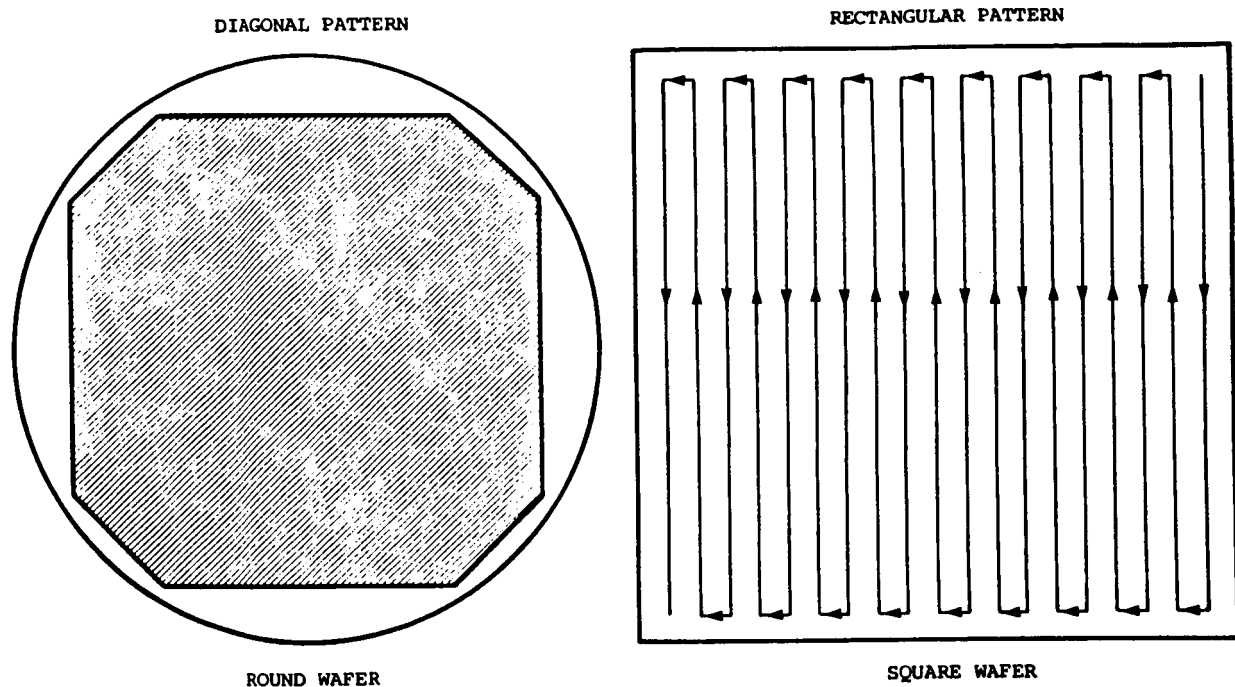


Fig. 3-4. Scan patterns.

Three cases of interest were modeled using the code. The position of the optical components in each of these cases is shown in Fig. 3-7. For the energy densities required, a demagnification of the kaleidoscope output of about 2:1 was needed. Experimentally, it was known that the imaging for such a low  $f$  number case was somewhat unsatisfactory. The spot diagrams showing the beam at the kaleidoscope output, at the plane of best geometric image for Case 1, are shown in Fig. 3-8. The axial position of best focus was determined by examination of several planes spaced 0.5 mm apart near the paraxial focus.

Not surprisingly, it was found that better homogenization results when the input beam had a significant inherent angular divergence. Since the small excimer laser has about 5 mrad half angle of divergence, the kaleidoscope technique is suited to homogenize the beam, as had been shown experimentally. The drawback of the large angular divergence of the beam is the lack of focusability which requires that the kaleidoscope front face be placed quite close to the focus of the input lens. The ray

trace code showed that significant numbers of rays are lost from the corners of the beam if the face is positioned more than 8 mm from the focal plane.

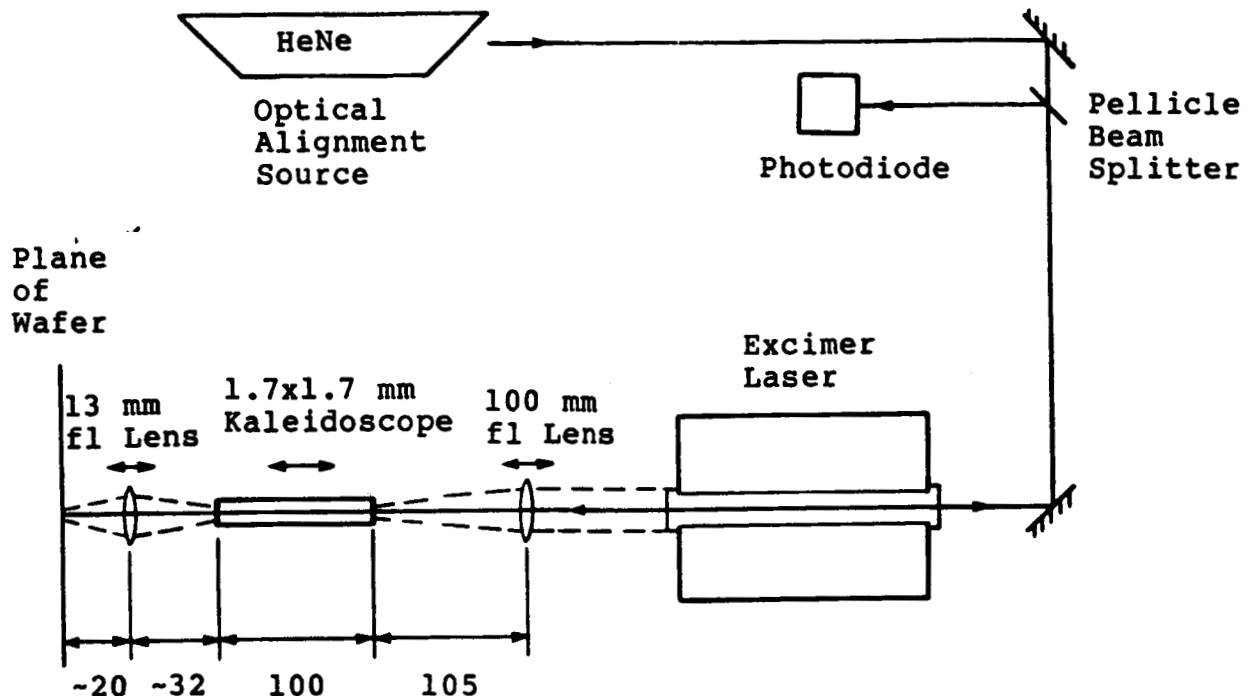


Fig. 3-5. Optical layout for laser annealing of wafers using the small excimer laser and beam homogenizer.

Figure 3-8(b) shows the spot diagram at the image plane for the case of a single 13 mm focal length lens. A significant number of rays fail to be collected within the main dark square measuring 0.8x0.8 mm (2:1 size reduction). By analogy with the usual geometric minimum blur circle, one might call this a smallest blur square. Some pinhole distortion at the spot boundary is also noted. The failure to collect the marginal rays adequately would be expected to be improved significantly by substituting the single lens with an equivalent two lens (Petzval type) combination. The best spacing between the two lenses was tested using the ray trace code. For each case several planes near the predicted paraxial image plane were plotted. The object to image distance for each case was based on the desired 2:1 size reduction. The two extreme cases of the lens spacing of 0 and 40 mm were tested first. The former case showed only fair performance for this system and was not studied further.

Figure 3-9(a) shows the results obtained at a position of 14 mm from the final surface for Case 2 (see Fig. 3-7). One observes that in contrast to the single lens case all rays except a few in the corners are reimaged within the desired spot area. The lens

positions for Case 2 were chosen to give a lens combination whose equivalent focal length was 13 mm and whose secondary principal plane was approximately 3 mm from the front surface of the second lens. An additional advantage of the lens combination is the fact that the wafer surface may be displaced +0.5 mm without a significant degradation of image quality. This is an improvement on the single lens case.

Figure 3-9(b) shows the image plane results for Case 3 (Fig. 3-7), the image not as sharp as in Case 2 and with less positioning tolerance. However, the blur square size is improved over that of a single lens. More of the total energy of the beam will hit the correct area on the wafer positioned at this location.

ORIGINAL PAGE IS  
OF POOR QUALITY



Fig. 3-6. Photograph of laser annealing optical arrangement showing excimer laser at right and 4" square wafer on x-y table at left.

### 3.3.3 Optical Arrangement for Metallization and Passivation Process Steps

This section describes the optical system used to carry out studies of laser photochemical vapor deposition for the passivation and metallization process steps. The optical assembly used for laser vapor CVD processing is shown in Figs. 3-10 and 3-11. The laboratory layout was similar to that shown in Fig. 3-1, with the excimer laser shifted to the opposite end of the optical table. The 193 nm laser beam was reflected off a 45° turning mirror and directed to the metallization processing optical assembly (Fig. 3-10). The beam enters Fig. 3-10 perpendicular to the page and parallel to the axis of motion of the upper motorized translation stage (Fig. 3-11 shows a 3-dimensional view of the motorized table motion). The beam then was deflected 90°, making it parallel to the axis of motion of the lower translation stage. The beam was then reflected downward through a cylindrical focusing lens and through the UV window of the metallization process chamber. The wafer was located in a fixed position inside the chamber, and the optics were adjusted to provide best focus of the laser beam at the plane of the wafer and proper orientation of the line focus relative to the direction of motion of the motorized translation stages.

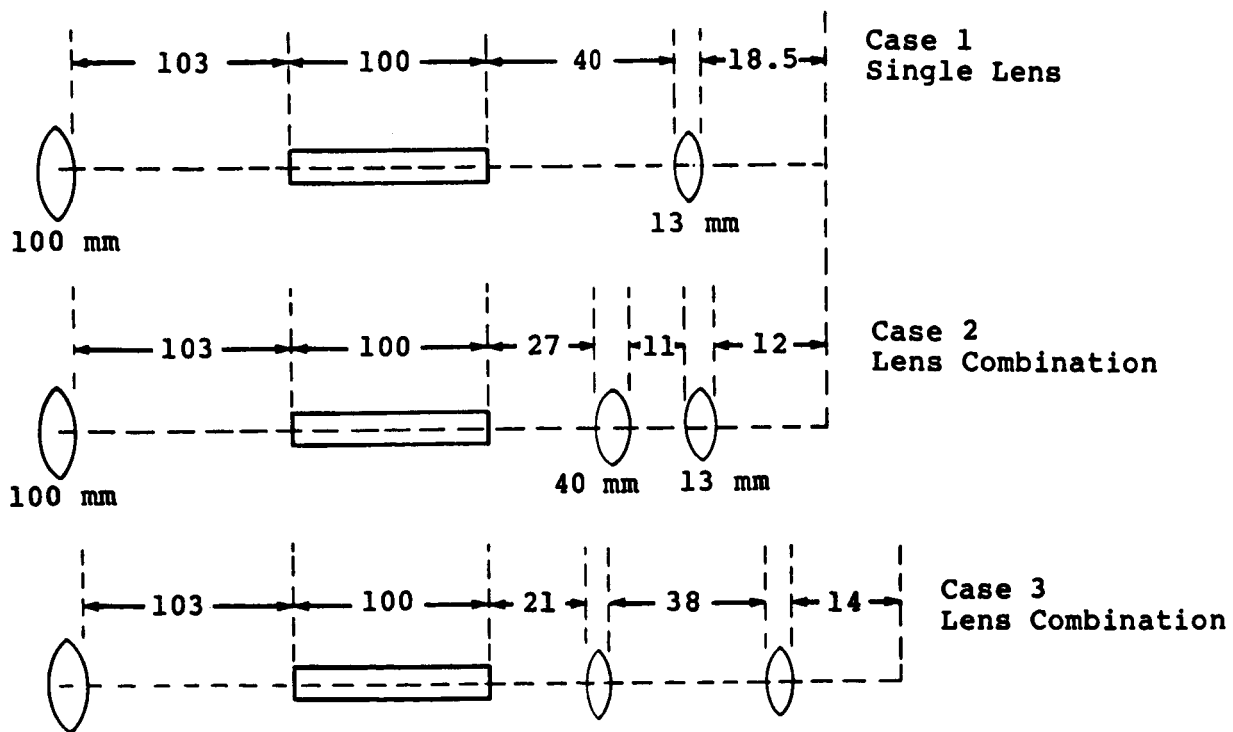


Fig. 3-7. Optical systems studied by ray tracing. Distances indicated are in millimeters.

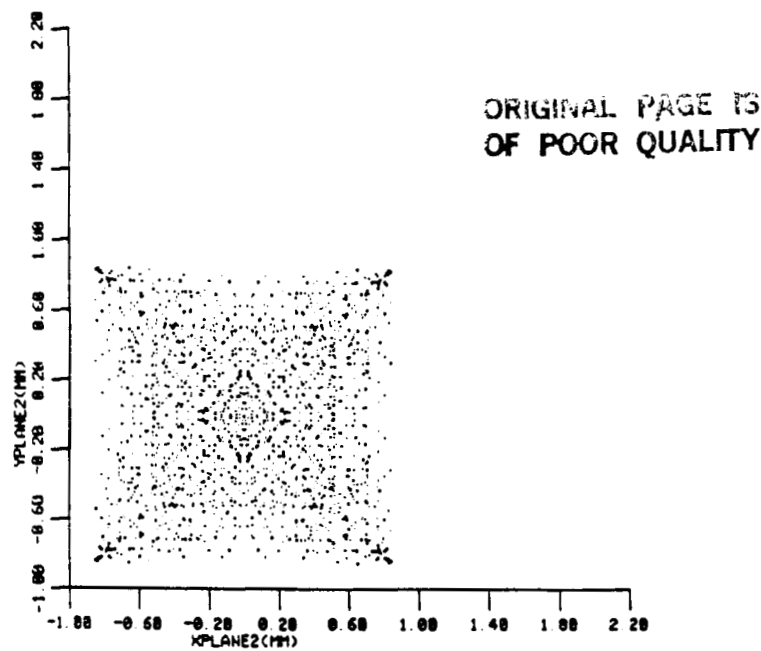


Fig. 3-8a. Spot diagram at kaleidoscope exit plane for a beam with 4 mrad angular divergence.

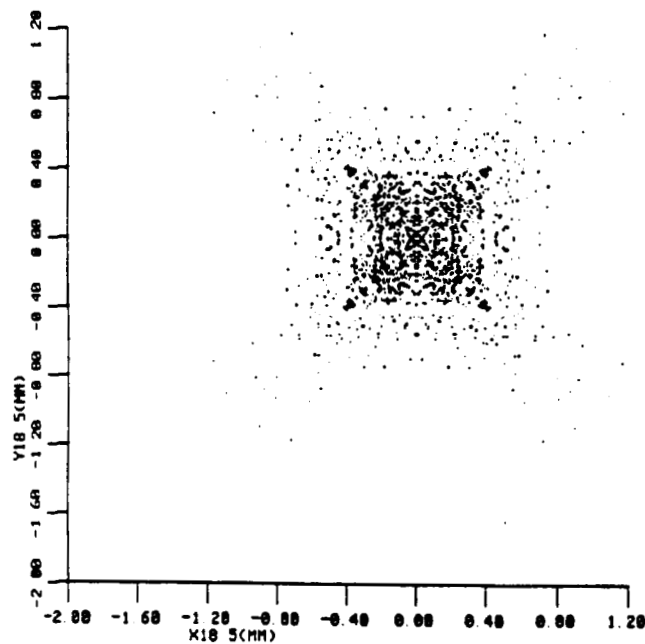


Fig. 3-8b. Case 1: Single 13 mm lens; 2:1 reduction in size.



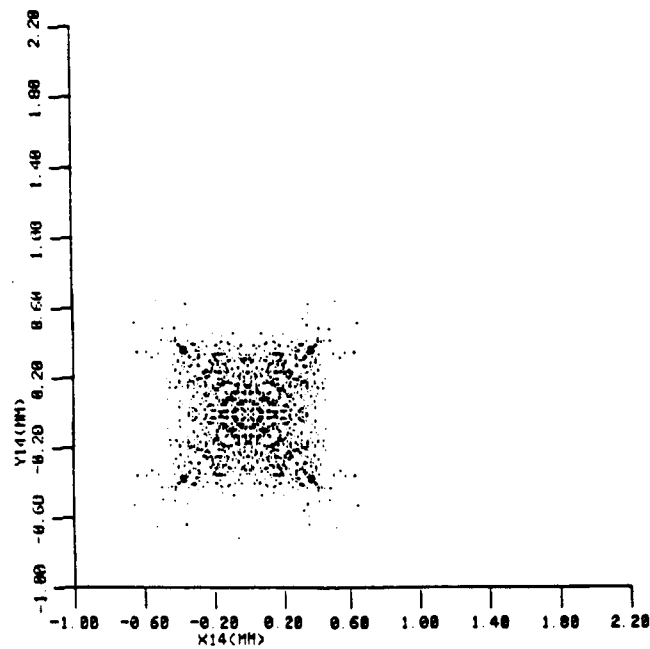


Fig. 3-9a. Case 2: Results obtained with two biconvex lenses with a combination effective focal length of 13 mm.

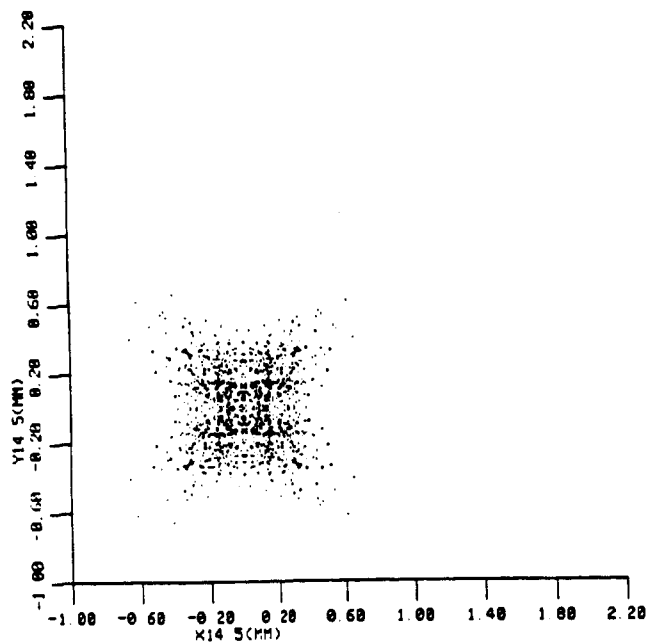
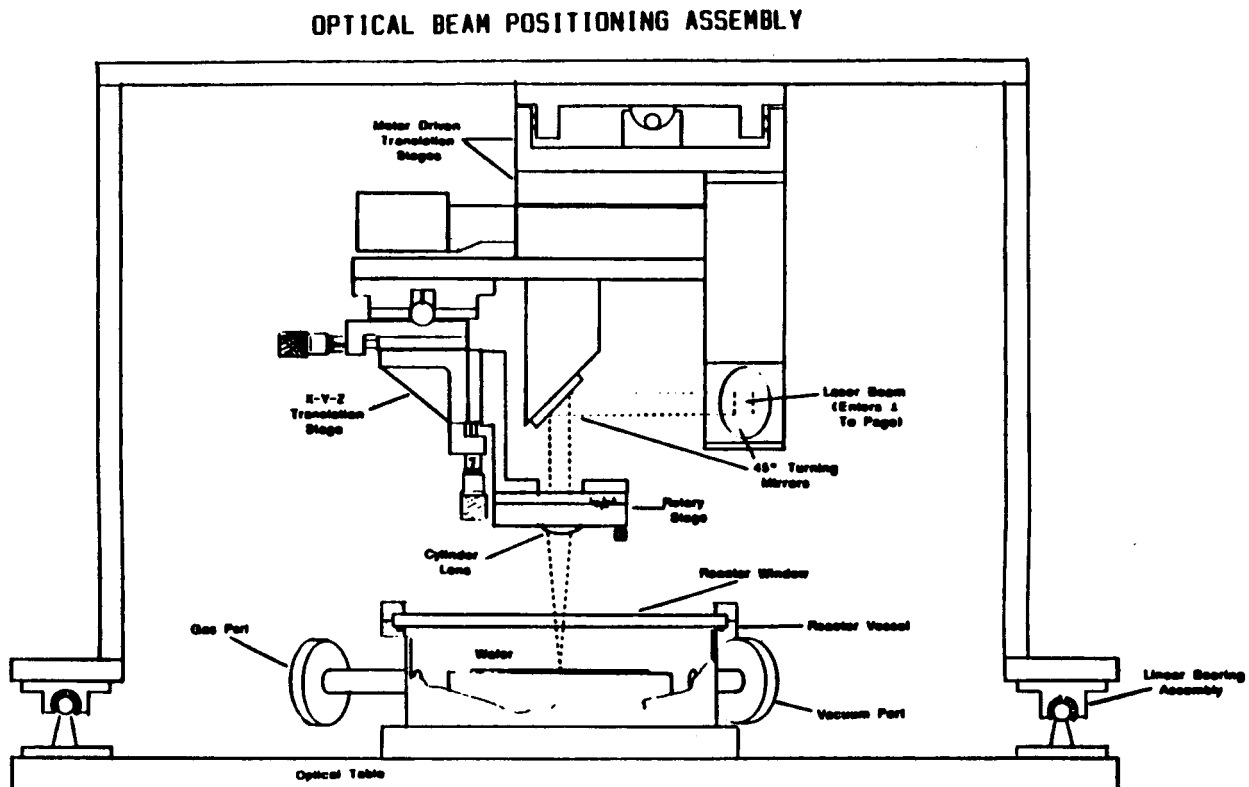


Fig. 3-9b. Case 3: Spot diagram at image plane.

The 45° turning mirrors were 2-inch diameter, large enough to accommodate the full laser beam. The cylinder lens was mounted on an x-y-z translation stage to center the lens with the center of the laser beam, and to adjust the focal plane relative to the wafer. The lens was mounted in a rotary stage to align the line focus with the direction of travel of one or the other of the motorized translation stages. In this way long metallization lines could be made up of line segments laid down end to end on the wafer. Line segments 1 to 2 cm long and 50 to 100 microns wide could be made using this optical arrangement.



**Fig. 3-10.** Scale drawing of optical assembly for metallization process step.

The whole optical assembly was mounted on rigid rails and could be rolled aside to permit access to the gas chamber in order to change wafers. With the optics moved to one side, the top flange holding the UV window could be unbolted and removed, permitting the previous wafer to be removed and a new wafer installed.

An objective cylinder lens was employed to form a line focus for the metallization process step and was analyzed using three-dimensional, extended source, ray trace code. Two commercially available lenses were studied. The first was a plano-cylinder lens with a nominal paraxial focal length of 100 mm. This lens was found to produce a minimum blur square 90

microns in size at a working distance of 83.5 mm. The second lens was a best form lens also with a nominal focal length of 100 mm. This lens produced a blur square size of 40 microns at a working distance of 72 mm. Both lenses were studied assuming an input beam from an extended source of 1.2x1.2 cm with 0.1 mrad half angle beam divergence. These parameters are those expected of the EXC-1 using unstable resonator optics. Thus it appeared that the inherent laser and lens performance would meet the metallization line width requirements, when used at this f number of six. The superior performance of the best form lens indicated that this lens would be the best choice.

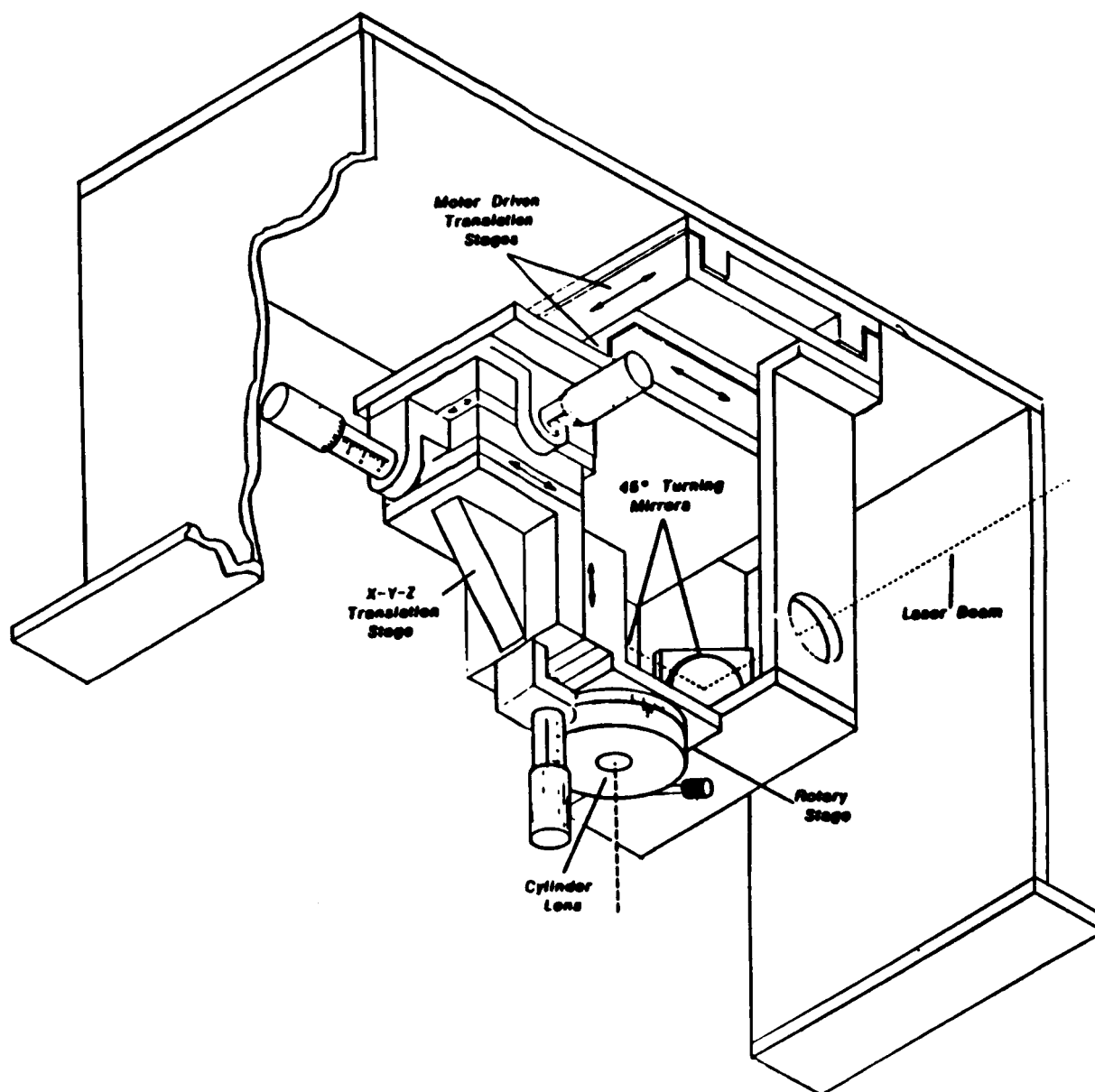


Fig. 3-11. Isometric view of optical assembly of metallization process step showing motion of translation stages.

The specification of unstable resonator optics for the EXC-1 at 193 nm was calculated, and a suitable vendor for the optics and coatings was located. The cavity optics consisted of a 200 cm radius of curvature plano-convex high reflector and a 75 cm meniscus output coupler with a dot high reflection coating 3.75 mm in diameter. The latter was AR coated for 193 nm on the second surface, and the two optics were designed to be separated by 62.5 cm, providing for a cavity magnification of ~2.7. Both substrates were made of suprasil quartz. However, the unstable resonator optics were not installed because stable resonator optics produced satisfactory line widths.

Many of the optics holders and motorized translation stages used for laser CVD were already available from the buildup of the laser annealing optical assembly. The common components for the two processes were not duplicated because of cost. The changeover from the metallization process to the laser annealing process required a period of 2 to 3 days for rearrangement and realignment of the optical assemblies, and to change the laser from 193 nm ArF operation to 308 nm XeCl operation.

### **3.4 LASER DIAGNOSTICS**

The output beams of the excimer lasers and optical beam handling systems used for wafer processing were measured to determine energy per pulse, pulse duration and waveform, and spatial distribution of intensity at the wafer location. In some experiments, the energy of each laser pulse was monitored during wafer processing and recorded on floppy disk memory to allow computer analysis of statistical variations when a large area wafer was processed by a large number of small spots distributed over the surface. The diagnostic equipment and techniques used for these measurements are described below.

#### **3.4.1 Laser Pulse Energy Measurements**

Average power measurements of the small laser (EXC-1) output at 308 nm and 193 nm were made as a function of repetition rate using a Scientech calorimeter type power meter. At the same time, the laser pulse repetition rate was measured using a Systron Donner pulse generator and Triplet frequency meter, and the energy per pulse was then determined. The 1" diameter Scientech sensor was placed at the laser output location and also at the wafer location, thereby measuring directly the optical loss introduced by the intervening beam handling optics. The laser pulse energy at 308 nm was found to be independent of repetition rate from low repetition rate (~1 Hz) up to more than 50 Hz, the highest value used in the laser annealing process step.

In order to monitor the pulse energy from the small laser during processing, a photodetector was set up to intercept the low intensity laser signal transmitted through the high reflectivity mirror of the excimer laser optical cavity. This detector signal

was fed into a high sensitivity FET op-amp integrator, which provided a measurement of the total energy in each pulse of the laser. The op-amp drift was measured and found to be less than 0.15 mV/sec. Since the signal from the photodiode was greater than 100 mV, sensitivity was excellent. The time constant of the integrator was set to distinguish individual pulses at repetition rates up to 100 Hz. The Scientech power meter had a time constant of ~14 sec and thus could not be used to detect individual pulse energy values at moderate rep rates. The integrator output was digitized by a 12-bit A/D converter and fed to the computer for processing and memory storage. Tests showed that light level changes of 1 part in 4000 were readily distinguished using this diagnostic once the dark current offset of the integrator was nulled. The digitized information was readily transferred directly to the PDP-11 computer for analysis and storage on magnetic media. Software was written to collect the data while performing the laser annealing process.

A Scientech volume absorption calorimeter having a 4 inch entrance aperture was used to determine the energy of individual laser pulses from the large excimer laser. The calorimeter was placed at the laser output and also at the wafer location. During laser annealing process experiments the laser pulse energy was checked periodically to verify reproducibility from pulse to pulse and to assess the need for replacement of the laser gas.

#### **3.4.2 Pulse Duration and Temporal Waveforms**

Temporal pulse waveform measurements at 308 nm were made by inserting a fast PIN photodiode into the output beam and recording on a 1 GHz bandwidth oscilloscope. The reproducibility of the output of the small laser was determined by recording a number of waveforms on a single Polaroid film. The response time of the detector and oscilloscope was less than 1 nsec, which readily resolved the pulses, ranging from 6 to 40 nsec for the small laser and about 90 nsec for the large laser. At 193 nm a Hamamatsu vacuum photodiode was used together with a 400 MHz bandwidth oscilloscope.

#### **3.4.3 Spatial Intensity Distribution Measurements**

Three methods were used to obtain data on the spatial distribution of laser intensity at the wafer surface location. One method utilized the photodiode described above which was illuminated by the portion of the laser spot transmitted through a tiny pinhole. The pinhole was scanned over the spot area and variations in pulse waveform were recorded. The second method was to take an imprint pattern of the laser spot on a wafer or on photosensitive paper. Various attenuating filters were inserted in the beam and the resulting changes in the imprint patterns with filter attenuation were used to infer spatial intensity variations.

A reliable, quantitative method of measuring beam profiles was developed, using a reticon array with associated frame digitizing features. In the configuration selected, the reticon diagnostic digitized and stored light intensity data at the rate of ~400 kHz. The array was designed to characterize short time duration, (compared to the frame time) pulses, typical of excimer lasers used for laser annealing. These arrays are particularly useful for studying light intensity distribution in the UV regime, since they possess a quartz window and adequate wavelength response down to 0.2 microns. This is in contrast to their major competitor, CCD arrays, which typically respond only to wavelengths greater than 0.4 microns.

The array consisted of 32 x 32 individual pixels spaced on 100 micron centers. Each individual photodiode current was stored on an integrated capacitor and read out (through an integrated shift register) every 4 msec, thus zeroing the array. By initiating the triggering of the excimer laser on the end-of-frame signal provided by the reticon array, a single shot of video information was collected, representing the laser pulse. Since the PDP-11 computer could not digitize and store information at the high speeds required to minimize array dark count, a special timing and digitizing board was designed around an AMD6108 8 bit A/D (1 MHz maximum rate) and fast (150 nsec) video memory. The available amount of video memory was sufficient to store 8 successive frames of spatial intensity information. The individual photodiodes had a dynamic range (manufacturer's data) of nearly 2000:1; thus the sensitivity of the array was limited by the 1 bit quantization error (measured) of the A/D converter to about 0.5 to 1 percent.

During the testing phase of the array, dark count data were collected and stored in a data file. These data were then averaged and used to subtract the dark count from the actual laser beam intensity profile. The pixel-to-pixel variation in response was tested by uniformly illuminating the array with a diffuse light source. The resulting variation was less than 5%. These data were also stored to provide appropriate response scaling. This information was then transferred to the PDP-11 computer and saved in a diskette data file. The information was then transferred to a VAX 11/780 computer where a Gaussian curve fit routine could be used to extract pertinent information on the spatial size and ellipticity of the pulse. Also, a contour plotting routine was employed to give direct visual information concerning the two dimensional energy distribution. Such information is shown in Fig. 3-12 which is the output of a small HeNe laser. The output was Gaussian as expected, and the profile was found to be slightly elliptical.

### **3.5 EXPERIMENTAL MEASUREMENTS**

In this section, the diagnostic measurements made to characterize the beams produced by the excimer lasers with their associated optical arrangements are described and the wafer processing

procedures, operating parameters, and observations are presented. The laser annealing experiments are described first, followed by metallization experiments and finally surface passivation experiments.

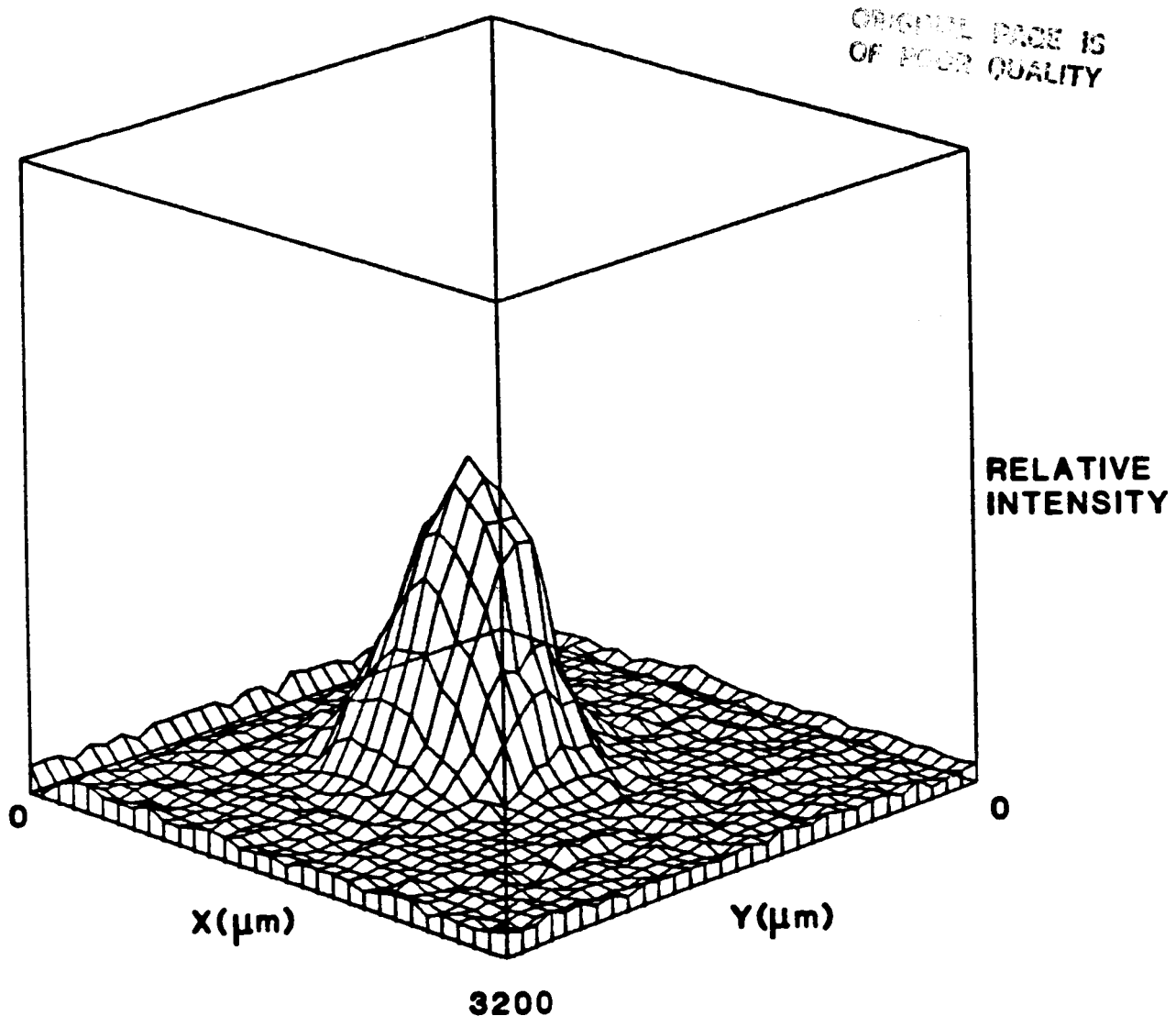


Fig. 3-12. Application of reticon array to intensity profile measurement of a single mode HeNe beam.

### 3.5.1 Junction Formation by Excimer Laser Annealing

Excimer laser annealing of single crystal silicon wafers was conducted in three phases. The first phase was an exploratory period using the small EXC-1 excimer laser to investigate a number of process variables, including textured wafers, spin-on techniques for introducing dopant into the junction, and various

laser parameters such as energy density and pulse duration. Some parameters already were selected based on prior work. For example, a laser wavelength of 308 nm was selected because in previous laser annealing studies it had yielded high solar cell efficiency<sup>1e</sup> and because XeCl excimer lasers that provided 308 nm output exhibit the longest gas lifetime and are more convenient to operate than other excimer lasers.

The second phase was a study of the application of a large scale excimer laser to junction formation. Results showed improvement over previous results on the small scale laser due to improved beam uniformity. However, work with the large scale laser was dropped because the output pulse duration was long (90 nsec) producing junctions that were too deep, the laser beam was not as uniform as required, and the pulse repetition rate was too slow (2 minutes between pulses).

The third phase used the small scale laser again, but modified by adding an optical beam homogenizer to provide good uniformity in laser intensity over a square spot on the wafer. This approach yielded the best solar cell efficiencies, good reproducibility in the laser annealing process step, and allowed optimization of most of the process variables.

The characteristics of the laser beam for each of these phases are discussed next, followed by a tabulation of the parameters used for each of the laser annealing experiments and the final processing of fifty 2-inch quadrants.

#### **3.5.1.1 Laser Pulse Duration and Waveform**

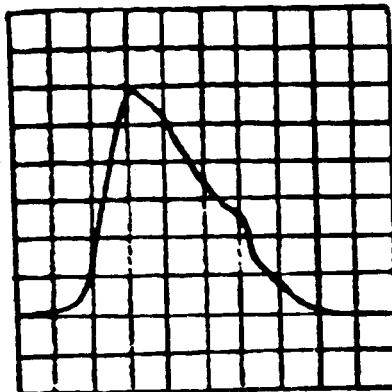
The pulse duration of the small laser was varied from 6 nsec to 40 nsec, and the pulse duration of the large laser was 90 nsec. This wide range of pulse duration permitted an investigation of the effect of pulse duration on various laser annealing and junction formation processes.

The pulse duration of the small laser was varied by selection of the gas mixture and by modifying the electrical pulse forming network (PFN) used to drive the discharge in the laser gas. Typical pulse waveforms used in the first phase of the laser annealing experiments are shown in Fig. 3-13. The use of helium diluent produced a single pulse of short duration (~6 nsec FWHM). Changing the gas mixture to a neon diluent produced a double pulse with the two peaks separated by about 25 nsec. The two peaks in laser output are correlated with two peaks in discharge current through the laser gas.

The relative amplitude of the two peaks could be varied by changing the amounts of Xe and HCl in the laser gas mixtures. This effect is illustrated in Fig. 3-14, which shows pulse waveforms from the small scale excimer laser during the third phase of laser annealing experiments. The waveforms shown are for 10 overlapping pulses in each case, indicating good

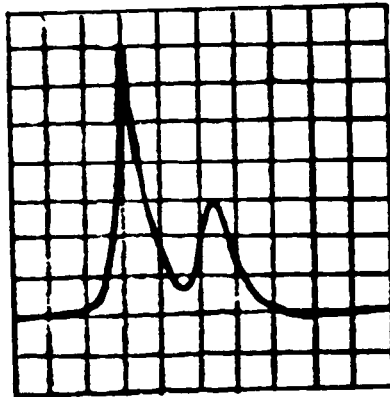


reproducibility of each of the waveforms for the two processing runs. In both cases, the full width half maximum pulse duration is 30 nsec. However, the second peak is larger in Fig. 3-14(a), whereas the first peak is larger in Fig. 3-14(b). This difference in pulse waveform produced a significant difference in threshold laser energy density on the wafer that induced surface damage. It was found that surface damage during laser annealing resulted in reduced solar cell efficiency; optimum processing required the laser energy density to be near, but below, the damage threshold. Here we note that the laser pulse waveform is one of the variables that influences the surface damage in laser energy density.



2 nsec/Div

a. Short pulse using helium diluent

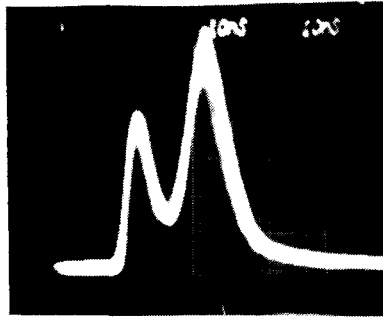


10 nsec/Div

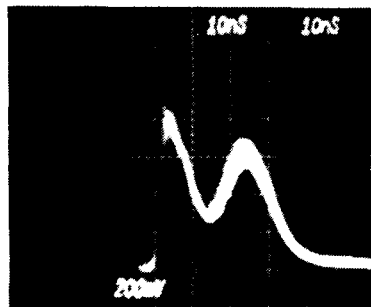
b. Long pulse using neon diluent

Fig. 3-13. Laser pulse shapes used in first phase of laser annealing process studies.

ORIGINAL PAGE IS  
OF POOR QUALITY



a. Batch 23: low damage threshold,  $1.2 \text{ J/cm}^2$



b. Batch 24: higher damage threshold,  $1.5 \text{ J/cm}^2$

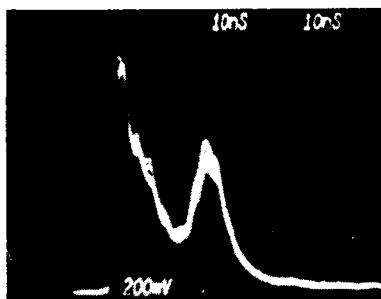
**Fig. 3-14.** Excimer laser pulse waveforms.

One of the better wafer processing results was obtained using the laser waveform shown in Fig. 3-15(a). It is seen that the second peak is considerably lower than the first peak. In order to study the effect of removing the double pulse, the PFN of the EXC-1 laser was modified to produce the waveform shown in Fig. 3-15(b). A further change in the PFN produced the longer pulse waveform (40 nsec) of Fig. 3-16(a). These changes did not lead to improvements in results, although other variables such as the wafer cleaning procedure also were changed during this period of testing. However, it was determined by spreading resistance measurements that the junction produced by the 40 nsec pulse of Fig. 3-16(a) was too deep. Based on these results, the PFN was again changed to produce the pulse waveform shown in Fig. 3-16(b) which was used for subsequent laser annealing experiments.

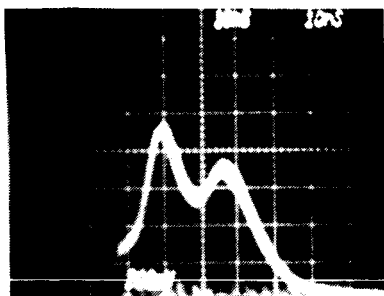
The junction formation by laser annealing task was completed by processing fifty 5 cm square wafers over a period of three

working days. The pulse waveforms obtained at intervals during this period are shown in Fig. 3-17. The waveforms varied somewhat from one batch to the next, and from the beginning to the end of a batch; however, the pulse duration (FWHM) remained 30 nsec to within a few nanoseconds.

The pulse waveform produced by the large scale excimer laser is shown in Fig. 3-18. The 90 nsec duration resulted in a higher surface damage threshold limit (about  $2.0 \text{ J/cm}^2$ ), deeper heat penetration, and a junction dopant profile that was deeper than desired.



a. Laser pulse waveform used in processing Batch #26



b. Laser pulse waveform after modifying EXC-1 pulse forming line

Fig. 3-15. Excimer laser pulse waveform.

### 3.5.1.2 Spatial Distribution of Intensity

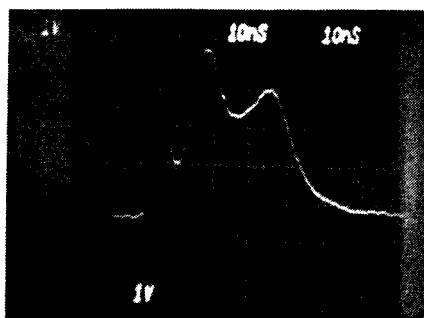
In the course of the laser annealing study, it was found that the laser intensity spatial profile must be very uniform. During the first phase experiments, the small scale laser was applied directly to the wafer, with focusing optics to image a plane near the output aperture of the laser onto the wafer. The spot size at the wafer needed to achieve 1 to  $1.5 \text{ J/cm}^2$  laser energy

density was about 1 mm square, requiring a low f number focusing lens. It was found that both the laser beam itself and the lens introduced nonuniformity in the spatial distribution of intensity at the wafer. Quantitative profile measurements of the laser beam were made using the reticon array, but it was not used directly at the wafer spot. Photosensitive paper imprints and wafer imprints were used which showed that the intensity was quite high in the middle and fell off significantly toward the edges. Also, the edges were not straight line images of the rectangular aperture used at the laser, due to geometrical aberration of the image by the low f number lens.

To improve the uniformity of intensity over the spot area at the wafer when using the small laser, the optical beam homogenizer described in Section 3.3 was used. It was important to select the correct size homogenizer, to assure good optical quality in manufacture, and to limit the angular spread of the output beam so that the reimaging optics would not introduce lens distortion. An experimental study of two beam homogenizers obtained by two different suppliers was carried out using a He-Ne laser beam and the reticon array.

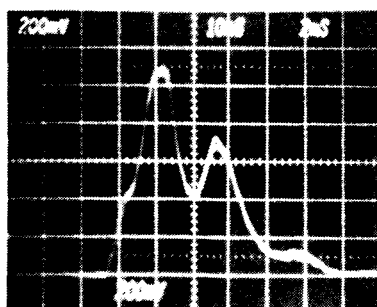
The optical setup used for testing is shown in Fig. 3-19. To closely approximate the behavior of the excimer laser, the small HeNe ( $\omega_0 = 0.45$  mm) beam was expanded by a telescope and then focused into the beam homogenizer (a 3 mm x 3 mm x 100 mm kaleidoscope). The f/4 input optics resulted in the fairly uniform beam shown in Fig. 3-20(a). This profile was taken at the output of the kaleidoscope and measured 3x3mm. To test the ability to reduce this object size to an image size compatible with the desired energy density at the work surface, an f/1 optic was used at a 2:1 conjugate ratio with the resulting image shown in Fig. 3-20(b). The image was square and possessed a rapid drop-off in intensity at the edges. The uniformity of the beam could be improved if the input and output faces of the kaleidoscope were better polished. An imperfection in at least one of the faces was observed to lead to spurious light scattering. The conclusion from this experiment was that f/4 input optics are sufficient to homogenize the beam to the  $\pm 7\%$  level. Figure 3-20(b) indicated that beam overlapping of 100-200 microns at the work surface should be sufficient.

In another series of experiments, a 5x5 mm kaleidoscope was used with the identical optical train. The resulting output was too large to record in a single shot on the reticon, but by scanning the array across the optical field the output (using f/4 output input optics) was found to be as uniform as that shown in Fig. 3-20 for the 3x3 mm kaleidoscope. The difficulty with the 5x5 mm kaleidoscope stems from the large size reduction ratio required to achieve energy densities of  $\sim 1.2$  J/cm<sup>2</sup> at the work surface. Thus, although the 5x5 mm kaleidoscope was of superior optical quality, it was not suitable for the laser annealing desired in this work.



ORIGINAL PAGE IS  
OF POOR QUALITY

a. PFN arranged for 40 nsec pulse duration (Batch 35)



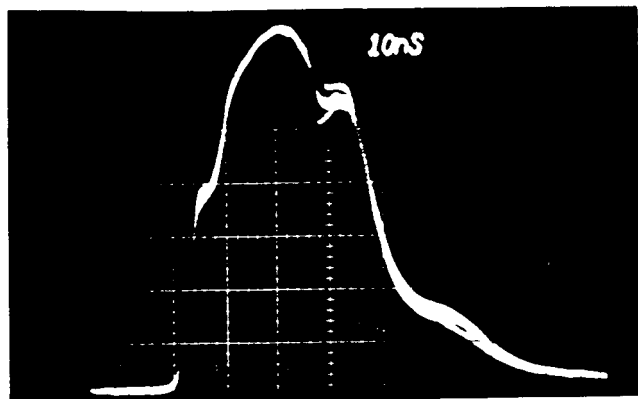
b. PFN arranged for 25 nsec pulse duration (Batch 37)

Fig. 3-16. Excimer laser pulse waveforms with modified driver and preionizer circuits.

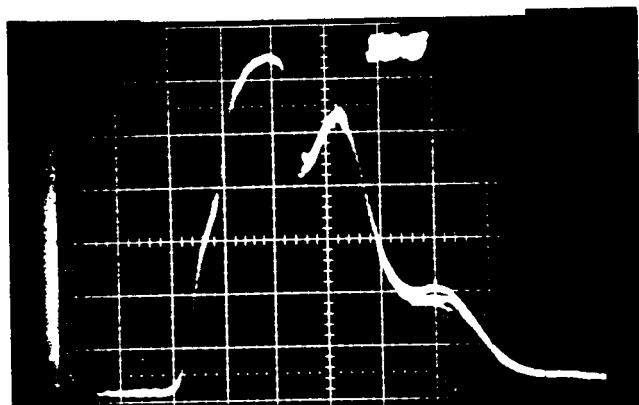
Three 1.7x1.7x100 mm kaleidoscopes of better optical quality were subsequently obtained and used with f/1 optics to reduce the image size to about 1 mm square. The smaller kaleidoscopes had beveled edges to prevent chipping during the polishing process, and had a high polish on all six surfaces. Beam profiles at the wafer using one of these kaleidoscopes are shown in Fig. 3-21. Figure 3-21 is a reticon profile exhibiting the sharp edge drop-off (<100 microns) found (experimentally) near the best focus. Also of interest in this figure is the well-defined plateau region, which contained nearly all of the pulse energy. The ray trace computational studies indicated that movement of the wafer plane more than 0.5 mm in either direction resulted in loss of this edge sharpness.

The optical ray tracing analysis described previously in Section 3 showed that a sharper focused image of the kaleidoscope output aperture could be obtained at the wafer by using two lenses rather than one. Furthermore, previous experiments had shown that better solar cell results were obtained if the laser spot was sharply focused on the wafer than if it was defocused. For these reasons, the single lens focusing arrangement was modified

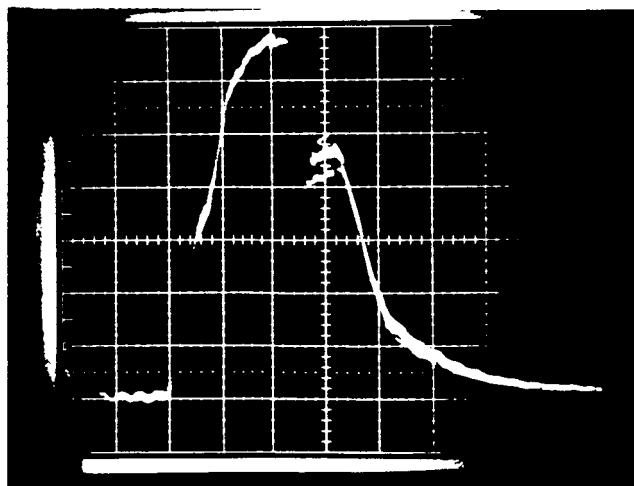
by adding a second lens. The spacing between the lenses, distance from the beam homogenizer, and distance to the wafer each could be varied individually by micrometer driven slides. The added lens had a focal length of 40 mm and diameter of 25 mm.



a. After Batch #59



b. Before Batch #60



c. After Batch #62

Fig. 3-17. Laser pulse waveforms during annealing of ion-implanted wafers.

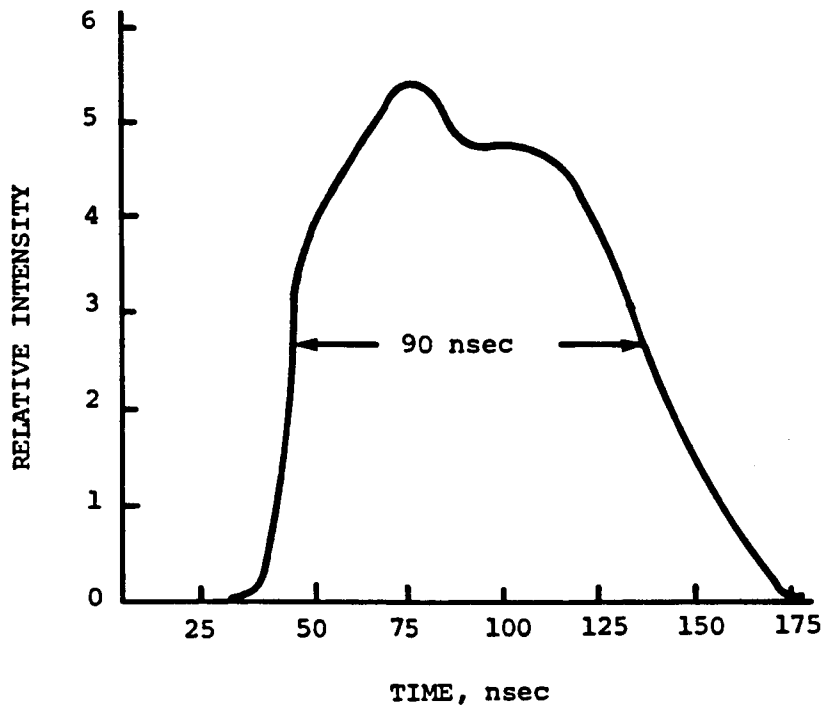
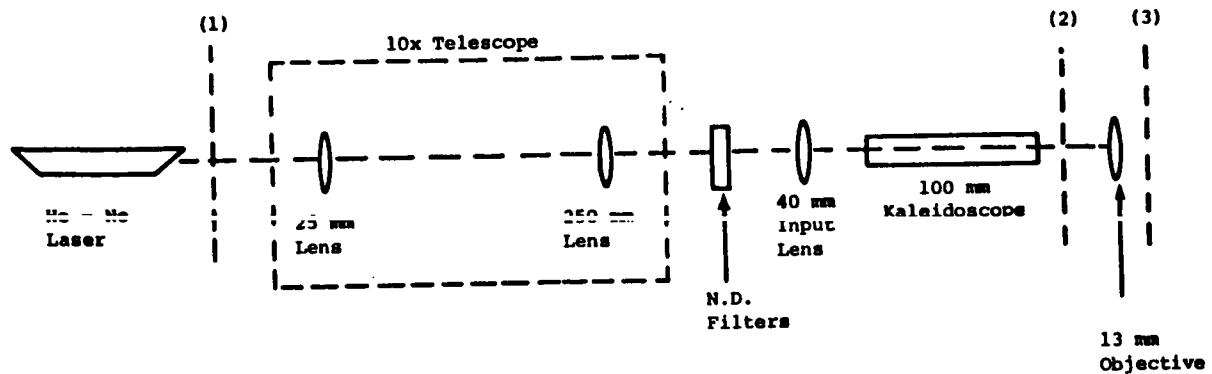


Fig. 3-18. Intensity vs time from large x-ray preionized excimer laser using XeCl at 308 nm.



Notes:  
 (1), (2), (3): Reticon Imaging Locations

Fig. 3-19. Optical setup for kaleidoscope testing.

The resulting laser spot using two lenses was found to be considerably more uniform, based on measuring the spot size dimension on photosensitive paper as a function of beam attenuation using neutral density filters. The intensity fall

off at the edge occurred over a dimension of 0.05 mm for a spot size of 1.0 mm. This spot edge definition was better than the 0.10 mm resolution element size of the reticon array. However, wafer processing using this sharper focus produced tiny damage sites on the wafer at laser energy densities that previously had produced only slight damage at the edges of the spot. Also multiple damage lines were seen at the edges. These effects are thought to be due to larger local intensity gradients in small regions of intensity nonuniformity at the output of the kaleidoscope. The multiple edge lines are due to nonregistry of multiply reflected beams within the kaleidoscope, and tiny damage sites distributed over the spot area are due to imperfect polishing of the kaleidoscope surfaces.

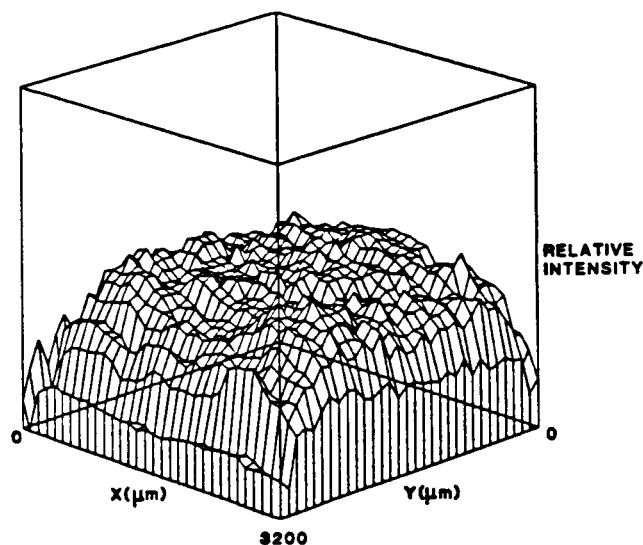


Fig. 3-20a. Beam profile at exit plane of kaleidoscope using  $f/4$  input optics.

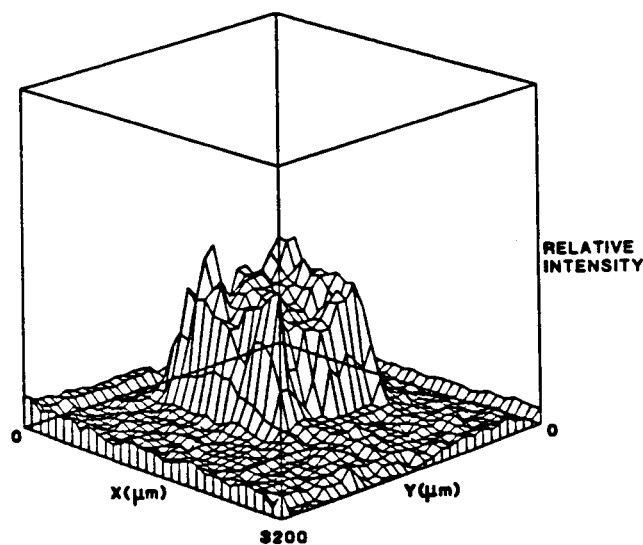


Fig. 3-20b. Beam profile demagnified 2x and reimaged.



After observing these damage effects, the optical imaging assembly was returned to the single lens configuration used previously.

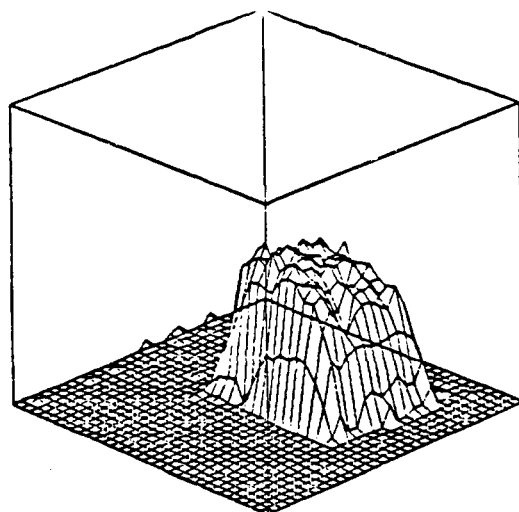


Fig. 3-21a. Excimer laser beam profile after kaleidoscope homogenization.

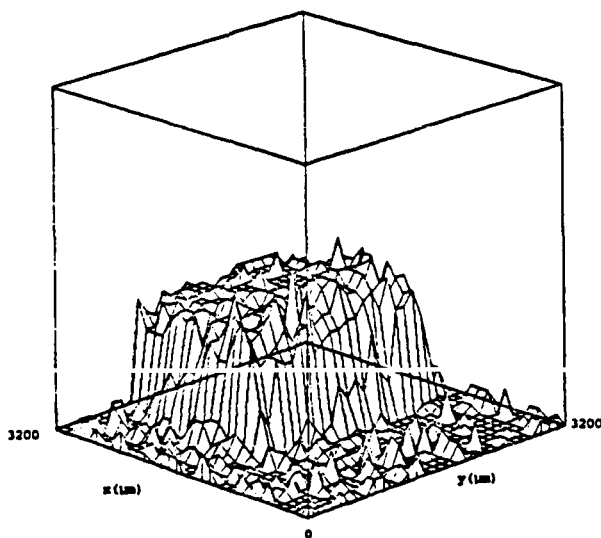


Fig. 3-21b. Beam profile showing edge falloff of excimer laser spot at wafer near best focus with single lens imaging.

An effort was made to measure the intensity distribution of the large laser using the reticon array. Unfortunately, due to the presence of the high voltage switches and the e-beam discharge, the electrical noise prevented successful operation of the unshielded array and computer. Due to the high speed signals present on the reticon array board, cable lengths were limited

and thus both array and motherboard had to be located less than 3 feet away from the actual location chosen for beam profiling. In order to duplicate as closely as possible the conditions during actual laser annealing operations, we could not optically relay the image of the output aperture to the existing screen room. Thus the screen room could not be used to house electronics. To eliminate the electrical noise, construction of a portable Faraday enclosure for both the reticon array and computer was initiated. Initial tests were still subject to excessive noise. However, after obtaining good junction formation results in the early Phase 3 experiments with the small laser, further work on the large laser was stopped.

### 3.5.1.3 Laser Repeatability

The digital photodiode described previously was used to monitor the individual per pulse energy as a function of repetition rate. Figure 3-22 shows one of the results obtained using this probe. An energy increase of ~5% was sometimes seen as the laser warmed up, reaching a plateau after about 1000 pulses. The same behavior was observed at 10 Hz rep rate. The short term energy fluctuation appeared smaller at 20 Hz than at 10 Hz (not shown). When necessary in wafer processing, the laser was operated at 20 Hz for one to two minutes to reach steady output before directing the beam on the wafer.

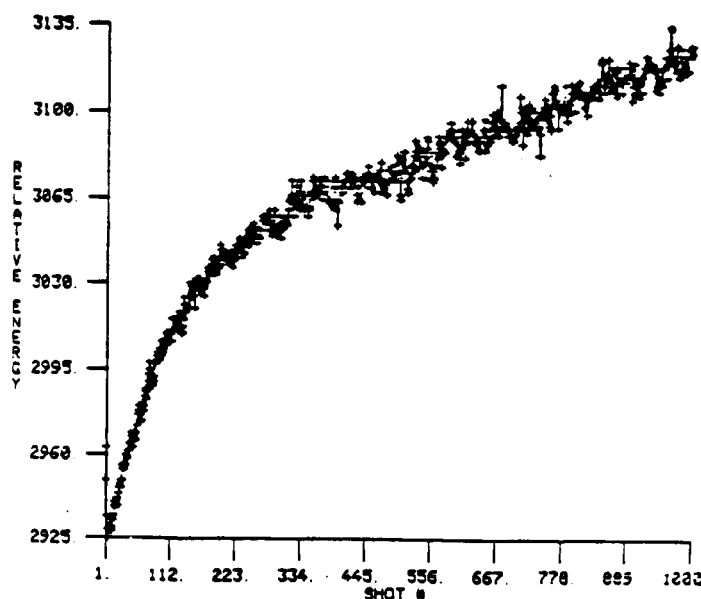


Fig. 3-22. Laser energy vs shot number for 1000 shots at 20 Hz repetition rate.

The raster scanning software was modified to allow real-time monitoring of the laser output energy during processing of a

wafer. Figure 3-23 shows results obtained with the photodiode probe synchronized with laser processing of a wafer. The detector was placed to view the weak 308 nm output transmitted through the high reflectivity cavity mirror of the excimer laser. It was found that the signal was slightly modulated by the motion of the wafer table due to feedback from laser reflection off the wafer and the glass wafer holder induced by each laser output pulse. The reflection and fluorescence retrace the optical train to the laser and are transmitted through the UV coated laser cavity mirrors to the detector.

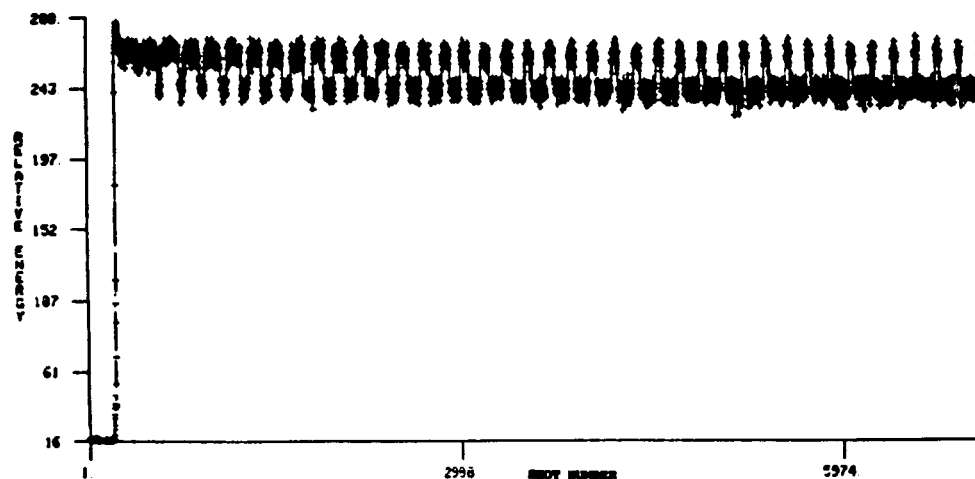


Fig. 3-23. Monitor of laser pulse energy during laser annealing of 4" diameter wafer. Regular modulation of the detector signal is due to reflections, not to laser energy variations.

For the results shown in Fig. 3-23, the motorized table was programmed for a 4.2 inch long scan pattern in steps of 0.020", beginning just off a 4 inch diameter round wafer. Each row of spots was spaced 0.021". Each cross in the figure represents a laser pulse. The low initial signal level was due to background noise from the room lights, before the laser was activated. During the early portion of the record, the laser spot was near the edge of the wafer and the detector signal corresponds to the laser spot hitting the glass plate most of the time. Later in the record, the scan of the laser spot was near the middle of the wafer and the detector signal corresponds to the spot hitting the wafer most of the time. The first 7000 pulses of the run are shown here. The complete wafer required 27,000 pulses.

In the complete scan of the wafer, there were no laser pulse dropouts. The modulation of the detector signal was 10% of the basic signal, and the variability of the laser energy remained

within  $\pm 5\%$  for the complete scan of the wafer. Monitoring records of the small scale excimer laser such as this one were made for an equivalent total of more than  $10^6$  pulses and no laser dropouts occurred. The programming software was designed to remember the extreme high and low values of laser energy and these fell within  $\pm 5\%$  of the mean for an interval that corresponds to a 4" square wafer.

#### 3.5.1.4 Wafer Processing

This section presents a description of the experimental procedure used in laser annealing of wafers for junction formation, a tabulation of the laser parameters for each of the 62 batches of wafers that were processed, and a discussion of key observations that were made in the course of the study. Major changes in the experimental setup are noted in the remarks column of the parameter tables.

Table 3-1 shows an overview of the excimer laser annealing parameters during the course of the project. Unless otherwise noted, each batch represents one wafer being processed. A given wafer may have been of 3" or 4" diameter as noted in the dimensions in Section 4.0. In general, each wafer was processed to form three or four 2 cm x 2 cm cells depending on the original wafer size. The tables in Section 4.0 give a detailed listing of the final values found for the solar cell parameters in each batch.

The experimental procedure began with rechecking mirror alignment of the excimer laser and operating the laser for about 15 minutes at 20 Hz to establish steady performance. The rest of the optical arrangement was then checked for proper alignment using first a He-Ne laser arranged collinear with the excimer beam, and then the excimer laser. The laser energy per pulse was then determined, both at the wafer and directly out of the laser. Next the optical system was adjusted to establish a sharply focused spot having dimensions that yielded the desired laser energy density ( $\text{J}/\text{cm}^2$ ) at the wafer. The focus and spot size at the wafer were determined using the imprint pattern observed on photosensitive paper and also on an ion implanted wafer. The pulse waveform was recorded both before and after a batch of wafers was processed.

The wafers were prepared for laser annealing. With no further cleaning, a wafer was placed on the x-y table using nylon tweezers and contacting only the edge of the wafer. To remove dust specks on the surface, a helium gas stream was used. Later (after Batch 56) an electrostatic cleaning device was included in the gas stream used to remove residual surface dust from wafers. Also, after Batch 56, a plastic enclosure was used over the wafer, the x-y table, and the optics to minimize dust during laser processing of the wafer and to permit a controlled atmosphere ( $\text{N}_2$  or He or Ar) at the wafer surface.

Table 3-1  
EXCIMER LASER ANNEALING PARAMETERS

LASER ENERGY mJ	SPOT SIZE, mm x mm*	AVERAGE ENERGY DENSITY, J/cm <sup>2</sup>	TABLE SPEED, cm/sec	SPOT INTERVAL, mm x mm*	OVERLAP, PERCENT*	LASER PRP, sec <sup>-1</sup>	REMARKS
Batch 1:							
5	0.6 x 0.4	2.0	1.2	0.4 x 0.3	30	31	4 nsec
Batch 2:							
6	1.1 x 0.8	0.7	2.5	0.6 x 0.45	45	42	6 nsec
Batch 3:							
7	1.1 x 0.8	0.8	2.5	0.8 x 0.6	25	31	6 nsec
Batch 4:							
6	1.1 x 0.8	0.7	2.5	0.55 x 0.4	50	45	6 nsec
Batch 5: 4 Wafers							
6	1.1 x 0.8	0.7	2.5	0.55 x 0.4	50	45	6 nsec
5	1.3 x 1.0	0.4	2.5	0.4 x 0.25	70	65	6 nsec
4	0.8 x 0.6	0.8	2.5	0.25 x 0.25	70 x 60	100	6 nsec
7.5	0.8 x 0.6	1.5	1.2	0.25 x 0.20	70	50	6 nsec
Batch 6: 1 Spin-on, 1 Ion Implant							
11	1.0 x 0.9	1.2	2.5	0.5 x 0.45	50	60	25 nsec**
11	1.0 x 0.9	1.2	2.5	0.5 x 0.45	50	50	25 nsec
Batch 7: Etched, Spin-on Wafers							
9	1.0 x 1.0	0.9	2.5	0.5 x 0.5	50	50	25 nsec
11.3	1.0 x 0.95	1.2	2.5	0.5 x 0.5	50	50	25 nsec
11.3	0.9 x 0.8	1.6	2.5	0.45 x 0.4	50	55	25 nsec

\* First number corresponds to spot dimension along direction of simultaneous table travel and laser firing.

\*\* The 25 nsec laser pulse was composed of 2 pulses spaced 25 nsec, each having a FWHM duration of 6 to 10 nsec.

Table 3-1 (continued)

LASER ENERGY mJ	SPOT SIZE, mm x mm*	AVERAGE ENERGY DENSITY, J/cm <sup>2</sup>	TABLE SPEED, cm/sec	SPOT INTERVAL, mm x mm*	OVERLAP, PERCENT*	LASER PRP, sec <sup>-1</sup>	REMARKS
Batch 8: Texture Etched, Spin-on Wafers							
12	1.3 x 1.3	0.7	2.5	0.4 x 0.4	70	62	25 nsec
12	1.7 x 1.6	0.44	2.5	0.5 x 0.45	70	50	25 nsec
10	1.7 x 1.6	0.36	2.5	0.5 x 0.45	70	50	6 nsec
Batch 9: 5 keV Ion Implant, 2 Wafers							
12	0.95 x 0.95	1.3	2.5	0.3 x 0.3	70	77	25 nsec**
11	1.2 x 1.0	0.9	2.5	0.4 x 0.3	70	62	25 nsec
Batch 10: 2 Ion Implant, 1 Spin-on							
5.6	0.85 x 0.7	0.9	2.5	0.6 x 0.5	30	42	25 nsec
5.6	0.75 x 0.6	1.25	2.5	0.6 x 0.5	20	42	25 nsec
5.4	0.75 x 0.6	1.2	2.5	0.6 x 0.5	20	42	25 nsec
Batch 11: Ion Implant							
900***	9 x 7.5	1.3	---	7.2 x 6.4	20	--	80 nsec
Batch 12: Ion Implant Wafer							
1200	9.1 x 7.7	1.65	---	8.4 x 6.8	8	--	90 nsec
1200	9.1 x 7.7	1.65	---	8.4 x 6.8	8	--	90 nsec
Batch 13: Ion Implant							
1100	11.8 x 10	0.95	---	10.7 x 9.0	10	--	90 nsec

\*\*\* Parameters varied over wafer. Values listed correspond to region that gave best cell.

Table 3-1 (continued)

LASER ENERGY mJ	SPOT SIZE, mm x mm*	AVERAGE ENERGY DENSITY, J/cm <sup>2</sup>	TABLE SPEED, cm/sec	SPOT INTERVAL, mm x mm*	OVERLAP, PERCENT*	LASER PRF, sec <sup>-1</sup>	REMARKS
Batch 14: 2 Ion Implant Wafers							
1220	11.4 x 9.8	1.1	---	10.7 x 9.0	8	--	90 nsec
1220	11.4 x 9.8	1.1	---	10.7 x 9.0	8	--	90 nsec
Batch 15: Thermal Diffused Control							
1220	10.3 x 9.0	1.3	---	9.3 x 8.0	10	--	90 nsec
Batch 16: 2 Ion Implant							
1140	9.6 x 8.3	1.45	---	8.4 x 7.2	12	--	90 nsec
Batch 17: 2 Ion Implant							
1020	8.9 x 7.5	1.55	---	8.0 x 6.6	12	--	90 nsec
Batch 18: 1 Ion Implant							
1000	7.5 x 6.5	2.0	---	6.4 x 5.7	12	--	90 nsec
Batch 19: 1 keV Ion Implant							
1080	9.0 x 8.0	1.5	---	8.0 x 7.0	12	--	90 nsec
Batch 20: 5 keV Ion Implant; CVD Surface Dopant							
1000	8.0 x 6.9	1.8	---	7.0 x 6.1	12	--	90 nsec
940		1.7					
Batch 21: 1 keV Ion; P <sup>+</sup> Thermal Dep; 10 keV B <sup>+</sup> ; 5 keV P <sup>+</sup> Ion; 50 keV P <sup>+</sup> Ion							
13	1.3 x 1.2	0.8	2.5	0.9 x 0.7	30	--	Small Laser With Beam Homogenizer (Kaleidoscope) 30 nsec
13	1.3 x 1.2	0.8		0.9 x 0.7	30	--	
13	1.3 x 1.2	0.8		0.9 x 0.7	30	--	
13	1.1 x 0.9	1.3		0.5 x 0.35	50	--	

Table 1 (continued)

LASER ENERGY	SPOT SIZE, mm x mm*	AVERAGE ENERGY DENSITY, J/cm <sup>2</sup>	TABLE SPEED, cm/sec	SPOT INTERVAL, mm x mm*	OVERLAP, PERCENT*	LASER PRF, sec <sup>-1</sup>	REMARKS
Batch 22: 4 5-keV Ion Implant							
13	0.8 x 0.8	2.0	1.2	0.64 x 0.64	20	--	Kaleidoscope Face Damage Seen Laser PRF 20 Hz
14	0.95 x 0.9	1.6	1.2	0.75 x 0.7	20	--	New Kaleidoscope Slight Damage on Wafers
14	0.95 x 0.9	1.6	1.2	0.48 x 0.45	50	--	
Batch 23: 3 5-keV Ion Implant							
10	0.9 x 0.85	1.3	1.2	0.40 x 0.38	50	--	Low Laser Reliability High Intensity at End of Pulse
10	0.9 x 0.85	1.3	1.2	0.40 x 0.38	50	--	
10	1.0 x 0.95	1.1	1.2	0.45 x 0.42	50	--	
Batch 24: 3 5-keV Ion Implant							
12	0.95 x 0.9	1.4	0.8	0.45 x 0.42	50	--	Good Laser Reliability and Pulse Shape 30 nsec
12	0.95 x 0.9	1.4	0.8	0.45 x 0.42	50	--	
12	0.95 x 0.9	1.4	0.8	0.45 x 0.42	50	--	
Batch 25: 1 5-keV n-Type; 1 Thermal Dep; 1 5-keV p-Type							
13	0.95 x 0.9	1.52	0.8	0.45 x 0.43	50	--	30 nsec
Batch 26: 3 5-keV Ion Implant p-Type							
15.5	1.05 x 1.0	1.45	0.8	0.53 x 0.5	50	--	Clean Wafers 30 nsec



Table 3-1 (continued)

LASER ENERGY mJ	SPOT SIZE, mm x mm*	AVERAGE ENERGY DENSITY, J/cm <sup>2</sup>	TABLE SPEED, cm/sec	SPOT INTERVAL, mm x mm*	OVERLAP, PERCENT*	LASER PRP, sec <sup>-1</sup>	REMARKS
Batch 27: Back of n-Type Wafer							
13.5	0.7 x 0.7	2.7	0.7	0.35 x 0.33	50	--	Not Sharp Focus 30 nsec
Batch 28: 3 5-keV p-Type							
14	1.0 x 0.95	1.47	1.0	0.48 x 0.45	50	--	Less Uniform Beam than Batch 26
Batch 29: 1 5-keV n-Type							
15	1.05 x 1.0	1.43	0.8	0.40 x 0.38	60	--	Fuzzy at Edges of Spot
Batch 30: 2 5-keV p-Type							
15	1.05 x 1.0	1.43	0.8	0.40 x 0.38	60	--	Fuzzy at Edges of Spot
Batch 31: 1 5-keV n-Type, 1 5-keV p-Type							
15	1.05 x 1.0	1.43	0.8	0.4 x 0.38	60	--	Fuzzy at Edges
14	1.05 x 1.0	1.42	0.8	0.4 x 0.38	60	--	30 nsec
Batch 32: Spin-on Back of n-Type Wafer							
15	0.8 x 0.75	2.45	0.8	0.4 x 0.38	50	--	Not Sharp Focus 30 nsec
Batch 33: Spin-on p-Type							
11	1.05 x 1.0	1.3	1.0	0.5 x 0.45	50	--	Sharp Focus, Wider Pulse
12.5	1.05 x 1.0	1.2	1.0	0.5 x 0.45		--	Waveform 35 nsec

Table 3-1 (continued)

LASER ENERGY mJ	SPOT SIZE, mm x mm <sup>2</sup>	AVERAGE ENERGY DENSITY, J/cm <sup>2</sup>	TABLE SPEED, cm/sec	SPOT INTERVAL, mm x mm <sup>2</sup>	OVERLAP, PERCENT*	LASER PRF, sec <sup>-1</sup>	REMARKS
Batch 34: 1 keV p-Type; 1 Spin-on							
13	1.0 x 0.9	1.44	0.6	0.5 x 0.45	50	--	Same as 33
Batch 35: 5 keV p-Type; 2 Thermal Diffusion							
13	0.9 x 0.9	16	0.9	0.45 x 0.45	50	--	40 nsec
Batch 36: 5 keV p-Type							
12	0.95 x 0.95	1.33	0.9	0.45 x 0.45	50	--	40 nsec
Batch 37: 5 keV Ion Implant							
14	1.0 x 1.0	1.4	1.0	0.5 x 0.5	50	--	25 nsec
Batch 38: 4 5-keV Ion Implant							
14.5	1.0 x 1.05	1.4	1.0	0.5 x 0.55	50	--	25 nsec
13.5	1.0 x 1.05	1.3	1.0	0.5 x 0.55	50	--	25 nsec
Batch 39: 3 5-keV Ion Implant							
14	1.0 x 1.0	1.4	1.0	0.5 x 0.5	50	--	25 nsec
13	1.0 x 1.0	1.3	1.0	0.5 x 0.5	50	--	25 nsec
Batch 40: n-Type 5 keV Front, 35 keV Back; Spin-on Back							
14.5	1.0 x 1.05	1.4	1.0	0.5 x 0.55	50	--	25 nsec
14	0.75 x 0.75	2.5	0.8	0.4 x 0.4	50	--	25 nsec
14	0.75 x 0.75	2.5	0.8	0.4 x 0.4	50	--	25 nsec

Table 3-1 (continued)

LASER ENERGY eV	SPOT SIZE, mm x mm*	AVERAGE ENERGY DENSITY, J/cm <sup>2</sup>	TABLE SPEED, cm/sec	SPOT INTERVAL, mm x mm*	OVERLAP, PERCENT*	LASER PRP, sec <sup>-1</sup>	REMARKS
Batch 41: 2 2-keV Ion Implant; 1 Spin-on Back; Repeat Back on 2 Wafers							
14	0.95 x 1.0	1.45	1.0	0.47 x 0.5	50	--	25 nsec
14	0.75 x 0.8	2.3	0.8	0.25 x 0.4	50	--	25 nsec
14	0.6 x 0.65	3.5	0.6	0.25 x 0.25	60	--	25 nsec
Batch 42: 2 5-keV Ion Implant Quadrants							
13.5	0.95 x 0.95	1.5	1.2	0.38 x 0.38	50	--	25 nsec
Batch 43: 5 Quadrants							
14	0.9 x 1.0	1.5	0.9	0.36 x 0.4	50	--	25 nsec
Batch 44: 2 5-keV Wafer							
14	0.92 x 1.0	1.5	0.9	0.36 x 0.4	50	--	25 nsec
Batch 45: 2 5-keV Wafers							
14.5	0.92 x 1.0	1.55	0.9	0.36 x 0.4	50	--	25 nsec
14.5	1.0 x 1.05	1.1	1.0	0.4 x 0.42	50	--	25 nsec
Batch 46: 1 Zymet Ion Implant							
14.5	1.0 x 1.05	1.4	1.0	0.4 x 0.42	50	--	25 nsec
Batch 47: 1/2 of Front of P-Type Wafer							
14	0.95 x 1.0	1.45	1.1	0.47 x 0.5	50	--	Little Surface Damage

Table 3-1 (continued)

LASER ENERGY mJ	SPOT SIZE, mm x mm*	AVERAGE ENERGY DENSITY, J/cm <sup>2</sup>	TABLE SPEED, cm/sec	SPOT INTERVAL, mm x mm*	OVERLAP, PERCENT*	LASER PRF, sec <sup>-1</sup>	REMARKS
Batch 48: Other 1/2 from Batch 47, After Recleaning; 3 p-Type Quadrants							
14	0.95 x 1.0	1.45	1.1	0.47 x 0.5	50	--	Strong Surface Damage
13.5	0.92 x 0.98	1.5	1.1	0.45 x 0.47	50	--	
13.5	0.92 x 0.98	1.5	1.1	0.45 x 0.47	50	--	
13.5	0.92 x 0.98	1.5	1.1	0.45 x 0.47	50	--	
Batch 49: 4 p-Type Quadrants, Different Surface Treatment							
13.5	0.90 x 0.97	1.5	1.1	0.47 x 0.50	50	--	All Showed Normal
13.5	0.90 x 0.97	1.5	1.1	0.47 x 0.50	50	--	Color Change Due
13.5	0.90 x 0.97	1.5	1.1	0.47 x 0.50	50	--	to Laser; Some
13.5	0.90 x 0.97	1.5	1.1	0.47 x 0.50	50	--	Surface Damage
Batch 50: 1 p-Type Quadrant and 1 p-Type 4" Square Wafer							
13.5	0.90 x 0.97	1.53	1.1	0.45 x 0.47	50	--	Scan Interrupted;
13.5	0.90 x 0.97	1.53	1.1	0.45 x 0.47	50	--	Weak Color Change
Batch 51: 2 p-Type 3 Inch Rounds, P <sub>2</sub> <sup>+</sup> Ion Implant; 4 Quadrants, P <sub>1</sub> <sup>+</sup> Implant							
13.5	0.90 x 1.0	1.5	1.1	0.45 x 0.47	50	--	Normal Color Change
Batch 52: 4 Quadrants, 1 3-Inch Round							
14	0.92 x 0.98	1.55	1.1	0.47 x 0.50	50	--	Some Surface Damage
	0.92 x 0.98	1.55	1.1	0.47 x 0.50	50	--	Cleaned Particles Out of Laser
	0.92 x 0.98	1.55	1.1	0.45 x 0.47	50	--	Before Starting
	0.92 x 0.98	1.55	1.1	0.45 x 0.47	50	--	
13	0.92 x 0.98	1.43	1.1	0.45 x 0.47	50	--	

Table 3-1 (continued)

LASER ENERGY mJ	SPOT SIZE, mm x mm*	AVERAGE ENERGY DENSITY, J/cm <sup>2</sup>	TABLE SPEED, cm/sec	SPOT INTERVAL, mm x mm*	OVERLAP, PERCENT*	LASER PRP, sec <sup>-1</sup>	REMARKS
Batch 53: 5 Quadrants, Various Surface Treatments							
14	0.92 x 0.98	1.55	1.1	0.45 x 0.47	50	--	1 Wafer Showed no Color Change
Batch 54: 4 p-Type Quadrants and 2 3" Dia. p-Type Rounds							
14	0.93 x 0.98	1.53	1.1	0.45 x 0.47	50	--	Significant Surface Damage Seen
Batch 55: 4 p-Type Quadrants and 2 3" Dia. p-Type Rounds							
13	0.93 x 0.98	1.42	1.1	0.47 x 0.50	50	--	Slight Surface Damage Seen
Batch 56: 2 p-Type Quadrants and 2 3" Dia. p-Type Rounds							
13.6	0.95 x 1.0	1.43	1.1	0.47 x 0.50	50	--	Computer Failure in Middle of 2nd Quadrant
Batch 57: 2 p-Type Quadrants							
15.8	1.05 x 1.0	1.5	1.1	0.50 x 0.45	50	--	Modified Optics; Slight Damage
Batch 58: 2 p-Type Quadrants							
15.8	1.05 x 1.0	1.5	1.1	0.50 x 0.45	50	--	Slight Damage
Batch 59: 5 p-Type Quadrants, 2 Old, 3 From New Batch with 1.8 x 10 <sup>15</sup> cm <sup>-2</sup> p <sup>+</sup> Dose at 5 keV							
15.2	1.03 x 1.0	1.47	1.1	0.50 x 0.47	50	--	Slight Scribe Lines on Old Wafer, More Definite on New Batch

Table 3-1 (continued)

LASER ENERGY mJ	SPOT SIZE, mm x mm*	AVERAGE ENERGY DENSITY, J/cm <sup>2</sup>	TABLE SPEED, cm/sec	SPOT INTERVAL, mm x mm*	OVERLAP, PERCENT*	LASER PRF, sec <sup>-1</sup>	REMARKS
Batch 60: 18 p-Type Quadrants, 5 keV Ion Implant, Various Doses							
15.2	1.03 x 1.0	1.47	1.1	0.50 x 0.47	50	--	Using N <sub>2</sub> Atmosphere Over Wafer
Batch 61: 10 p-Type Quadrants, 5 keV Ion Implant at 2.5 x 10 <sup>15</sup> Doses							
15.2	1.03 x 1.0	1.47	1.1	0.50 x 0.47	50	--	Changed from N <sub>2</sub> to Ar as Atmosphere Over Wafer
Batch 62: 9 p-Type, 5 keV at 1.8 x 10 <sup>15</sup> , 13 p-Type, 5 keV at 2.5 x 10 <sup>15</sup>							
15	1.03 x 1.0	1.45	1.1	0.5 x 0.47	50	--	Last 5 Wafers Down to 1.40 J/cm <sup>2</sup>

The laser was rechecked for power output and, if not within 5% of the original power output, adjustments were made either on the laser or the optical beam handling system to re-establish the desired laser energy density. The computer commands were entered to determine step size between laser pulses, row length to cover the wafer, and x-y table speed to obtain ~20 Hz laser repetition rate. The automated laser processing scan of the wafer was initiated. During wafer processing, any visible fluorescence from the wafer and from the adjacent glass surface was observed by eye, and the photodiode monitor of laser pulse energy was watched to assure proper operation of the laser. The laser annealing process could be observed by the change in reflection characteristics on the wafer as laser annealing changed the state of the silicon surface material from amorphous to single crystal. After completion of laser annealing, the wafer was carefully removed from the x-y table, placed in a sample box and shipped the same day by overnight mail for further processing and testing.

Sixty-two groups of wafers in total were excimer laser processed for purposes of junction formation during this project. Details of the laser and x-y table operating parameters are listed in Table 3-1 for each set of experiments. Various laser energy densities and spot overlap factors were investigated, as well as a number of different types of wafers and surface dopant application methods. Wafers that were ion implanted showed little or no luminosity of the surface when laser annealed, whereas spin-on materials exhibited significant luminosity due to laser heating. The imprint of the laser beam, with its residual spatial nonuniformities, was readily visible on textured wafers and on wafers that had spin-on material on the surface. Following these observations of surface damage on textured and/or spin-on material, further studies were directed toward polished wafers that were ion-implanted with phosphorus or boron dopant.

Using the small laser, the total number of laser pulses accumulated was more than  $10^6$ . The spot pattern could be recognized on all samples due to a change in surface reflection characteristics. We saw no evidence of a single missed spot. With the large laser there was an occasional missed spot due to a trigger or switch malfunction. However, during processing the wafer was inspected after each laser pulse and the missing spot was filled in before moving on to the next spot.

The beam homogenizer was added to the small laser optical arrangement after Batch 20. We found that the input end of the rectangular quartz kaleidoscope could be damaged by high laser repetition rate or by focusing the laser to too small a spot in the quartz. For this reason wafer processing was limited to laser repetition rates of less than 25 Hz, and the optical throughput was less than optimum because of clipping of the beam at the entrance aperture of the kaleidoscope.

After annealing with the large laser, the wafer from Batch 18

showed slight surface damage in some areas, indicating a threshold for damage of about  $2.0 \text{ J/cm}^2$  when using a 90 nsec pulse duration. In the case of the small laser with a 30 nsec pulse duration, damage was observed on the surface of the wafers at about  $1.5 \text{ J/cm}^2$ , especially at the edges of the spot. One factor affecting the damage threshold is the laser pulse shape. The damage threshold was lower (about  $1.2 \text{ J/cm}^2$ ) for the pulse shape shown in Fig. 3-14(a), whereas it was about  $1.5 \text{ J/cm}^2$  for the laser pulse shape of Fig. 3-14(b). The high intensity late in the pulse of Fig. 3-14(a) may have produced excessive vaporization and surface damage.

Good solar cell results were obtained from the wafers processed in Batch 24. Just prior to this test the laser had been disassembled to determine the reason for excessive shot-to-shot variability. The screen electrode was smoothed and the laser mirrors were cleaned. In addition, the resistor in series with the corona bar was reduced, thereby increasing the strength of the UV preionization and improving the reproducibility of the electrical discharge in the laser gas.

Even better solar cell results were obtained from the wafers processed in Batch 26, although there were slight residual damage marks on the wafer surface at the edges of each laser spot. The laser pulse waveform used in these experiments is shown in Fig. 3-15(a). The overall pulse duration was 30 nsec, with the higher intensity during the early part of the pulse. The laser spot was sharply focused on the wafer, was square, and the overlap was set carefully to 50 percent in both directions. Highest cell efficiency was obtained with a 5 keV,  $2.5 \times 10^{15} \text{ cm}^{-2}$  phosphorus ion implant using Cz wafers that had been cleaned prior to the laser processing.

Following Batch 27, a careful study was made of the laser intensity distribution, both spatial and temporal, at the exit of the kaleidoscope and also at the location of the wafer surface. Particularly close attention was directed at the edges of the spot to see if the intensity or pulse shape was altered in a way that would induce surface damage specifically at the edge of each spot. A fast response photodiode recorded the laser intensity from the portion of the laser beam transmitted through a 25 micron pinhole, mounted on an x-y-z micropositioning assembly. In addition, the surface damage on 5 keV ion implanted wafers was examined as a function of the laser parameters such as energy density, laser pulse waveform, and edge sharpness of the spot on the wafer. The following observations were made:

1. No indications of laser intensity or pulse waveform changes near the edges of the spot were seen other than the expected falloff in intensity at the edges.
2. The top and bottom of the spot showed more abrupt intensity changes than did the sides. The damage to the wafer was more severe at the top and bottom edges. The laser output had greater



beam spread up and down, filling the kaleidoscope better and making the intensity gradient sharper at the output of the kaleidoscope.

3. Surface damage appeared to be essentially the same whether single spots were used, or multiple spots with 50 percent overlap.

4. By significantly defocusing the spot on the wafer it was possible to eliminate the edge damage that was observed. With higher laser energy density in the central portion of the spot (1.6 to 1.7 J/cm<sup>2</sup>) a speckle pattern of surface damage was seen, but with no edge damage noticeable.

5. Wafers with higher ion implant dose showed greater susceptibility to damage than wafers with low dose. Any surface film on the wafer reduced the damage threshold.

6. Slight luminosity was seen on the wafer surface as the laser spot impinged when the laboratory was darkened. The luminosity may have been due to vaporization of Si, P, or a thin residual surface layer such as SiO<sub>2</sub>.

It was concluded from these observations that the edge surface damage was due to vaporization of the surface and the resulting sharp pressure gradients at the edge of the spot caused by the sharp laser spot intensity gradients. Only at the edge could the vapor move laterally, causing movement of the surface melt layer during the brief (100 nsec) melt time. A simple calculation of the distance traveled by acoustic waves in the vapor during a period of 50 nsec yields an estimate for the width of the edge damage region of approximately 30 microns, which corresponds well to the width of the edge damage lines that were observed on these wafers.

Experiments confirmed that two effects, namely laser intensity gradients and volatile surface contaminants, played a role in the amount of surface damage produced. For constant laser processing conditions, variations in the wafer cleaning procedure influenced the amount of surface damage, indicating that sometimes there was some volatile material present on the surface at the time of laser processing. Similarly, wafers that were cleaned the same way showed that the amount of damage produced was very sensitive to the laser energy density, even over the narrow range from 1.4 J/cm<sup>2</sup> to 1.5 J/cm<sup>2</sup>, and to the sharpness of focus.

After obtaining good solar cell results from the wafers of Batch 26, later results were not as good and an effort was made to duplicate the results of Batch 26. Differences in laser parameters between Batch 26 and later experiments may have been responsible for this change in results. The following changes in the laser had been made:

1. The pulse waveform for Batch 26 was shown in Fig. 3-15(a)

whereas the later waveform was shown in Fig. 3-15(b). The overall pulse duration in the two cases is 25 nsec but there is some difference in the waveforms.

2. Following Batch 37, the optical arrangement for focusing the output of the beam homogenizer onto the wafer was intended to improve by adding a second lens. Improved focus produced sharper images, which could have larger gradients in intensity at the wafer surface if the output from the beam homogenizer is nonuniform. The quartz surface at the output of the homogenizer was well polished, but still showed many fine scratches and tiny marks.

3. After Batch 37 and before Batch 43, the beam homogenizer being used was damaged and was replaced with one that had not been as well polished on the ends by the supplier. The finely structured nonuniformities on the output end were focused onto the wafer and may have contributed to surface damage.

Following Batch 56, we modified the optical arrangement to reproduce the setup used for Batch 26. The second lens, having short focal length, was removed, and a high quality beam homogenizer was substituted for the one with poor quality. No change in pulse waveform was attempted. The resulting laser spot appeared very uniform across the central region covering 80 to 90 percent of the linear span. However, the intensity at the edges of the spot decreased over a larger distance than when the dual lens arrangement was used for refocusing the output of the beam homogenizer onto the wafer. The laser spot size was approximately 1 mm by 1 mm, and the linear dimension for the laser intensity to fall from 90% to 10% of the maximum value was about 0.1 mm.

The observed damage on wafers that were laser annealed was similar to that obtained in Batch 26; there was very little or no damage over the central portion of each spot, with noticeable short line segments of damage at the four edges of each spot. These observations regarding surface damage indicate that the differences were due primarily to the optics and not to the differences in pulse waveform or to surface cleanliness.

At the time of installation of the high quality beam homogenizer, the square output face was not oriented to be in registry with the directions of travel of the motorized table carrying the wafer. As a result, the edges of the spots were about 5° off from being parallel and perpendicular with the directions of travel. This effect reduced the uniformity of overlap of the laser spots and led to regions of nonuniformity in the integrated laser energy dose applied to the wafer surface. This misalignment was noticed after Batch 58 and was then corrected.

In order to reduce the possibility of accumulation of dust particles on the wafer during the laser annealing process, a dust cover was placed over the optical assembly and wafer translation

tables. This enclosure was purged with high purity air from a high pressure gas storage tank. The air was introduced into the enclosure through an electrostatic air filter. Visual observation of the helium-neon alignment laser showed no evidence of dust in the air in the enclosure. However, even with these precautions, and the use of dust free air flow over the wafer to remove surface dust prior to installation on the translation table, luminous specks were occasionally observed on the wafer surface during the laser annealing process. These specks of luminosity occurred when the UV laser impinged on dust or other material clinging to the surface. These regions can produce shadowing of the laser beam, additional surface damage on the wafer, and impurities incorporated into the junction. All of these effects can degrade performance of the final solar cells produced by the use of laser annealing to form the junction.

### **3.5.2 UV Laser Metallization**

Laser photodeposition experiments for the metallization process step were investigated using both tungsten and aluminum containing gas carriers. The excimer laser was operated at 193 nm and was characterized with regard to energy per pulse, pulse waveform, optical attenuation from the laser to the wafer, and focal line dimensions at the wafer. Procedures for operating the WF<sub>6</sub> and Al(CH<sub>3</sub>)<sub>3</sub> gas supplies were established. Several wafers and glass slides were processed at various laser energy densities and gas compositions and pressures in order to determine the sticking characteristics and the chemical composition of the lines that were deposited by this method. Both W and Al lines that were ~1000Å thick and which could pass the adhesive tape adherence test were successfully deposited. However, analysis of the metal deposits using Auger spectroscopy revealed that both the W and Al deposits consisted primarily of metal oxides. Efforts to reduce the oxidation using flowing gas during the wafer processing were not successful and the source of the oxygen contamination is not known.

Laser sintering of silicon wafers plated with titanium, palladium, and silver layers was investigated to see if laser heating of the surface would bond the plated metal to the silicon. Laser photodecomposition of silicon wafers coated with a solid organic-silver compound was also investigated to see if silver could be deposited on the wafer using a pulsed UV laser. Several wafers were processed at various energy densities, pressures, and temperatures in order to determine the adhesion properties and chemical composition of the photodeposited lines.

#### **3.5.2.1 Excimer Laser Characteristics**

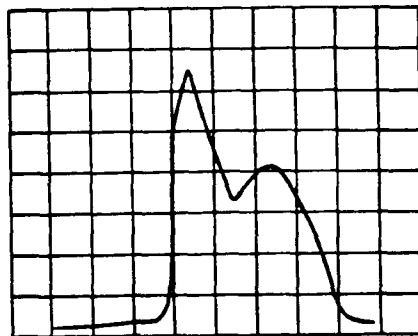
Shortly after beginning laser CVD metallization experiments (following Batch 5) a corona bar failure on the laser required repair. Along with repair of the corona bar, the laser was cleaned and the anode electrode profile was modified by substituting a new standard EXC-1 anode which had a more rounded

contour. These changes produced better 193 nm laser performance and the laser was characterized in this form.

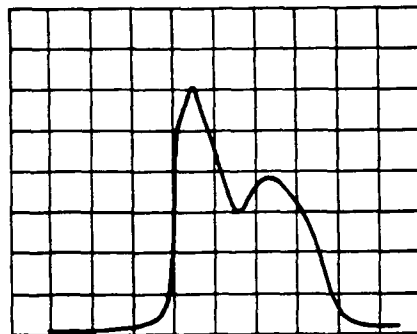
The energy per pulse was typically 20 mJ and the pulse waveform was a double peak having a 30 nsec full width, half maximum duration, as shown in Fig. 3-24. The gas lifetime was limited to 250 to 500 shots before the energy fell off by 25% due to gas contaminants that build up in the laser chamber. The gas life steadily improved with the number of gas fills. Gas life is much better (by a factor of 100 to 1000) on lasers that have been operated with  $F_2$ , but not with  $HCl$ , in the gas mixture.

The laser beam attenuation was a factor of 2 between the laser output and the wafer surface. This loss was made up of 90% reflectivity from each of 3 turning mirrors (including aperture clipping), 10% absorption in ambient air at 193 nm, 85% transmission through the uncoated quartz window, and 90% transmission through the cylindrical lens.

The focal spot size at the wafer was 1 to 2 cm long by 0.1 mm wide. With the laser operating at 20 mJ per pulse and 50% loss through the optics, the average laser energy density incident on the wafer was 0.5 to 1.0 J/cm<sup>2</sup>. This value was high enough to bring the silicon surface to or near the melting point. A 50% attenuator at 193 nm was available to decrease the applied energy density by a factor of 2.



a. Fresh gas 21 mJ pulse energy



b. After 250 pulses 20 mJ pulse energy

**Fig. 3-24.** Laser pulse waveforms measured after Batch 9, and obtained after laser repair following Batch 5.

### 3.5.2.2 Gas Supply Procedure

A static gas fill approach was used initially in the metallization experiments. After evacuating and flushing all lines and the process chamber with argon, an intermediate gas storage chamber was pressurized (to 5 psia) with  $\text{WF}_6$  and another chamber was pressurized (to 8 psia) with  $\text{H}_2$ . Either of these gases could be added into the process chamber at low pressure (~1 torr) by first filling a short line segment to the pressure of the intermediate chamber and then transferring this limited volume of gas into the process chamber. Higher partial pressure of either gas was obtained by repeating the procedure. If both gases were introduced, a brief time (a few minutes) for mixing in the chamber was allowed, which is sufficient when the total gas pressure was under 20 torr. The chamber was pumped down to less than 5 mtorr and the observed outgasing rate was less than 1 to 2 mtorr per minute.

The  $\text{Al}(\text{CH}_3)_3$  was stored as a liquid with an inert gas overpressure. For each usage the inert gas was exhausted and an intermediate line was filled with  $\text{Al}(\text{CH}_3)_3$  to its vapor pressure (9 torr at  $20^\circ\text{C}$ ) and then transferred into the chamber.  $\text{H}_2$  also could be added as described above. Following the day's experiments the storage bottle of  $\text{Al}(\text{CH}_3)_3$  was repressurized with argon to about 1 atm.

Later experiments used a steady flow through the chamber in order to reduce the depletion of  $\text{WF}_6$  and to minimize contamination by  $\text{O}_2$ . The mixture ratio was set by adjusting the mass flow of each constituent with the flow controllers on the gas handling system. The total pressure was then set by manually turning the pump-out valve on and off while monitoring the total pressure with a mechanical pressure gauge (0-50 torr).

### 3.5.2.3 Wafer Processing

The same remarks found in Section 3.5.1.4 regarding batch size and number of cells apply in this section.

The first experiments utilized  $\text{WF}_6$  as the process gas. Review of the literature yielded the ultraviolet optical absorption curve<sup>2</sup> shown in Fig. 3-25. At 193 nm the absorption cross section is  $3.5 \times 10^{-19} \text{ cm}^2$ , requiring a partial pressure of 85 torr to reach an absorption coefficient of  $1 \text{ cm}^{-1}$ . Much lower pressures were used to minimize the production of particles in the gas following photodecomposition by the laser. The absorption coefficient for  $\text{Al}(\text{CH}_3)_3$  at 193 nm is much larger.<sup>3</sup>

The x-y table carrying the optics was controlled by manually entering commands to the stepper motor control box. A series of adjacent lines parallel to each other could be applied to the wafer at any desired spacing. In initial experiments the lines were spaced by 0.2 inches to assure that each line was independent. Spacing closer than 0.1 inches led to overlap of

deposition on the window, which interfered with passage of the laser beam through the window when one line followed a previous line.

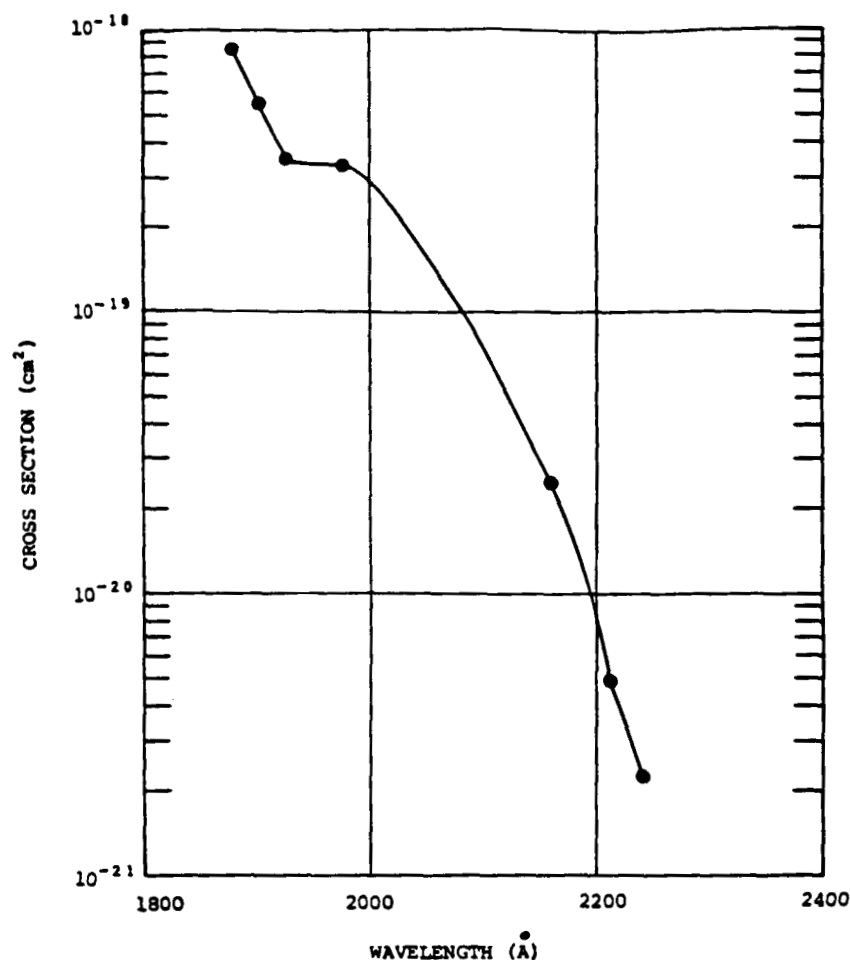


Fig. 3-25.  $WF_6$  absorption cross section.

The parameters used in the initial metallization experiments conducted without flowing gas are listed in Table 3-2. Both W and Al lines that were  $\sim 1000\text{\AA}$  thick and which could pass the tape adherence test were successfully deposited. However, analysis of the metal deposits using Auger spectroscopy revealed that both the W and Al deposits consisted of metal oxides rather than pure metal.

Wafers were then processed using the best conditions identified in the static gas experiments, except that extra effort was expended to eliminate oxygen from the system. All of the gas lines were pumped out and flushed several times, the chamber was passivated by exposure to  $WF_6$  or  $Al(CH_3)_3$ , and the gas was flowed during processing to eliminate contamination from small air

leaks. The parameters used in these metallization experiments are summarized in Table 3-3.

A preliminary investigation was also made of fine line metallization by using the pulsed ArF laser ( $\lambda = 193$  nm) to either sinter a plated metal onto the silicon wafer or to photodecompose a solid metal organic compound that had been applied to the wafer. The wafers for sintering had been plated with layers of Ti, Pd, and Ag. The sintering was done at room temperature in air and laser energy densities of  $\sim 1.5$  and  $0.8$  J/cm<sup>2</sup> with various numbers of shots investigated. Visible marks were made on the metal surface by the laser. The parameters investigated are listed in Table 3-4.

The photodecomposition experiments were done with wafers coated with silver neodecanoate. The wafers were processed in air at atmospheric pressure and at both room temperature and  $\sim 70^\circ\text{C}$  to promote better adhesion. Two apertures were placed in the laser beam outside of the cavity in order to obtain a sharper focus and to improve the uniformity by removing weak light at the edges of the beam. This light probably arises from a diamond mode parasitic oscillation involving reflection from the laser electrodes. Exposing the silver neodecanoate to the laser caused dust to be ablated from the wafer and left visible lines of shiny, reflective material deposited on the wafer. In addition to a number of lines, several grids of lines were deposited to form cells for evaluation. The parameters used in these experiments are summarized in Table 3-4.

### 3.5.3 UV Laser Passivation

Passivation of Si solar cells by photodepositing SiO<sub>2</sub> from a SiH<sub>4</sub>/N<sub>2</sub>O mixture using an ArF ( $\lambda = 193$  nm) laser was investigated. Energy densities of  $0.02$  J/cm<sup>2</sup> and  $0.5$  J/cm<sup>2</sup> were investigated by using both an unfocused and loosely focused spot. Best results were obtained with the unfocused spot. The spots were overlapped by 50% in order to achieve better uniformity. For these experiments, the ArF laser beam impinged normal to the wafer surface rather than parallel to it as reported by Boyer, et al.<sup>4</sup> The conditions investigated are listed in Table 3-5. Because of time limitations the range of parameters was not extensive.

The first samples of SiO<sub>2</sub> that were deposited were found to contain a few percent nitrogen. In an effort to eliminate this impurity, O<sub>2</sub> and SiH<sub>4</sub> were mixed by diluting 2 torr of SiH<sub>4</sub> in 30 torr Ar and O<sub>2</sub> mixtures. Time limitations prevented optimization of the SiH<sub>4</sub>/Ar/O<sub>2</sub> mixtures. It should be noted that Mishima, et al have reported depositing SiO<sub>2</sub> by photolysis of Si<sub>2</sub>H<sub>6</sub> diluted in N<sub>2</sub> plus O<sub>2</sub> using a low pressure mercury lamp.<sup>5</sup> Later samples of SiO<sub>2</sub> deposited with SiH<sub>4</sub>/N<sub>2</sub>O mixtures did not show the nitrogen impurity.

Table 3-2  
Fine Line Metallization by Laser Photodeposition  
Laser Pulse Repetition Rate, 2 Hz

Laser Energy (mJ)	Number of Pulses and Lines	Image Size mm x mm	Donor Gas	Partial Pressure, Other		Partial Pressure, Torr	Pulse Duration, nsec	Remarks
				Torr	Gas			
Batch 1: (a) 3" round wafer; (b) quadrant; (c) glass slide								
4 (He diluent)	(a) 4 lines 100 or 200 pulses	0.1 x 20	WF <sub>6</sub>	4	H <sub>2</sub>	12	6	WF <sub>6</sub> gas degrades Dust on wafer
3	(b), 5 lines (c) 50,100,200, 500	0.1 x 20	WF <sub>6</sub>	4 2 1	H <sub>2</sub>	12 7 4	6 6 6	Dust over area Double line on glass Fine line on wafer
Batch 2: Untreated Quadrant								
3	3 lines, 2 with wafer heated 500 pulses	0.1 x 20	WF <sub>6</sub>	2	H <sub>2</sub>	4	6	WF <sub>6</sub> degrades with heat
Batch 3: Clean, Untreated Quadrant								
12 (Ne diluent)	3 lines 100,200,300	0.1 x 20	WF <sub>6</sub>	0 2	H <sub>2</sub>	0 5	not measured	Mark on wafer with no gas
Batch 4: 2 Clean, Bare, Polished Si Quadrants								
15	(1) 6 lines, 50 pulses; 3 lines, 250 pulses	0.1 x 12	WF <sub>6</sub>	2	H <sub>2</sub>	4	not measured	



Table 3-2 (continued)

Laser Energy (mJ)	Number of Pulses and Lines	Image Size mm x mm	Donor Gas	Partial Pressure, Torr	Other Gas	Partial Pressure, Torr	Pulse Duration, nsec	Remarks
15	(2) 6 lines, 50 pulses, 3 lines, 250 pulses	0.1 x 12	WF <sub>6</sub>	2	H <sub>2</sub>	4	not measured	Heated chamber 115 °C
Batch 5: Clean Quadrant; Thermal Diffused Quadrant								
16	4 lines each 50,250	0.1 x 12	WF <sub>6</sub>	4	H <sub>2</sub>	12	not measured	Double lines with center depressed
Batch 6: Clean Quadrant; Glass Slide								
10 or 5	4 lines on each 2 with no gas 100 pulses	0.1 x 12	WF <sub>6</sub>	3	H <sub>2</sub>	13	30	Laser corona bar and electrode repaired
Batch 7: Clean Quadrant; Glass Slide								
15 or 7	6 lines on each 100,250 pulses	0.1 x 12	Al(CH <sub>3</sub> ) <sub>3</sub>	1	H <sub>2</sub>	5	30	50% attenuator used for 1/2 energy
Batch 8: Thermal Diffused Quadrant; Glass Slide								
14 or 7	9 lines 250 pulses	0.1 x 12 0.2 x 12	Al(CH <sub>3</sub> ) <sub>3</sub>	4	H <sub>2</sub>	12	30	Solid lines plus dust

Table 3-2 (continued)

Laser Energy (mJ)	Number of Pulses and Lines	Image Size mm x mm	Donor		Partial Pressure, Torr		Partial Pressure, Torr		Pulse Duration, nsec	Remarks
			Gas		Torr		Torr			
Batch 9: Thermal Diffused Quadrant; Glass Slide										
18±2	11 lines	0.1 x 12	Al(CH <sub>3</sub> ) <sub>3</sub>		0		0		30	More deposition with argon
(50%	250 pulses	0.2 x 12			1		4			
atten..							400			
in place)										

Table 3-3  
Fine Line Metallization by Laser Photodeposition

LASER ENERGY (mJ)	NUMBER OF PULSES & LINES	IMAGE SIZE (mm)	DONOR GAS	PARTIAL PRESSURE (Torr)	OTHER GAS	PARTIAL PRESSURE (Torr)	PULSE DURATION (nsec)	REMARKS
Batch 10: Clean Untreated Quadrant								
20	a) 3 lines 250 pulses	0.1 x 12	Al(CH <sub>3</sub> ) <sub>3</sub>	3				
	b) 2 lines 250 pulses	0.1 x 12	Al(CH <sub>3</sub> ) <sub>3</sub>	1	H <sub>2</sub>	14	30	H <sub>2</sub> bomb and lines pumped out and flushed.
Batch 11: Untreated Quadrant								
10 or 20	3 lines 200 pulses	0.1 x 12	WF <sub>6</sub>	1.6			30	Chamber passivated with 4 Torr WF <sub>6</sub> and WF <sub>6</sub> lines pumped out and refilled twice.
20	3 lines 250 pulses	0.1 x 12	WF <sub>6</sub>	1.6	H <sub>2</sub>	32	30	
Batch 12: a) Untreated Quadrant; b) R64 Treated Quadrant								
10	a) 8 lines 250 pulses	0.1 x 12	Al(CH <sub>3</sub> ) <sub>3</sub>	0.3 - 4			30	Constant flow of Al(CH <sub>3</sub> ) <sub>3</sub>
10	b) 27 lines 250 pulses	0.1 x 12	Al(CH <sub>3</sub> ) <sub>3</sub>	0.3			30	Last 17 lines made with cylinder lens rotated 90° so lines are ⊥ to first 9.
Batch 15: 2 Untreated Quadrants								
0.5-4	a) 11 lines 1000 pulses	0.1 x 12	Al(CH <sub>3</sub> ) <sub>3</sub>	0.3			30	Laser beam apertured to give better defined line focus. Flowing gas.
	b) 8 lines 500 & 1000 pulses	0.1 x 12	WF <sub>6</sub>	0.7 - 3	H <sub>2</sub>	3 - 16	30	

Table 3-4  
Fine Line Metallization by Laser Sintering and Photodecomposition

LASER ENERGY (mJ)	NUMBER OF PULSES & LINES	IMAGE SIZE (mm)	GAS	PRESSURE (Torr)	TEMP. (°C)	LASER PULSE DURATION (nsec)	REMARKS
Batch 13: Si Wafer Plated with Ti/Pd/Ag							
10 or 20	10 lines 1, 10, 50 pulses	0.1 x 12 0.2 x 12	Air	760	20	30	Try to sinter plated metal to bond to Si wafer. Visible marks made on metal surface.
Batch 14: Si Wafer Plated with Ti/Pd/Ag							
10 or 20	20 lines 1, 10, 50 shots	0.1 x 12 0.2 x 12	Air	760	20	30	Improved laser mirror alignment
Batch 16: Two Si Wafers Coated with Silver Neodecanoate							
2 - 7	a) 19 lines 1, 10, 50, 100, 250 pulses	0.1 x 12	Air	760	20	30	Laser beam apertured to give sharper focus. Curls of dust formed in chamber from decomposition of silver neodecanoate. Reflectivity decreases after ~5 shots. Gold lines visible on surface after processing.
2 - 9	b) 21 lines 1, 10, 50, 100, 200 pulses	0.1 x 12	Air	760	20	30	
Batch 17: Two Si Wafers Coated with Silver Neodecanoate							
2	a) 49 lines 250 pulses	0.1 x 12	Air	760	65	30	Two grids consisting of 20 lines spaced 0.020" and a buss bar at 90° touching all the lines.
0.2	b) 50 lines 10, 20 pulses	0.1 x 12	Air	760	65	30	Flowing Air
Batch 19: Si Wafer Coated with Silver Neodecanoate							
1	18 lines 100, 250 pulses	0.1 x 12	Air	760	20°C 70°C	30	Four grids of 8 lines spaced 1 mm with 1 buss bar contacting all lines.

Table 3-4 (Continued)  
Fine Line Metallization by Laser Sintering and Photodecomposition

LASER ENERGY (mJ)	NUMBER OF PULSES & LINES	IMAGE SIZE (mm)	GAS	PRESSURE (Torr)	TEMP. (°C)	LASER PULSE DURATION (nsec)	REMARKS
Batch 21: Si Wafer Coated with Silver Neodecanoate							
1	45 lines 100, 250 pulses	0.1 x 12	Air	760	70	30	Four grids of 10 lines with 1 cross bars contacting all 10 lines.

Table 3-5

Laser Photodeposition of SiO<sub>2</sub>

LASER ENERGY (mJ)	NUMBER OF PULSES & LINES	IMAGE SIZE (mm)	DONOR GASES	FLOW RATE RATIO	PRESSURE (Torr)	TEMP (C)	PULSE DURATION (nsec)	REMARKS
Batch 18: Untreated Si Quadrant								
5	5 spots 1000, 2000 pulses	5 x 12	N <sub>2</sub> O/SiH <sub>4</sub>	5/1	10, 20	190	30	Spots were visible after processing.
Batch 19A: Untreated Si Quadrant								
5	14 spots 1000, 2000 pulses	5 x 12	N <sub>2</sub> O/SiH <sub>4</sub>	5/1	10	200	30	
Batch 22: Si Solar Cell (2 x 2 cm)								
12	45 spots 500 pulses	5 x 12	N <sub>2</sub> O/SiH <sub>4</sub>	5/1	10	190	30	Cell completely covered with 50% overlapping spots.
Batch 23: Four Si Solar Cells (2 x 2 cm)								
12	49 spots 500 pulses	5 x 12	N <sub>2</sub> O/SiH <sub>4</sub>	5/1	10	90	30	
Batch 24: Three Si Solar Cells (2 x 2 cm)								
12	a) 45 spots 1000 pulses	5 x 12	N <sub>2</sub> O/SiH <sub>4</sub>	5/1	10	180	30	
12	b) 240 spots 100 pulses	0.2 x 12	N <sub>2</sub> O/SiH <sub>4</sub>	5/1	10	180	30	
12	c) 240 spots	0.2 x 12	N <sub>2</sub> O/SiH <sub>4</sub>	5/1	10	180	30	

## SECTION 4.0

### SOLAR CELL EXPERIMENTAL INVESTIGATIONS

Several major areas were to be investigated: junction formation, surface passivation, and metallization. Each area had many variables of its own to be determined for optimum cell performance. Remarks regarding batch size and number of cells per wafer are found in Section 3.5.1.4.

#### 4.1 JUNCTION FORMATION

Starting parameters to be determined included surface condition, dopant source and methodology, laser energy density, and laser beam overlap percentage. Some of the parameters are related and inseparable experimentally.

##### 4.1.1 Liquid Dopant and Surface Morphology

A spin-on liquid dopant source was used in an effort to achieve a shallow junction in order to improve the short wavelength response. Both p-type (boron glass) and n-type (phosphorus glass) were applied on n- and p-type substrates, respectively. It was found immediately that p-type boron glass required a high laser energy density ( $>2 \text{ J/cm}^2$ ) because of its slower diffusivity in silicon, but this badly damaged the surface, causing poor fill factor and low  $V_{oc}$ .

The annealing experiment was then continued with only a phosphorus spin-on dopant source on p-type Cz wafers of 0.7 ohm-cm base resistivity. Surface preparation included texturization and chemical polishing. The threshold laser energy was found to be different for the two due to differences in surface reflectivity, as expected. The use of the textured surface was an effort to achieve lower required annealing energy density and better AR effects due to the pyramidization.

##### 4.1.1.1 Textured Surface

Energy density as low as  $0.4 \text{ J/cm}^2$  (70% overlap) was found sufficient to melt the texturized surface. However, the cells were almost all badly shunted (Table 4-1a). A companion wafer (2x4 in.) that had been laser annealed at the same settings went through an additional furnace heat treatment at  $650^\circ\text{C}$  for 30 minutes before metallization. The cell efficiency improved to 11.7% (Table 4-1b). Such a low temperature heat treatment is believed to provide stress relief of the melt-recrystallized surface. Cell performance of a cell prepared with  $0.7 \text{ J/cm}^2$  annealing with 50% overlap showed further improvement. Highest cell efficiency was about 11.6% before AR coating (Table 4-1c). Heat treatment of the  $0.7 \text{ J/cm}^2$  annealed wafer did not show obvious improvement. A possible explanation could be that  $0.7 \text{ J/cm}^2$  was sufficient to cause more complete surface regrowth

with less relievable stress. In fact, SEM photographs of these two samples indicated much more surface melting with  $0.7 \text{ J/cm}^2$  than with  $0.4 \text{ J/cm}^2$  (Fig. 4-1).

**Table 4-1.** Textured Cz p-type wafer with spin-on source, laser annealed.

a. At  $0.4 \text{ J/cm}^2$  with 70% overlap.

Cell ID	V <sub>oc</sub> (V)	J <sub>sc</sub> (mA/cm <sup>2</sup> )	FF (%)	Eff (%)
B5B 1	0.429	28.32	59.60	7.24
2	0.406	28.26	57.30	6.56
3	0.399	28.24	55.40	6.25
4	0.434	27.89	57.60	6.97

b. At  $0.4 \text{ J/cm}^2$  with 70% overlap followed by furnace heat treatment at  $650^\circ\text{C}$  for 30 minutes.

Cell ID	V <sub>oc</sub> (V)	J <sub>sc</sub> (mA/cm <sup>2</sup> )	FF (%)	Eff (%)
B5BT 1	0.555	28.95	69.50	11.18
2	0.560	29.04	67.40	10.96
3	0.563	28.54	69.10	11.10
4	0.560	28.90	68.90	11.15
5	0.573	28.66	71.40	11.73
6	0.544	29.08	65.00	10.27

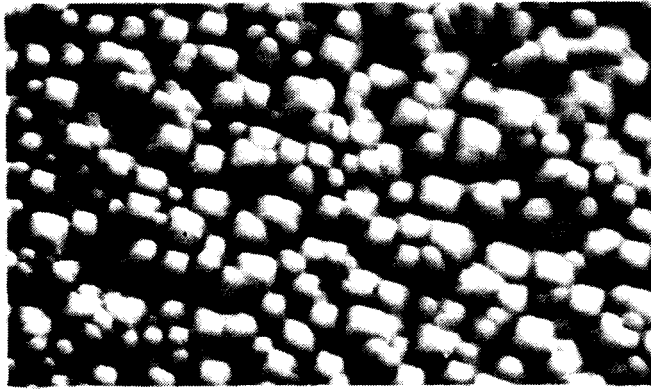
c. At  $0.7 \text{ J/cm}^2$  with 50% overlap.

Cell ID	V <sub>oc</sub> (V)	J <sub>sc</sub> (mA/cm <sup>2</sup> )	FF (%)	Eff (%)
B5A 1	0.534	29.94	69.30	11.08
2	0.536	29.56	68.60	10.87
3	- - -	Dead Cell	- - -	- - -
4	0.459	26.34	63.00	7.74
5	- - -	Dead Cell	- - -	- - -
6	0.549	30.43	69.66	11.64

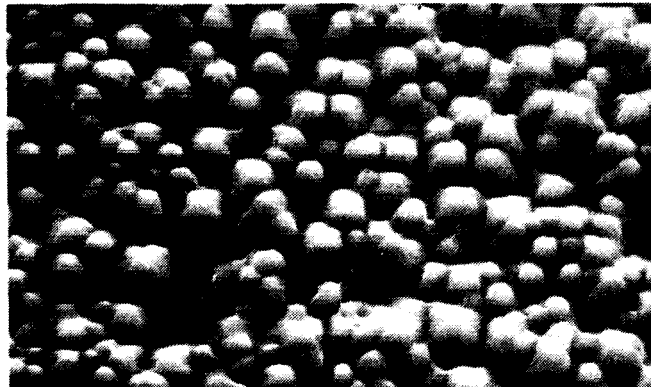
High energy density, e.g. at  $1.2 \text{ J/cm}^2$ , yielded lower cell efficiency ( $\sim 8.7\%$ ) due to severe reduction in  $J_{sc}$  ( $21 \text{ mA/cm}^2$ ) because of loss in texturing. SEM photos (Fig. 4-1c) also revealed that heavy melting-resolidification took place after high energy density annealing. The effective energy density at the surface was increased by approximately 40% due to the second reflection from the textured surface.



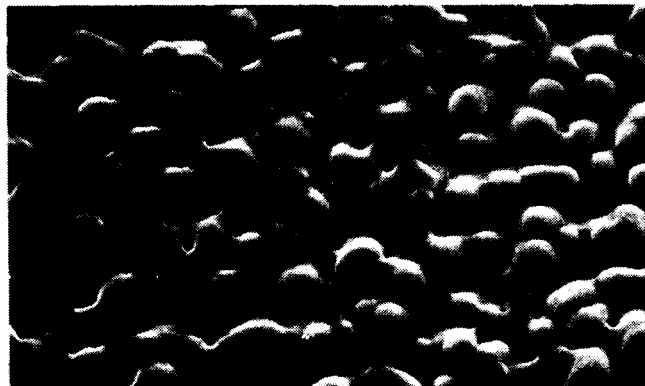
ORIGINAL PAGE IS  
OF POOR QUALITY



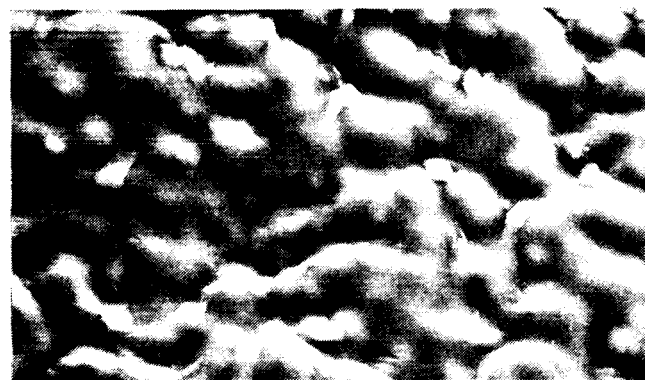
(a)



(b)



(c)



(d)

Fig. 4-1. 500x SEM photos of textured wafers with spin-on liquid dopant after laser annealing at (a)  $0.4 \text{ J/cm}^2$ , (b)  $0.7 \text{ J/cm}^2$ , (c)  $1.2 \text{ J/cm}^2$ , and (d)  $2.5 \text{ J/cm}^2$ .

#### 4.1.1.2 Chemically Polished Surface

In parallel with the textured wafer experiment, 20% NaOH etched wafers (Cz 0.7 ohm-cm p-type base) were used which had spin-on liquid dopant followed by laser annealing at energy densities of 0.9 J/cm<sup>2</sup>, 1.2 J/cm<sup>2</sup>, and 1.6 J/cm<sup>2</sup> with 50% overlap. Results are summarized in Table 4-2. The data represent the average cell efficiency weighted over four samples in each case. Also included are the results of post furnace annealing at 650°C for 30 minutes to test for a stress relief effect.

**Table 4-2.** Cells fabricated from polished Cz p-type wafer with spin-on source laser annealed at energies 0.9, 1.2, and 1.6 J/cm<sup>2</sup>.

Cell ID	Control				650°C Furnace Annealed			
	V <sub>oc</sub> (V)	J <sub>sc</sub> (mA/cm <sup>2</sup> )	FF (%)	Eff (%)	V <sub>oc</sub> (V)	J <sub>sc</sub> (mA/cm <sup>2</sup> )	FF (%)	Eff (%)
B7-I annealed at 1.2 J/cm <sup>2</sup> (1F)	0.586	20.65	75.3	9.1	0.587	19.90	76.0	8.9
B7-III annealed at 0.9 J/cm <sup>2</sup> (2F)	0.582	21.15	68.8	8.5	0.589	20.54	73.0	8.8
B7-II annealed at 1.6 J/cm <sup>2</sup> (3F)	0.588	19.40	75.9	8.6	0.587	18.60	79.7	8.5

As indicated by the data, the shallow junction formed by annealing at 0.9 J/cm<sup>2</sup> (1F) on these reflective surface wafers improved the J<sub>sc</sub> in comparison with other groups.

However, the fill factor was lowered as a result of increased series resistance. Deeper junctions of groups 1F and 3F had much better fill factor yet lower J<sub>sc</sub>, confirming the statement above.

Furnace annealing at 650°C for 30 minutes (before metallization) improved the fill factor slightly, especially on group 2F (0.9 J/cm<sup>2</sup>), but degraded the J<sub>sc</sub> by approximately 3-4%. The results suggest that thermal stress relief appears effective only for low laser energy density annealed surfaces, which is similar to the observation for the textured surface.

For control purposes, caustic etched wafers with a doping layer from liquid dopant were subjected to thermal diffusion at 820°C for 1.5 hours. Results are summarized in Table 4-3.

Cell efficiency of the thermally diffused wafers on average was better than those laser annealed due to higher J<sub>sc</sub>, suggesting that the junction depth of thermally diffused cells with spin-on dopant was even shallower with less absorption in the emitter

(Fig. 4-2). The lower  $V_{oc}$  was probably due to high recombination in the junction as indicated by the dark I-V. In fact, all cells with emitters diffused both thermally or laser assisted with liquid dopant had high dark recombination current. One of the possible sources of recombination centers could be from the liquid dopant. The usage of liquid dopant was then halted.

**Table 4-3.** Cell performance of thermally diffused caustic polished Cz wafer with spin-on source as dopant.

Cell ID	$V_{oc}$ (V)	$J_{sc}$ (mA/cm <sup>2</sup> )	FF (%)	Eff (%)
B5-C 1	0.531	22.87	64.4	7.8
2	0.563	23.33	71.1	9.3
3	0.559	23.43	71.8	9.4
4	0.585	22.43	60.2	7.9
5	0.540	23.00	71.4	8.9

#### **4.1.2 Ion Implanted Emitter and Laser Uniformity**

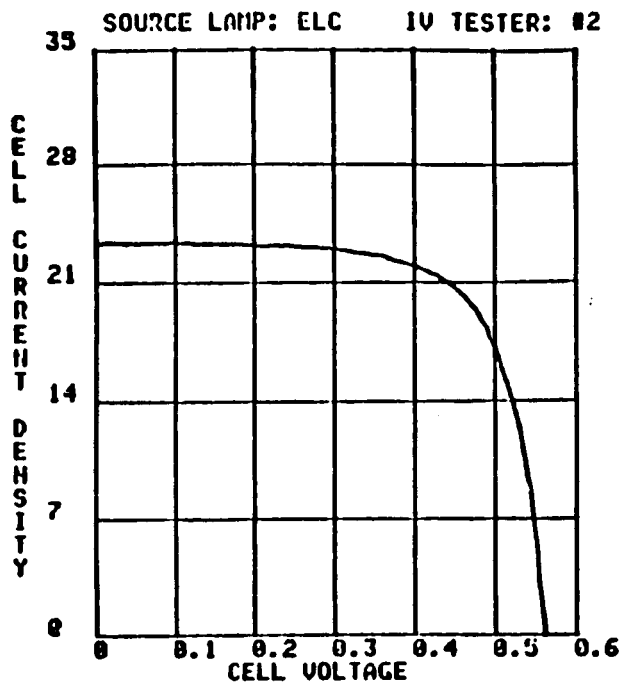
##### **4.1.2.1 Conventional Mass Analyzed $31p^+$ Ion Implant**

In the early stage of the program, ion implants were processed for 4-in. diameter p-type caustic polished Cz ( $\sim 0.33$  ohm-cm) wafers at 10 keV with dosage of  $5 \times 10^{15}$  atoms/cm<sup>2</sup> and  $1 \times 10^{15}$  atoms/cm<sup>2</sup> respectively. Laser energy density (EXC-1, the small laser) was set at 0.4 J/cm<sup>2</sup> and 0.7 J/cm<sup>2</sup>, respectively, with pulse duration 4-6 ns. Cell characterization indicated low  $J_{sc}$ ,  $V_{oc}$ , and fill factor as the result of insufficient implant damage removal by such low laser energy densities. Typical results are listed in Table 4-4.

On L5A #7, the extremely low  $V_{oc}$  was due to insufficient surface concentration ( $1 \times 10^{15}$  atoms/cm<sup>2</sup>), which also affected the sheet rho uniformity across the surface and caused leakage as revealed by reverse dark I-V measurement.

The poor result with caustic polished Cz wafers suggested the use of chem-mechanically polished 0.3 ohm-cm p-type FZ wafers as a baseline experiment. The material had been well characterized by conventional thermal diffusion that yielded 16% efficiency at AM1.5 with simple spin-on AR coating for cells with 25 cm<sup>2</sup> total area.

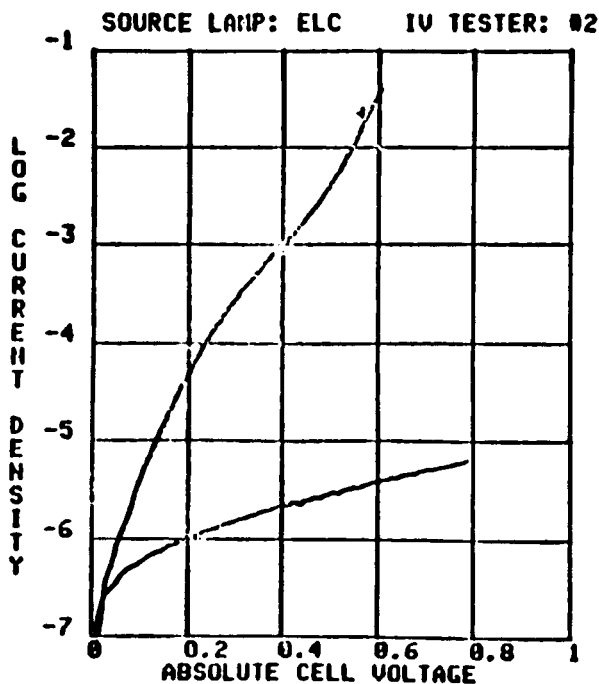
Material from this batch was sent for ion implantation with  $31p^+$  at 5 keV of dosage  $1 \times 10^{15}$ ,  $2.5 \times 10^{15}$ , and  $5 \times 10^{15}$  atoms/cm<sup>2</sup>, respectively. Laser energy varied from 0.90 to 1.30 J/cm<sup>2</sup>, with overlap from 20% to 70%. Pulse duration time was extended from 6 nsec to 50 nsec (double pulse shape). The reason for overlap was to compensate beam nonuniformity as already mentioned. As beam quality was progressively improving, the overlap factor was decreasing proportionally. Results are summarized in Table 4-5.



SINGLE/POLY  
 LIGHT IV AT 25C  
 OPERATOR: DW  
 CELL: L5 CONTR. (1)  
 Date/time: 15-JUN-84 16:55:40  
 AREA: 4.00 (sq.cm)  
 Isc: 0.093 (amps)  
 Jsc: 23.33 (ma/sq)  
 Voc: 0.563 (volts)  
 Ipn: 0.082 (amps)  
 Jpn: 20.46 (ma/sq)  
 Vpn: 0.456 (volts)  
 Pn: 0.037 (watts)  
 Cff: 71.08 %  
 Eff: 9.33 %

(a)

SPIN ON SOURCE CAUTIC POLISHED  
 SINTERED  
 THERMAL ANNEALED @ 820 C X 1.5 HOURS



SINGLE/POLY  
 DARK IV AT 25C  
 Date/time: 15-JUN-84 16:56:25  
 OPERATOR: DW  
 CELL: L5 CONTR. (2)  
 AREA: 4.00 (sq.cm)  
 Gsh: 2.76E-005 (mho)  
 $\pm$  3.48E-007  
 gsh: 6.89E-006 (mho/sq.cm)  
 Rsr: 1.65E-001 (ohm)  
 rsr: 6.58E-001 (ohm-sq.cm)

(b)

SPIN ON SOURCE CAUTIC POLISHED  
 SINTERED  
 THERMAL ANNEALED @ 820 C X 1.5 HOURS

Fig. 4-2. Light and dark I-V curves of a thermally diffused n+ cell with spin-on liquid source on a p-type substrate.

**Table 4-4.** Results of laser annealing caustic polished Cz wafer with 10 keV ion implant dosage at  $5 \times 10^{15}$  and  $1 \times 10^{15}$  atoms/cm<sup>2</sup>.

Cell ID	Laser Energy Density (J/cm <sup>2</sup> )	Over-lap (%)	V <sub>OC</sub> (V)	J <sub>SC</sub> (mA/cm <sup>2</sup> )	FF (%)	Eff (%)	Sheet Rho (ohms/sq)
10 keV at $5 \times 10^{15}$ atoms/cm <sup>2</sup>							
B5A #5	0.7	50	0.581	18.7	67.0	7.3	33
B5B #4	0.4	70	0.516	18.7	64.9	6.3	31
10 keV at $1 \times 10^{15}$ atoms/cm <sup>2</sup>							
L5A #7	0.7	50	0.389	20.4	52.1	4.2	90
L5B #4	0.4	70	0.479	19.8	68.3	6.5	87

In experiment B9-1 where laser energy density was as high as 1.3 J/cm<sup>2</sup> with 70% overlap, both current density and V<sub>OC</sub> were very low. The latter was probably due to excessive surface damage, especially at the center of overlap (Fig. 4-3), indicating the laser is highly nonuniform spatially. All cells annealed at 0.9 J/cm<sup>2</sup> (B9-2) had high leakage current and low shunt resistance because of incomplete ion damage removal at such low energy density. However, the high current density obtained suggested that 5 keV with 1 to  $2.5 \times 10^{15}$  atoms/cm<sup>2</sup> ion implant provided sufficient surface concentration for a reasonable internal electric field for good current collection.

At a late stage of the program, there were experiments to study effects of damage by 5 keV implant and alternate implant methods.

**Table 4-5.** Results of laser annealing on chem-mech polished FZ wafers; 5 keV ion implanted with  $1 \times 10^{15}$  and  $2.5 \times 10^{15}$  atoms/cm<sup>2</sup> dosage, respectively.

a. 5 keV ion dosage at  $2.5 \times 10^{15}$  atoms/cm<sup>2</sup>, laser energy density 1.30 J/cm<sup>2</sup>, 70% overlap.

Cell ID	V <sub>OC</sub> (V)	J <sub>SC</sub> (mA/cm <sup>2</sup> )	FF (%)	Eff (%)	Sheet Rho (ohms/sq)
B9-1					
#1	0.554	18.23	75.00	7.58	40-45
#2	0.552	18.22	75.70	7.62	40-45
#3	0.555	16.61	73.00	6.79	40-45
#4	0.544	17.74	67.22	6.48	40-45
#5	0.543	18.33	71.72	7.14	40-45

b. 5 keV ion dosage at  $2.5 \times 10^{15}$  atoms/cm<sup>2</sup>, laser energy density 0.90 J/cm<sup>2</sup>, 70% overlap.

Cell ID	V <sub>oc</sub> (V)	J <sub>sc</sub> (mA/cm <sup>2</sup> )	FF (%)	Eff (%)	Sheet Rho (ohms/sq)
B9-2					
#1	0.579	21.36	48.13	5.96	50-55
#2	0.583	21.13	55.92	6.89	50-55
#3	0.531	21.17	60.21	6.77	50-55
#4	0.593	21.12	67.20	8.42	50-55

c. 5 keV ion dosage at  $1 \times 10^{15}$  atoms/cm<sup>2</sup>, laser energy density 0.90 J/cm<sup>2</sup>, 30% overlap.

Cell ID	V <sub>oc</sub> (V)	J <sub>sc</sub> (mA/cm <sup>2</sup> )	FF (%)	Eff (%)	Sheet Rho (ohms/sq)
B10-1					
#1	0.534	21.74	70.24	7.70	65-74
#2	0.548	22.64	70.74	8.78	65-74
#3	0.553	22.58	72.17	9.01	65-74
#4	0.552	22.36	68.97	8.51	65-74

d. 5 keV ion dosage at  $1 \times 10^{15}$  atoms/cm<sup>2</sup>, laser energy density 1.25 J/cm<sup>2</sup>, 20% overlap.

Cell ID	V <sub>oc</sub> (V)	J <sub>sc</sub> (mA/cm <sup>2</sup> )	FF (%)	Eff (%)	Sheet Rho (ohms/sq)
B10-2					
#2	0.569	21.77	70.68	8.75	60-75
#3	0.577	21.95	71.32	9.03	60-75
#4	0.572	21.96	70.67	8.87	60-75
#5	0.573	21.59	72.12	8.92	60-75

#### 4.1.2.2 Effects of Damage by 5 keV Ion Implant

To investigate performance effects from lattice damage caused by 5 keV ion implantation, two key experiments (Batch 35 and Batch 36) were performed in which thermal n<sup>+</sup> deposition was used instead of ion implant. A thermal deposition of dopant source represents a zero lattice damage case in comparison to any ion implant source.

In Batch 35, laser energies of 1.6 J/cm<sup>2</sup> with 50% overlap were used. The four comparison process sequences are shown in Fig. 4-4. Average performances of the four groups of cells (made from a 3" FZ wafer for ion implant Case A, and a 4" Cz wafer for thermal deposition Cases B, C, and D) are given in Table 4-6.

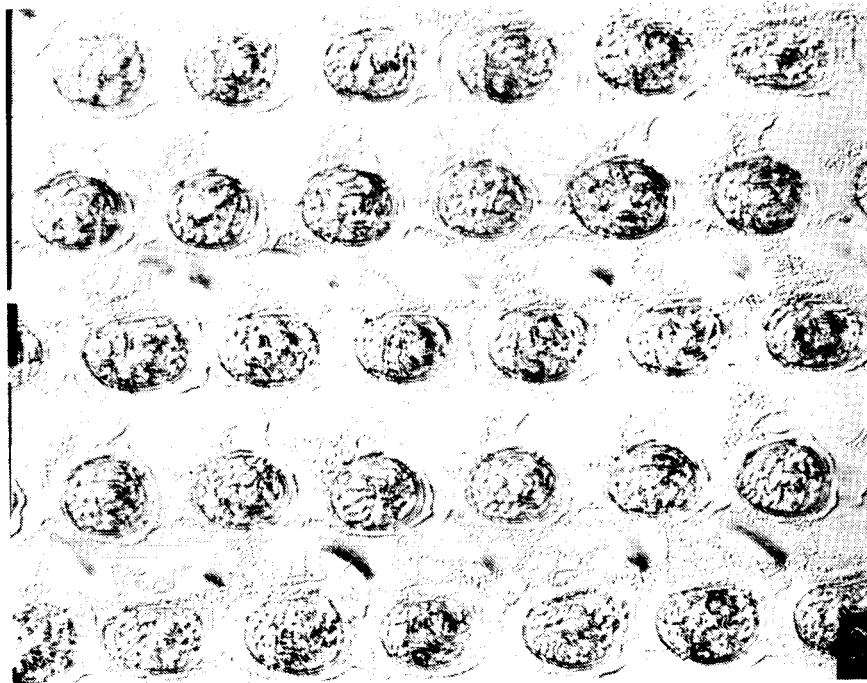


Fig. 4-3. Laser annealing on 5 keV,  $2 \times 10^{15}$  atoms/cm<sup>2</sup> ion implanted surfaces at 1.3 J/cm<sup>2</sup>, with 70% overlap pulse duration estimated at 6 nsec (B-9).

The low sheet rho for Case C (laser annealed cells with phosphorus glass) is consistent with results from Batch 15 in that the glass layer acted as a high concentration doping source. Spreading resistance measurements on these cells (Fig. 4-5) suggested that the various junction depths correlate well with the differences in  $J_{sc}$  among these cells and that shallow junctions gave rise to higher current collection.

The results of the  $V_{oc}$  measurements, however, are rather interesting. Case C (Cz, n+ thermal deposition followed by laser annealing) had the highest  $V_{oc}$ , about 8 mV higher than Case A (FZ, low bulk resistivity, ion implanted, laser annealed). The difference in  $V_{oc}$  between the two is believed to be due to residual lattice damage by ion implantation.

The second experiment, Batch 36, used the same ion implanted FZ material as Batch 35 except that the laser annealing energy was reduced to 1.33 J/cm<sup>2</sup>. Control cells to monitor wafer cleaning and metallization were thermally diffused Cz cells. Results showed that both the  $V_{oc}$  and fill factor of ion implanted cells decreased in comparison with Batch 35, while the control cells behaved typically for 1 ohm-cm Cz material without BSF. These results indicate that reducing the annealing energy increases the amount of non-removable lattice damage induced by 5 keV ion implantation.

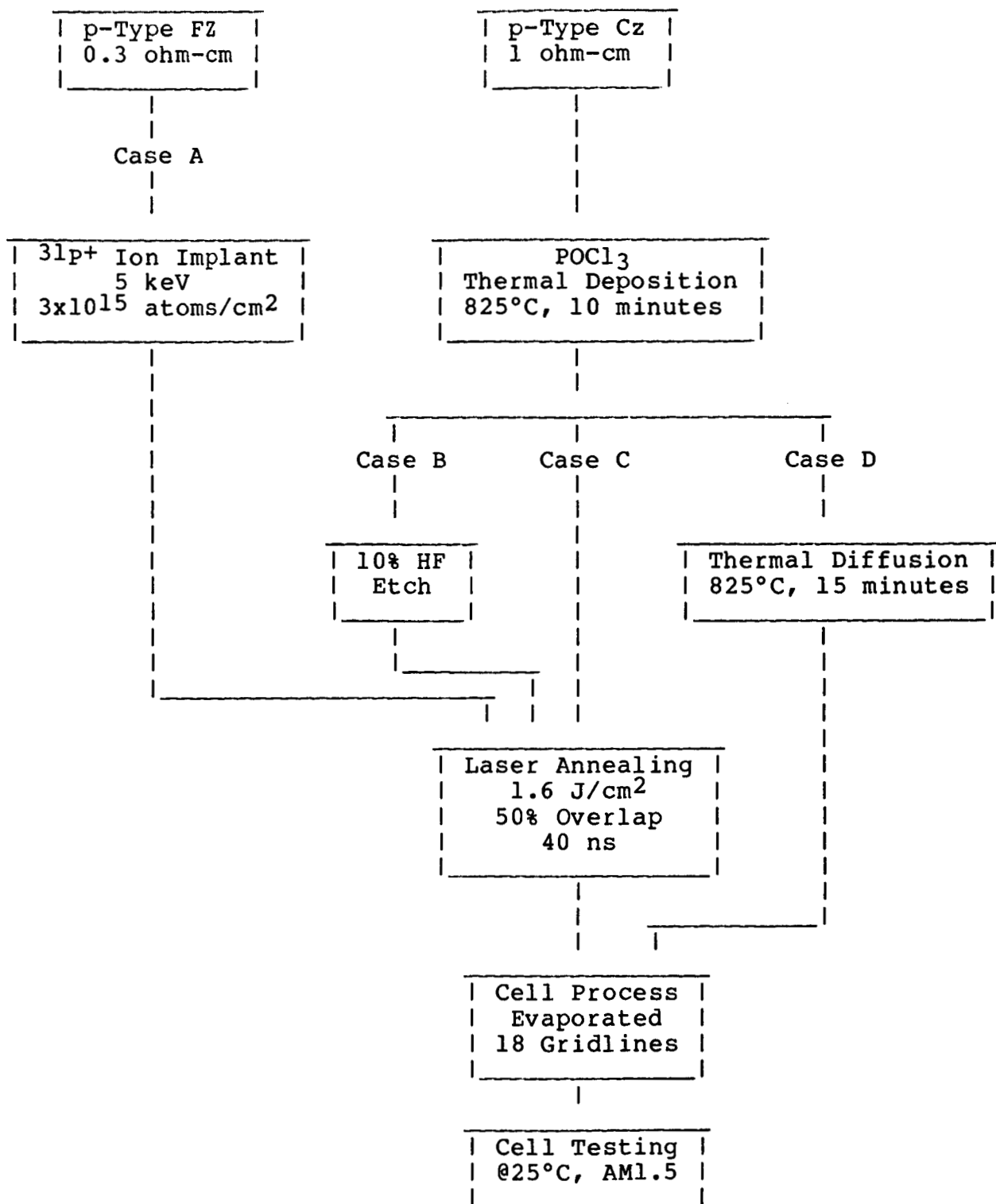


Fig. 4-4. Process sequence for Batch 35.

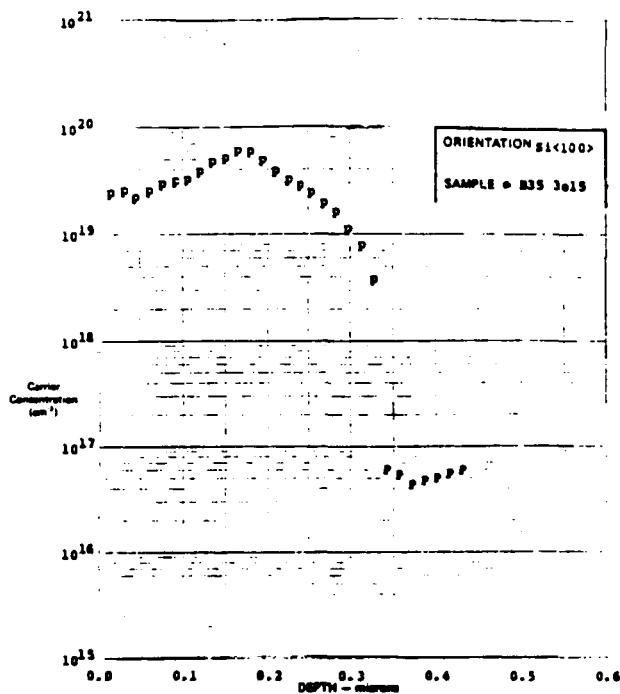


**Table 4-6.** Average performance of Batch 35 cells. Laser energy density at  $1.6 \text{ J/cm}^2$ , 50% overlap with 40 ns pulse duration.

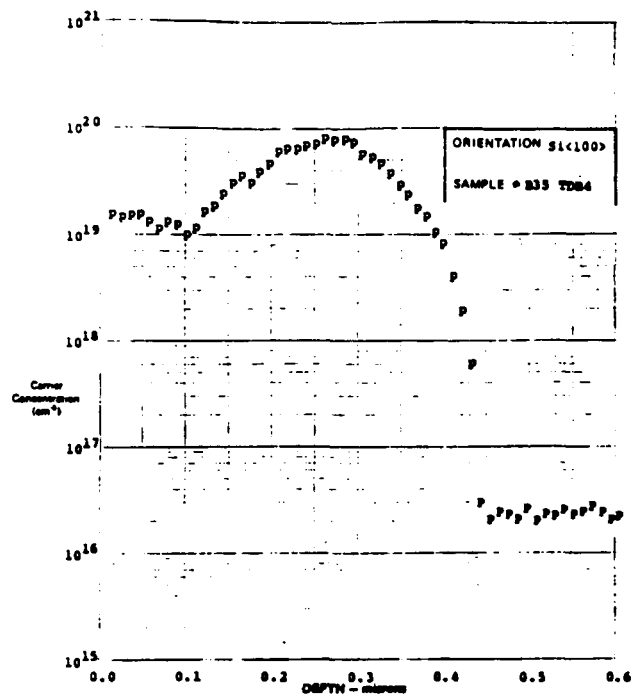
Sample	$J_{sc}$ (mA/cm <sup>2</sup> )	$V_{oc}$ (%)	FF (%)	Eff (%)	Sheet Rho (ohm/sq)	Junction Depth (micron)
Case A FZ, 0.3 ohm-cm, 5 keV, 31p+ ion implant $3 \times 10^{15}$ atoms/cm <sup>2</sup>	21.02	0.588	75.10	9.28	85	0.35
Case B Cz, 1 ohm-cm, thermal POCl <sub>3</sub> deposition + HF + laser annealing	19.20	0.587	73.80	8.3	65	0.45
Case C Cz, 1 ohm-cm, thermal POCl <sub>3</sub> deposition + laser annealing	19.80	0.596	75.44	8.9	23	0.49
Case D Cz, 1 ohm-cm, thermal POCl <sub>3</sub> deposition + thermal diffusion	21.38	0.590	74.24	9.3	140-150	0.27

#### 4.1.2.3 Effects of "Neutrals" on Mass Analyzed Ion Implantation

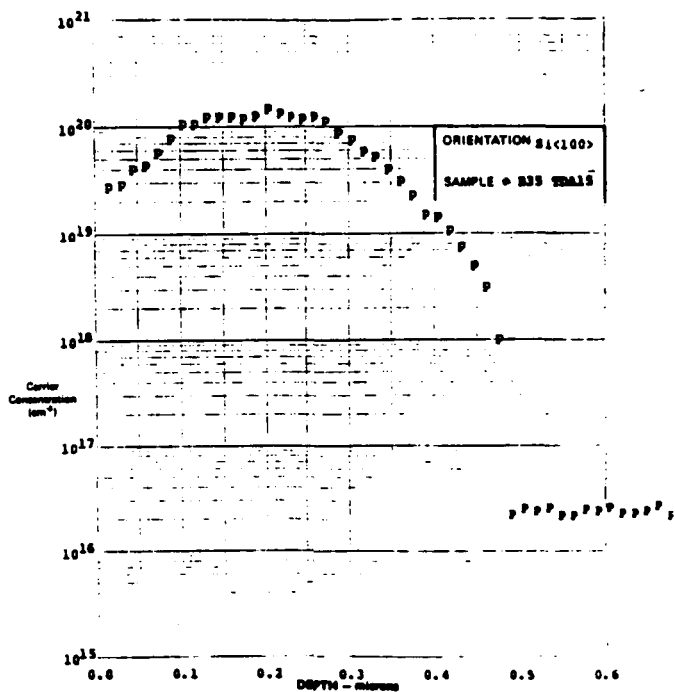
The best cell obtained so far in the project had been from Batch 26, in which 31p+ ion was implanted onto 2"x2" Cz material at 5 keV with fluence  $2.5 \times 10^{15}$  atoms/cm<sup>2</sup>. The ion implanted material was used through experiments B24, B26, and B28. In all three experiments, the average cell efficiency was above 9.5%, which was comparable to thermally diffused Cz cells. At the same time, the 5 keV,  $5 \times 10^{15}$  atoms/cm<sup>2</sup> ion implanted 3" (diameter) FZ material was about 8.5-9% in efficiency overall. Discussion with the implant vendor indicated that the Cz material was implanted with the presence of "neutral" traps while the FZ was not. The "neutrals" came from ionized phosphorus atoms accelerated to 35 keV which were electrically neutralized at the walls before reaching the decelerating field. Such neutrals would continue to travel with 35 keV impact kinetic energy unaffected by the reversing 30 kV potential. The penetration depth by such high energy atoms would be more than 0.4 micron. This is a potential explanation for poorer fill factor.



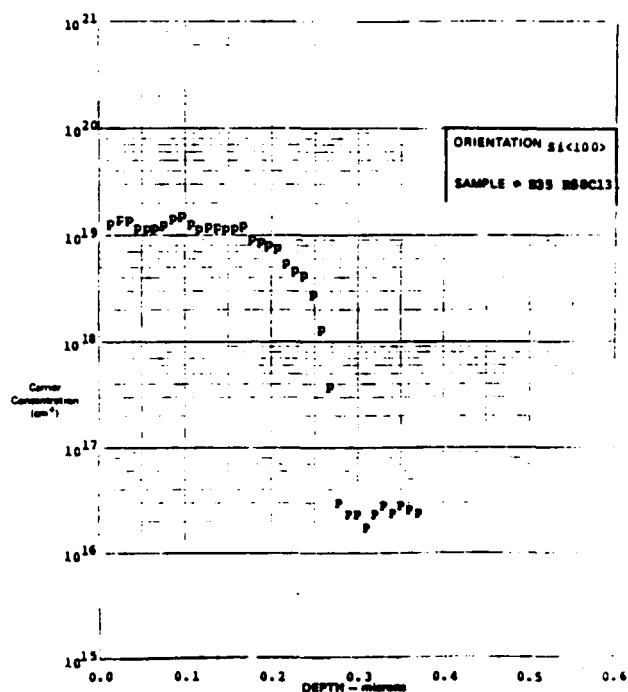
Case A. FZ; ion implant  
+ laser anneal



Case B. Cz; thermal deposition  
+ HF + laser anneal



Case C. Cz; thermal deposition  
+ laser anneal



Case D. Cz; thermal deposition  
+ thermal diffusion

Fig. 4-5. Depth profiles of Batch 35 cells.

ORIGINAL PAGE IS  
OF POOR QUALITY

Their effect on  $V_{oc}$  can be realized by considering the following junction equation:

$$V_{oc} \cong \frac{kT}{e} \ln \frac{J_L}{J_{o1} + J_{o2}}$$

where

$J_L \sim J_{sc}$  = short circuit current density

$$J_{o1} \propto \sqrt{D/T} / N_A$$

$$J_{o2} \propto \frac{U}{N_B}$$

$N_B$  = bulk dopant concentration

$$\frac{kT}{e} = 0.0254 \text{ V at } T = 300^\circ\text{K}$$

$U$  = recombination rate

An increase in  $U$  will obviously decrease the  $V_{oc}$  as experimentally observed in ion implanted samples compared with non-ion implanted ones. In practice, neutrals can be mitigated by the presence of a deflecting field during implant.

#### 4.1.2.4 Non-Mass Analyzed Molecular Ion Implantation

Besides using the conventional mass-separated atomic ion implantation for emitter formation, a molecular ion implant process was also attempted. The vendor subjected samples of 4" square, 1 ohm-cm p-type Cz material to  $PF_3^+$  ion implantation at the calculated energy

$$\text{dopant keV} = \frac{\text{dopant atomic wt}}{\text{molecular wt}} \times \text{electrode potential}$$

e.g.,

$$\begin{aligned} \text{boron atom energy} &= \frac{\text{boron atomic wt}}{\text{BF}_2 \text{ molecular wt}} \times \text{beam energy} \\ &= \frac{11}{49} \times 22 \text{ keV} \sim 5 \text{ keV} \end{aligned}$$

This analysis is true only if the  $BF_2$  molecule dissociates into atoms at the surface. Otherwise, the impact energy would be 22 keV, the effect of which is uncertain. Molecular ion implant

(PF<sub>3</sub>), on the other hand, could be promising due to the heavier atomic weight of phosphorus. The detrimental effect of the nondissociated molecule would not be as much as in BF<sub>2</sub>.

In the actual experiment, 4" square p-type Cz wafers were subjected to the calculated PF<sub>3</sub><sup>+</sup> molecular ion implant with fluence 3x10<sup>15</sup> atoms/cm<sup>2</sup>. Wafers were then annealed at energy 1.4 J/cm<sup>2</sup>, 50% overlap. Sheet rho was about 110 ohms/sq, which is high for the estimated 3x10<sup>15</sup> atomic implant. It is possible that a large portion of the molecular ion bounced off the surface instead of penetrating into the substrate. Cell testing indicated (Table 4-7) the majority are above 9% in efficiency with three at or above 9.4%, a substantially better performance than previous experiments. Better results could have been obtained by fine tuning the new parameters such as beam energy and beam fluence.

**Table 4-7.** Cz p-type material subjected to molecular ion implant. Laser energy density ~1.47 J/cm<sup>2</sup>, 50% overlap, 110 sheet rho.

Sample No.	J <sub>sc</sub> (mA/cm <sup>2</sup> )	V <sub>oc</sub> (V)	FF (%)	Eff (%)
B46				
#1	20.66	0.574	72.30	8.58
#2	21.13	0.579	77.48	9.48
#3	20.16	0.575	75.78	8.79
#4	20.17	0.577	76.30	8.87
#5	20.50	0.577	76.00	9.00
#6	20.87	0.578	78.2	9.44
#7	20.74	0.577	75.74	9.07
#8	20.97	0.58	80.00	9.71
Average	20.65	0.577	76.48	9.11

#### 4.1.2.5 <sup>62</sup>P<sub>2</sub><sup>+</sup> Ion Implantation

Lattice damage due to energetic ion implant was further studied by tuning mass spectrum for <sup>62</sup>P<sub>2</sub><sup>+</sup> species at 5 keV instead of <sup>31</sup>P<sub>1</sub><sup>+</sup> ion species. At the moment of impact, the molecule would dissociate into <sup>31</sup>P<sub>1</sub><sup>+</sup> atoms each with 2.5 keV. From the kinetic energy equation, the impact momentum of the individual atoms (after dissociation) is calculated from:

$$5 \text{ keV} = 1/2 mV_0^2 + 1/2 mV_0^2 = mV_0^2 \quad (\text{Eq 1})$$

where 5 keV is the initial molecular energy, m is the atomic mass, and V<sub>0</sub> the velocity of the particles before impact.

$$V_0 = \sqrt{5 \text{ keV/m}} \quad (\text{Eq 2})$$

Hence the atomic momentum of  $^{62}\text{P}_2^+$  at impact,  $W_m$ , is

$$W_m = mV_0 = m \sqrt{5 \text{ keV/m}} = \sqrt{5m \text{ keV}} \quad (\text{Eq 3})$$

The momentum of  $^{31}\text{P}_1^+$ , at 5 keV, on the other hand, is

$$W_A = m \sqrt{(5 \times 2/m) \text{ keV}} = \sqrt{10m \text{ keV}} \quad (\text{Eq 4})$$

The difference in impact momentum between  $^{62}\text{P}_2^+$  (Eq 3) and  $^{31}\text{P}_1^+$  (Eq 4) then is equal to

$$\Delta W\% = \frac{W_m - W_A}{W_m} \times 100\% = -29.3\% \quad (\text{Eq 5})$$

If lattice damage is linearly proportional to particle impact momentum, the  $^{62}\text{P}_2^+$  ion implant would decrease damage by 30% over the  $^{31}\text{P}_1^+$  implant. However, if the molecule does not dissociate at the impact, the molecular momentum could become:

$$W_m(^{62}\text{P}_2^+) = (2m) V_0 = 2 \sqrt{5m \text{ keV}} = 4.47 \sqrt{m \text{ keV}}$$

which, compared with  $^{31}\text{P}_1^+$  atomic momentum

$$W_m(^{31}\text{P}_1^+) = 3.16 \sqrt{m \text{ keV}}$$

is almost 42% more than  $^{31}\text{P}_1^+$  ion impacts.

The concept was first tested with FZ p-type material ion implanted with  $^{62}\text{P}_2^+$  at 5 keV with  $2 \times 10^{15}$  atoms/cm<sup>2</sup> fluence. Results are summarized in Table 4-8.

The difference in  $J_{sc}$  between the B51 (I) and B51 (II) groups was caused mainly by the smaller shadow factor in B51 (II). Both wafers exhibited signs of slightly contaminated junctions, which could relate to the hazy surface to be discussed later. Despite the low fill factor, the average  $V_{oc}$  was satisfactory for non AR-coated Si cells. The best cell, No. B51 (II) #3, achieved an efficiency of almost 10.8%, the highest obtained in this program.

The variation in fill factor is believed to be due to contamination in wafer handling and transportation. The  $V_{oc}$ , on the other hand, is due mainly to poor junction characteristics, as revealed by spreading resistance depth profiling (Fig. 4-6a). Compared with B51 (Fig. 4-6b) which had the 10.8% cell, the dopant distribution here is much broader and slower falling, giving rise to a weaker built-in electrical field. The reason for the difference in profile is not immediately known, since all were ion implanted similarly with  $^{62}\text{P}_2^+$  species at 5 keV, except B51 at  $2 \times 10^{15}$  atoms/cm<sup>2</sup>, while B54 and B58 received  $2.5 \times 10^{15}$ , a

25% increase in dosage. In comparison with the  $31P_1^+$  ion implanted junction, both profiles of the above are considered significantly broader (Fig. 4-6c).

**Table 4-8.** FZ material ion implanted with  $62P_2^+$  at 5 keV,  $2 \times 10^{15}$  atoms/cm<sup>2</sup>.

Sample No.	$J_{sc}$ (mA/cm <sup>2</sup> )	$V_{oc}$ (V)	FF (%)	Eff (%)	Sheet Rho (ohm/sq)	Metallization
B51 (I)						
#1	21.36	0.591	75.54	9.53	80	18-grid
#2	21.53	0.593	78.63	10.04	"	shadow
#3	21.59	0.588	73.46	9.33	"	mask
#4	21.66	0.594	78.64	10.11	"	
B51 (II)						
#1	22.86	0.603	77.14	10.64	"	18-grid
#2	23.06	0.599	75.26	10.39	"	lift-off
#3	22.84	0.604	78.10	10.77	"	
#4	-----	-----	Broken	-----	-----	

Experiments continued with Cz material (1 ohm-cm) of 2"x2" and were also ion implanted with  $62P_2^+$  species at 5 keV with fluence  $2.5 \times 10^{15}$  atoms/cm<sup>2</sup>. Note that the dosage was increased from the  $2 \times 10^{15}$  of the previous experiment (B51) on FZ material, which had produced the highest efficiency cell at 10.8%. The reason for increasing the dosage was to try to increase the surface concentration for higher  $V_{oc}$ . Two different laser energy densities were used: 1.53 J/cm<sup>2</sup> for Batch 54 and 1.43 J/cm<sup>2</sup> for Batch 55. Both were annealed with the double lens focusing system. The post-annealed surface exhibited a haze-like appearance due to microscopic defects (Fig. 4-7), a phenomenon observed on all wafers annealed by the double lens focusing (see Section 4.2.2.3 for details). Electrical measurements (Table 4-9) on cells of both Batch 54 and Batch 55 were not as good as expected. Although the  $J_{sc}$  is at the right level (except B54-#3 because of broad gridlines), the  $V_{oc}$  is almost 10 mV too low for 1 ohm-cm material, and the fill factor varied erratically from 69% to 78%.

## 4.2 LASER PARAMETERS

From the experimental results obtained above and the examination of literature and data, indications are that the laser imprint overlap is crucial for ideal junction formation. A high percent overlap by a highly nonuniform laser would produce severe surface damage (see Fig. 4-3 under Section 4.1.2). With poor Gaussian beam quality, a decrease of overlap from 70% to 20% appears to

ORIGINAL PAGE IS  
OF POOR QUALITY

yield a comparatively better cell. However, nonuniform surface annealing was found to be present in the cells processed.

To further investigate the effect of beam uniformity, a larger and more powerful excimer (spot size  $>0.7 \text{ cm}^2$ ) laser was used. Results would be applied to upgrade the smaller laser originally used in the above experiments.

#### 4.2.1 Large Laser ("Lucy")

This laser can deliver 4 J of energy at 308 nm and is known to be superior in uniformity by design.

Two initial experiments were conducted with encouraging results (Table 4-10).

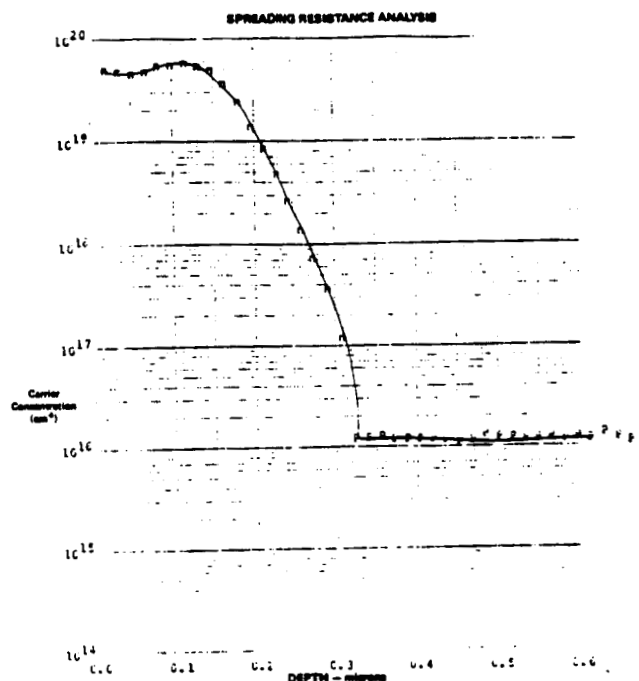


Fig. 4-6a. Spreading resistance depth profile. Cz sample (B55 W<sub>1</sub>), ion implanted at 5 keV with  $^{62}\text{P}_2^+$  molecular ion of fluence  $2 \times 10^{15} \text{ atoms/cm}^2$ .

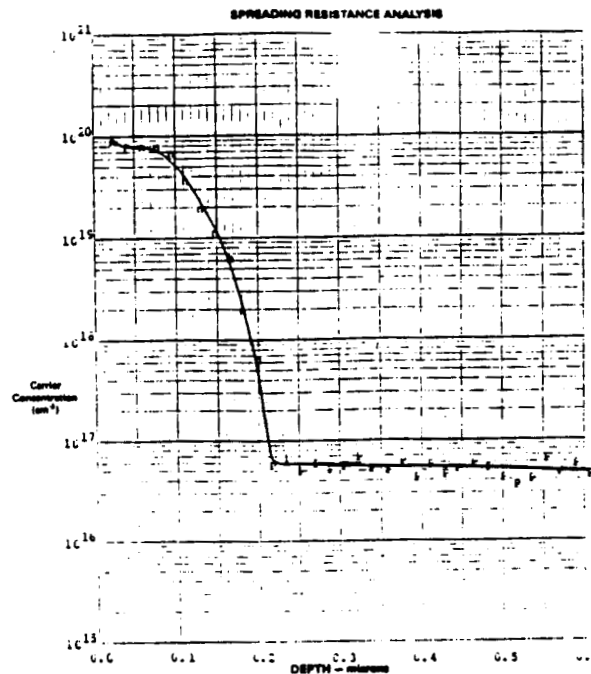


Fig. 4-6b. Spreading resistance depth profile. FZ sample (B51 W<sub>2</sub> #3), ion implanted at 5 keV with <sup>62</sup>P<sub>2</sub><sup>+</sup> of fluence 2x10<sup>15</sup> atoms/cm<sup>2</sup>.

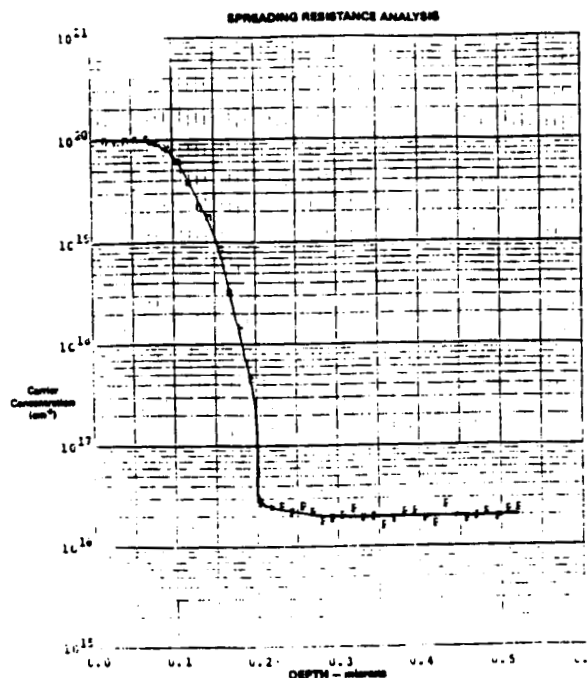


Fig. 4-6c. Spreading resistance depth profile. Cz sample (B51 W<sub>4</sub> #3), ion implanted at 5 keV with <sup>31</sup>P<sub>1</sub><sup>+</sup> ions of fluence 1.8x10<sup>15</sup> atoms/cm<sup>2</sup>.



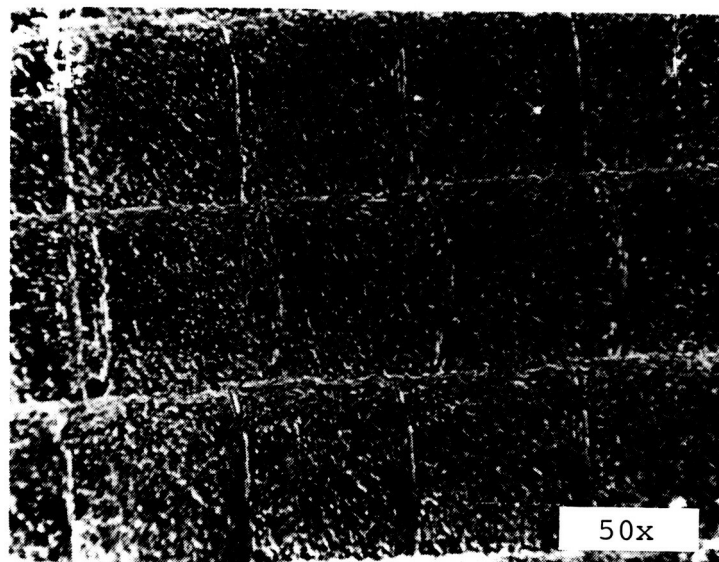


Fig. 4-7. Typical microscopic defects on wafer surface after being annealed at  $1.5 \text{ J/cm}^2$ , double lens, old kaleidoscope optical set up. No etching.

Table 4-9. Electrical measurements on B54 and B55.  $^{62}\text{P}_2^+$  ion implant at 5 keV,  $2.5 \times 10^{15} \text{ atoms/cm}^2$ .

Sample No.	Laser Energy (J/cm <sup>2</sup> )	Sheet Rho (ohm/sq)	J <sub>sc</sub> (mA/cm <sup>2</sup> )	V <sub>oc</sub> (V)	FF (%)	Eff (%)	Contact % Shadow
B54W							
#1	1.53	85	20.44	0.584	78.24	9.33	8-9%
#2			20.70	0.584	77.50	9.36	"
#3			18.92	0.577	69.16	7.56	<10%
#4			20.64	0.583	76.66	9.22	8-9%
-----							
B55W							
#1	1.43	70	21.19	0.585	77.65	9.62	7%
#2			21.59	0.587	75.63	9.58	"
#3			21.52	0.586	78.89	9.89	"
#4			21.21	0.585	78.12	9.69	"

Although the junctions formed here (Table 4-10) were deeper than previous experiments, as indicated by the lower sheet resistivities, both the  $\text{V}_{\text{OC}}$  and  $\text{J}_{\text{SC}}$  were comparatively higher on average. A fill factor as high as 78.5% was also obtained (B12-2.5E #1). Results suggested the advantage of a more powerful laser of larger beam size with more output uniformity that allowed less total overlap.

**Table 4-10.** First experimental result with the larger laser, at density 1.3 and 1.6 J/cm<sup>2</sup> respectively.

Cell ID (FZ)	Energy Density (J/cm <sup>2</sup> )	Over-lap (%)	Pulse Duration (ns)	V <sub>OC</sub> (V)	J <sub>SC</sub> (mA/cm <sup>2</sup> )	FF (%)	Eff (%)	Sheet Rho (ohms/sq)
B11, 5 keV at 2.5x10 <sup>15</sup>								
#1	1.3	20	80	0.569	21.47	67.95	8.31	46-65
#2	1.3	20	80	0.581	21.06	62.15	7.60	46-65
#4	1.3	20	80	0.587	21.53	74.18	9.37	46-65
#5	1.3	20	80	0.583	21.36	67.56	8.41	46-65
B12, 5 keV at 2.5x10 <sup>15</sup>								
#1	1.6	8	80-90	0.593	20.14	78.50	9.38	40-53
#2	1.6	8	80-90	0.580	20.02	71.17	8.26	40-53
B12, 5 keV at 5x10 <sup>15</sup>								
#1	1.6	8	80-90	0.593	20.40	70.62	8.55	26-32
#2	1.6	8	80-90	0.593	20.54	73.89	9.01	26-32

Two more experiments with different combinations of energy and percent of overlap were then immediately conducted: 0.95 J/cm<sup>2</sup> with 9% overlap and 1.1 J/cm<sup>2</sup> with 7% overlap, respectively. Results are summarized in Table 4-11.

**Table 4-11.** Results of annealing by the larger laser with lower energy density and overlap %, 5 keV at 5x10<sup>15</sup>.

Cell ID (FZ)	Energy Density (J/cm <sup>2</sup> )	Over-lap (%)	V <sub>OC</sub> (V)	J <sub>SC</sub> (mA/cm <sup>2</sup> )	FF (%)	Eff (%)	Sheet Rho (ohms/sq)
B13							
#1	0.95	9	0.495	21.30	49.93	5.26	>100
#2	0.95	9	0.531	20.80	52.29	5.78	>100
#4	0.95	9	0.425	21.81	41.87	3.88	>100
#5	0.95	9	0.554	21.54	52.80	6.30	>100
B14							
#1	1.10	7	0.531	22.71	58.78	7.09	68-80
#2	1.10	7	0.533	22.99	58.80	7.20	68-80
#3	1.10	7	0.512	22.69	53.58	6.23	68-80
#4	1.10	7	0.477	20.37	44.59	4.33	68-80

All cells showed high series resistance and high shunt conductivity due to shallow junction as well as insufficient overlap. The other factor considered to be contributing to the low V<sub>OC</sub> was the presence of ion implantation damage that was not removed at such low energy densities. Results so far suggest

that the threshold energy for complete annealing is between 1.3 J/cm<sup>2</sup> and 1.6 J/cm<sup>2</sup>. In fact, the subsequent experiment continued with the large laser set at 1.45 J/cm<sup>2</sup> which yielded much better cell efficiency on lightly doped wafers (Table 4-12).

**Table 4-12.** Electrical performance of large laser processed Cz cells. No AR coating. Implant energy = 5 keV; ion fluence =  $1 \times 10^{15}$  atoms/cm<sup>2</sup>. Cells measured at AM1.5, 25°C. Laser energy density = 1.45 J/cm<sup>2</sup>; overlap = 12%.

Cell ID	J <sub>sc</sub> (mA/cm <sup>2</sup> )	V <sub>oc</sub> (V)	FF (%)	Eff (%)
B16				
#1	21.16	0.576	74.58	9.10
#2	21.57	0.578	76.94	9.60
#3	19.62	0.571	76.01	8.52
#4	21.61	0.574	75.08	9.32

#### **4.2.2 Improved Small Laser EXC-1 With Single Lens Focusing**

The above results demonstrate that ion implantation at 5 keV with fluence between 1 to  $2.5 \times 10^{15}$  atoms/cm<sup>2</sup> could produce high efficiency cells if the laser output is sufficiently uniform. However, the slow pulse rate of the large laser (1 pulse per 2 minutes) made it impractical for extensive experimentation and production application. Thereafter, efforts were devoted to improving uniformity of the smaller laser which has a repetitive rate as fast as 25 Hz. The improvement was accomplished by the installation of kaleidoscopes (Section 3.5.1.2) with single lens focusing. The first experiment with the improved small laser, EXC-1, was to redefine the energy density range, which is highly dependent on pulse shape and pulse duration. The melt penetration depth for 30 nsec of the EXC-1 laser could be almost 50% deeper than 90 nsec of Lucy at the same laser energy density (R. Young et al., 1983).<sup>1</sup> The threshold annealing energy density, therefore, is different for the two lasers. Due to the difference in beam uniformity, beam overlap percentage is also a critical parameter. Detailed annealing parameters were listed in Table 3-1, Section 3.5.1.4, Experimental Equipment.

##### **4.2.2.1 p-Type Substrate with 31p<sup>+</sup> Ion Implant Dopant**

The experiment (B22) with the small laser began by using the same Cz material and ion implantation (5 keV,  $2.5 \times 10^{15}$  atoms/cm<sup>2</sup>) as for B19 and B20 that were processed by Lucy. Laser energy density was set at 1.6 J/cm<sup>2</sup> with 50% and 20% overlap, respectively, and 2.0 J/cm<sup>2</sup> with 20% overlap. For comparison, samples that were 5 keV ion implanted at  $1 \times 10^{15}$  atoms/cm<sup>2</sup> dosage were also annealed at 1.6 J/cm<sup>2</sup> with 20% overlap. Such ion

implanted material had been demonstrated to yield cells with efficiencies  $>9.5\%$  in three consecutive runs (B16, B17, B18) processed by the larger laser (Section 4.2.1).

As indicated by Table 4-13, results of the whole experiment (B22) were poor. Even the  $1 \times 10^{15}$  atoms/cm<sup>2</sup> samples (B22-V) were degraded in both  $V_{oc}$  and fill factor compared with previous runs reported earlier.

Comparing the electrical performance of B22-II (50% overlap) with B22-III (20% overlap), both annealed at 1.6 J/cm<sup>2</sup> energy density, it was clear that the low  $V_{oc}$  (0.55 V) of the latter (20% overlap) was due to incomplete surface annealing because of the beam's inhomogeneity. As overlap was increased to 50% (B22-II), the  $V_{oc}$  was improved to 0.583 V, similar to previous results obtained from the larger laser. The poor fill factor was believed to be due to surface contamination. This was the key observation of the importance of surface cleanliness to final cell performance, which is discussed in detail below.

Incomplete surface annealing due to insufficient overlap was further demonstrated by increasing the energy density to 2.0 J/cm<sup>2</sup> (B22-IV) while keeping overlap to 20%. No further improvement in  $V_{oc}$  was obtained. Laser scanning (Fig. 4-8a) over the surface indicated current sink points along the overlap area, suggesting heavy damage due to localized overheating. A cell from this group was preferentially etched with Secco etchant after metal contacts were removed. The optical photo revealed massive surface defects (Fig. 4-8b).

The results from B22 suggest that 20% overlap was not sufficient to compensate for beam nonuniformity. Also, even 1.6 J/cm<sup>2</sup> was too high at 30 nsec pulse (double peaks) duration to cause surface damage.

The next experiment, B23, was conducted to study defects vs laser energy from 1.1 J/cm<sup>2</sup> to 1.3 J/cm<sup>2</sup> with 50% overlap. Samples were then Secco etched. Optical photos at 50x are presented in Fig. 4-9, and laser parameters and sheet resistivities are summarized in Table 4-14. Results suggest that 1.3 J/cm<sup>2</sup> with 50% overlap apparently produced the ideal range in sheet resistivity for dosages of  $2.5 \times 10^{15}$  to  $5 \times 10^{15}$  atoms/cm<sup>2</sup>, while the surface concentration was low for the  $1 \times 10^{15}$  atoms/cm<sup>2</sup> dosage.

The degree of surface damage due to the imprint of the laser beam was apparently quite different for 1.1 J/cm<sup>2</sup> and 1.3 J/cm<sup>2</sup> (Fig. 4-9). Provided that the laser output and pulse shape were reproducible, the annealing threshold energy in optimizing dopant activation vs surface damage for the EXC-1 small laser would be very close to 1.3 J/cm<sup>2</sup> with 50% overlap. Whether it can provide complete lattice damage removal caused by 5 keV  $^{31}P^+$  ion implant is not determined.

**Table 4-13.** Laser annealing by improved small laser on ion-implanted Cz wafers. Implant energy 5 keV.

- a. Ion fluence =  $2.5 \times 10^{15}$  atom/cm<sup>2</sup>; energy density = 1.6 J/cm<sup>2</sup>; overlap = 50%.

Cell ID	Sheet Rho (ohm/sq)	J <sub>sc</sub> (mA/cm <sup>2</sup> )	V <sub>oc</sub> (V)	FF (%)	Eff (%)
B22-II					
#1	38-40	19.84	0.579	66.05	7.59
#2	"	19.76	0.587	70.97	8.24
#3	"	18.97	0.576	60.44	6.61
#4	"	20.22	0.583	70.43	8.31

- b. Ion fluence =  $2.5 \times 10^{15}$  atom/cm<sup>2</sup>; energy density = 1.6 J/cm<sup>2</sup>; overlap = 20%.

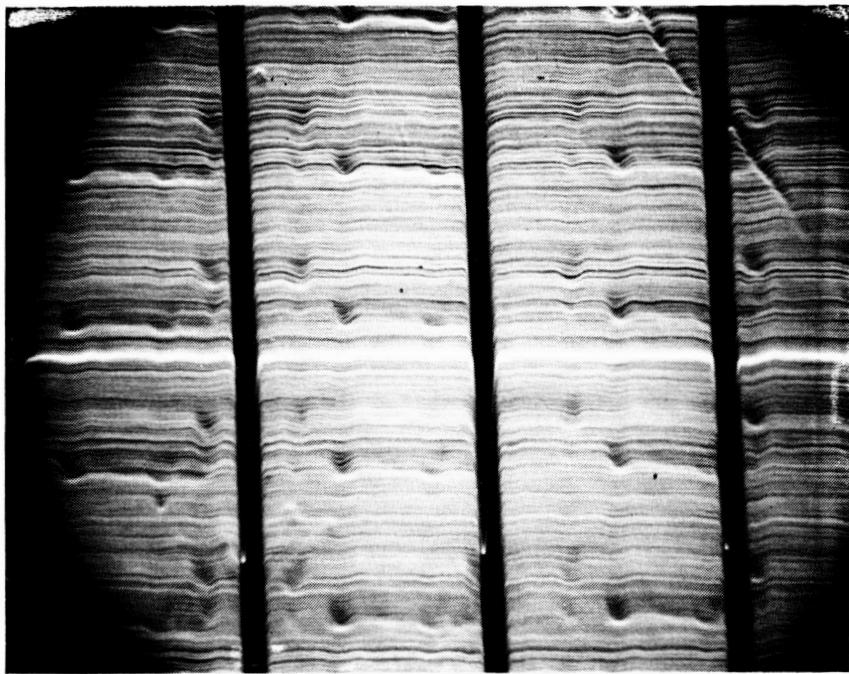
Cell ID	Sheet Rho (ohm/sq)	J <sub>sc</sub> (mA/cm <sup>2</sup> )	V <sub>oc</sub> (V)	FF (%)	Eff (%)
B22-III					
#1	38-40	19.26	0.542	34.34	3.59
	"	20.07	0.557	46.23	5.17
	"	19.51	0.566	44.82	4.95
	"	19.09	0.541	34.62	3.57

- c. Ion fluence =  $2.5 \times 10^{15}$  atom/cm<sup>2</sup>; energy density = 2.0 J/cm<sup>2</sup>; overlap = 20%.

Cell ID	Sheet Rho (ohm/sq)	J <sub>sc</sub> (mA/cm <sup>2</sup> )	V <sub>oc</sub> (V)	FF (%)	Eff (%)
B22-IV					
#1	>100	21.00	0.507	69.72	7.74
#2	"	22.06	0.493	65.84	7.71
#3	"	21.37	0.492	70.29	7.39
#4	"	20.03	0.458	48.77	4.48
#5	"	- - -	Broken	- - -	
#6	"	21.92	0.500	66.95	7.34
#7	"	20.39	0.457	51.58	4.80
#8	"	21.44	0.487	62.35	6.51

- d. Ion fluence =  $1 \times 10^{15}$  atom/cm<sup>2</sup>; energy density = 1.6 J/cm<sup>2</sup>; overlap = 20%.

Cell ID	Sheet Rho (ohm/sq)	J <sub>sc</sub> (mA/cm <sup>2</sup> )	V <sub>oc</sub> (V)	FF (%)	Eff (%)
B22-V					
#1	92	20.49	0.577	73.48	8.68
#2	"	20.29	0.574	70.34	8.20
#3	"	20.71	0.578	67.15	8.04
#4	"	21.29	0.577	67.97	8.35



- a.  $2.0 \text{ J/cm}^2$ , 20% overlap laser annealed cell. Dark vertical lines are contact fingers. Dimpled structures are damaged areas along annealing directions, faintly observable.



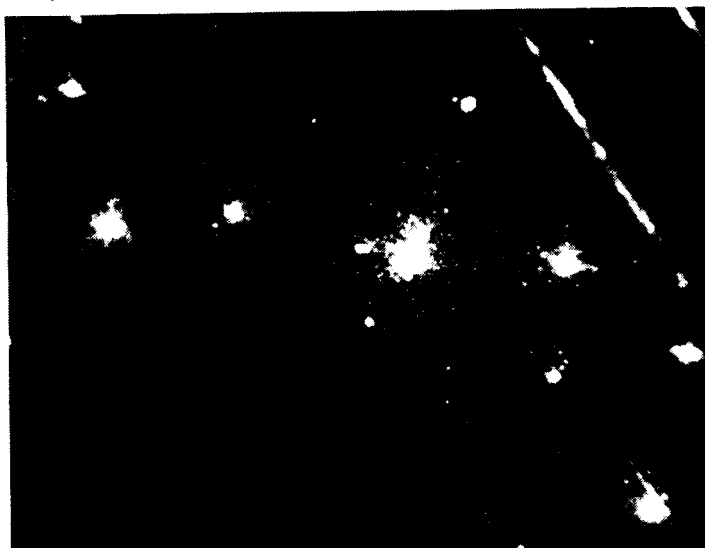
- b. Surface appearance after preferential etch. Imprints of the laser beam are recognizable.

Fig. 4-8. Laser scan showing incomplete surface annealing.

ORIGINAL PAGE IS  
OF POOR QUALITY



a. 1.3 J/cm<sup>2</sup>



b. 1.3 J/cm<sup>2</sup>



c. 1.1 J/cm<sup>2</sup>

Fig. 4-9. Surface damage revealed by etching.

The surface damage that appeared on sample B23-I (Fig. 4-9a) was of a crystallographic type. Although the exact cause is not determined yet, it is possibly due to surface contamination. Such contamination acted as nuclei for recrystallization during the melting-solidification process. Both epitaxial regrowth and free (no constraint) recrystallization are clearly distinguishable by the (100) and (111) structures at such defects.

**Table 4-14.** Sheet resistivity of wafers. Implant energy 5 keV, overlap 50%.

Cell ID	Crystal Zoning	Base Resistivity (ohms-cm)	Ion Fluence ( $\times 10^{15}$ atoms/cm <sup>2</sup> )	Laser Energy (J/cm <sup>2</sup> )	Sheet Rho (ohms/sq)
B23					
-I	FZ	0.3	5	1.3	22-24
-II	Cz	0.7-0.9	2.5	1.3	52
-III	Cz	0.7-0.9	1	1.1	85-90

An experiment (B24) immediately following the test run was then conducted with 50% beam overlap at 1.4 J/cm<sup>2</sup> energy density. Material included Cz (0.7 ohm-cm p-type) ion implanted at 5 keV with  $1 \times 10^{15}$  and  $2.5 \times 10^{15}$  atoms/cm<sup>2</sup> respectively, and FZ (0.3 ohm-cm, p-type) ion implanted at 5 keV with  $5 \times 10^{15}$  atoms/cm<sup>2</sup> fluence. Originally there were four wafers 2x2 cm in size prepared from each group. Some wafers were used for defect studies, leaving only seven pieces for final metallization. Results of electrical performance are summarized in Table 4-15.

While the average  $J_{sc}$  was in the same range as previous experiments, the fill factor was strikingly improved from 40-62% in previous experiments to over 74-78% in this run (B24). The  $V_{oc}$  was also increased to as high as 0.594 V (B24-II #3). The FZ sample in the same experiment had  $V_{oc}$  of 0.61 V. The higher  $V_{oc}$  obtained in the FZ sample was due to its lower base resistivity (0.3 ohm-cm vs 0.7 ohm-cm in Cz). The maximum cell efficiency from this experiment (B24) was 9.77% (B24-II #3). The large variations in fill factors among these cells are thought to be due to surface conditions discussed below.

Using information obtained from B23 and B24 that included laser energy density, overlap ratio, and surface conditions, a summary experiment (B26) was conducted. Material used consisted of Cz (0.7 ohm-cm) and FZ (0.3 ohm-cm). Wafers were cleaned by scrubbing in detergent, 10% HF acid etching,  $H_2SO_4 + H_2O_2$ , HF acid etching, and finally soaking in HCl acid before deionized water rinsing. Although water spots were still present, their density was drastically decreased. Due to the unavailability of equipment for adequate scrubbing, surface scratches were observed



on some wafers. Ion implant energy was 5 keV on both Cz and FZ wafers. The dosage for CZ was  $1 \times 10^{15}$  atoms/cm<sup>2</sup> and  $2.5 \times 10^{15}$  atoms/cm<sup>2</sup>, and  $5 \times 10^{15}$  atoms/cm<sup>2</sup> for FZ material. The results are summarized in Table 4-16.

Cells processed from 5 keV ion implant with dosage  $1 \times 10^{15}$  atoms/cm<sup>2</sup> were slightly better than in the previous experiment (B24) in  $J_{sc}$  and fill factor. Cells from dosage  $2.5 \times 10^{15}$  atoms/cm<sup>2</sup>, however, had obvious improvements in both  $J_{sc}$  and fill factor. While the increased  $J_{sc}$  is not immediately explainable, the improvement in fill factor is most likely due to surface cleanliness.

**Table 4-15.** Electrical performance of B24 cells. Implant energy 5 keV, energy density 1.4 J/cm<sup>2</sup>, overlap 50%.

a. Cz cells. Ion fluence =  $1 \times 10^{15}$  atom/cm<sup>2</sup>.

Cell ID	Sheet Rho (ohm/sq)	$J_{sc}$ (mA/cm <sup>2</sup> )	$V_{oc}$ (V)	FF (%)	Eff (%)
B24-I					
#1	90	21.06	0.581	76.63	9.38
#2	"	21.26	0.581	76.80	9.50

b. Cz cells. Ion fluence =  $2.5 \times 10^{15}$  atom/cm<sup>2</sup>.

Cell ID	Sheet Rho (ohm/sq)	$J_{sc}$ (mA/cm <sup>2</sup> )	$V_{oc}$ (V)	FF (%)	Eff (%)
B24-II					
#1	46	20.88	0.593	78.10	9.66
#2	"	20.88	0.593	73.61	9.06
#3	"	21.26	0.594	77.40	9.77

c. FZ cells. Ion fluence =  $5 \times 10^{15}$  atom/cm<sup>2</sup>.

Cell ID	Sheet Rho (ohm/sq)	$J_{sc}$ (mA/cm <sup>2</sup> )	$V_{oc}$ (V)	FF (%)	Eff (%)
B24-III					
#1	23	21.49	0.611	73.63	9.67
#2	"	21.37	0.607	67.93	8.81

Table 4-16. Small laser (EXC-1) annealing of Cz and FZ wafers. Ion implanted with  $+p^{31}$  at 5 keV; 18-grid evaporated-type metallization; AR coated. Cells measured at 25°C AM1.5 calibrated with JPL standard cell MT-472.

- a. Cz cell. Ion fluence =  $1 \times 10^{15}$  atom/cm<sup>2</sup>; laser energy density = 1.5 J/cm<sup>2</sup>; overlap = 50%; pulse duration = ~30 ns.

Cell ID	Sheet Rho (ohm/sq)	J <sub>sc</sub> (mA/cm <sup>2</sup> )		V <sub>oc</sub> (V)		FF (%)		Eff (%)	
		Pre AR	Post AR	Pre AR	Post AR	Pre AR	Post AR	Pre AR	Post AR
B26-1E									
#1	80-90	21.24	31.74	0.584	0.598	78.76	78.26	9.76	14.85
#2	"	21.24	31.86	0.584	0.599	78.31	78.31	9.73	14.94
#3	"	21.37	---	0.585	---	76.57	---	9.57	---
#4	"	20.80	---	0.581	---	77.33	---	9.35	---

- b. Cz cell. Ion fluence =  $2.5 \times 10^{15}$  atom/cm<sup>2</sup>; laser energy density = 1.5 J/cm<sup>2</sup>; overlap = 50%; pulse duration = ~30 ns.

Cell ID	Sheet Rho (ohm/sq)	J <sub>sc</sub> (mA/cm <sup>2</sup> )		V <sub>oc</sub> (V)		FF (%)		Eff (%)	
		Pre AR	Post AR	Pre AR	Post AR	Pre AR	Post AR	Pre AR	Post AR
B26-2.5E									
#1	44-48	21.44	31.79	0.596	0.610	79.44	79.50	10.15	15.4
#2	"	21.62	32.45	0.596	0.612	79.36	79.51	10.22	15.78
#3	"	21.32	32.06	0.594	0.610	79.74	79.63	10.10	15.57
#4	"	21.50	32.68	0.595	0.604	78.76	74.63	10.08	14.73

- c. FZ cell. Ion fluence =  $5 \times 10^{15}$  atom/cm<sup>2</sup>; laser energy density = 1.5 J/cm<sup>2</sup>; overlap = 50%; pulse duration = ~30 ns.

Cell ID	Sheet Rho (ohm/sq)	J <sub>sc</sub> (mA/cm <sup>2</sup> )		V <sub>oc</sub> (V)		FF (%)		Eff (%)	
		Pre AR	Post AR	Pre AR	Post AR	Pre AR	Post AR	Pre AR	Post AR
B26-5E									
#1	66-75	19.94	---	0.579	---	75.65	---	8.71	---
#2	"	19.68	---	0.585	---	78.06	---	8.95	---
#3	"	20.22	---	0.588	---	76.95	---	9.39	---
#4	"	20.01	---	0.589	---	76.79	---	9.04	---
#5	"	20.08	---	0.587	---	77.32	---	9.11	---
#6	"	- - - Shunted - - -							

The maximum and minimum efficiency of group B26-2.5E is 10.22% and 10.08% respectively before AR, with 18 gridlines producing 9% shadowing. These cells were sent to ASEC for AR coating. The best cell (B26-2.5E #2) had an efficiency of almost 15.8%. The light and dark I-V curves of this cell are presented in Fig. 4-10; Fig. 4-11 shows the spectral response at AM1.5.

Results from the FZ material with ion fluence of  $5 \times 10^{15}$  atoms/cm<sup>2</sup>, however, had a poor result in all respects. From this experiment, it is obvious that ion implant energy near 5 keV with fluence about  $3 \times 10^{15}$  atoms/cm<sup>2</sup> is capable of producing a high efficiency cell.

The experiment (B28) was repeated for the two Cz wafers (2"x2") with  $2.5 \times 10^{15}$  atoms/cm<sup>2</sup> fluence at the similar laser settings except slightly decreased in energy density from 1.5 J/cm<sup>2</sup> to 1.45 J/cm<sup>2</sup>. Cells were processed utilizing photolithographic metallization techniques followed by AR coatings. Results are shown in Table 4-17.

Both  $J_{sc}$  and  $V_{oc}$  of this run were almost equal to the previous one. It was the fill factor that differed significantly and is believed to be due to either the laser annealing process or initial surface condition, or both, rather than the cell processing.

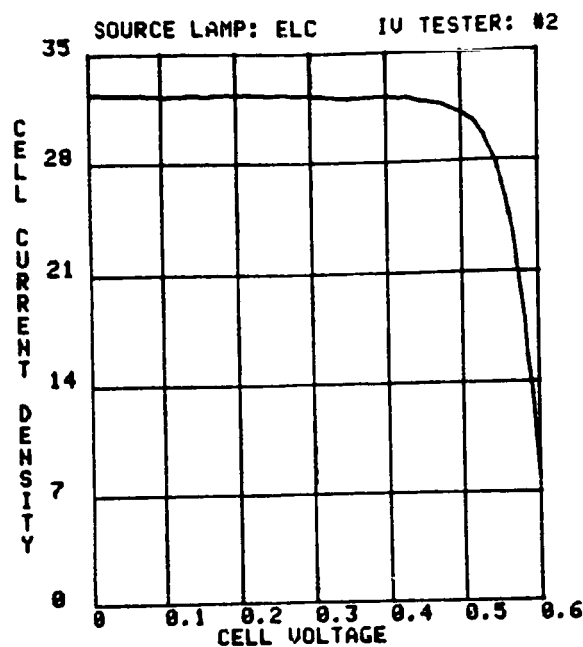
#### **4.2.2.2 n-Type Substrate with $11B^+$ Ion Implant Dopant**

Experiments with n-type wafers were performed with the improved small (EXC-1) laser. Material used was 4" n-type Cz (1 ohm-cm) 18 mils thick. The front side was  $11B^+$  ion implanted at 5 keV with a dosage of  $2.5 \times 10^{15}$  atoms/cm<sup>2</sup>. After cleaning, the wafers were annealed at 1.52 J/cm<sup>2</sup> with 50% overlap at 1.5 J/cm<sup>2</sup>. The backs were then coated with spin-on phosphorus dopant as the n<sup>+</sup> layer and diffused with laser energy of 2.6-2.7 J/cm<sup>2</sup>. Contacts were of the 18 gridline evaporated type. Some of the better cells were AR coated as summarized in Table 4-18.

The highest efficiency obtained was 15% after AR (B27N #3). The current was higher than for a p-type substrate of 0.7 ohm-cm while the  $V_{oc}$  was lower. The junction depth profile on the emitter and the back surface showed satisfactory depth with high surface concentration on both areas (Fig. 4-12).

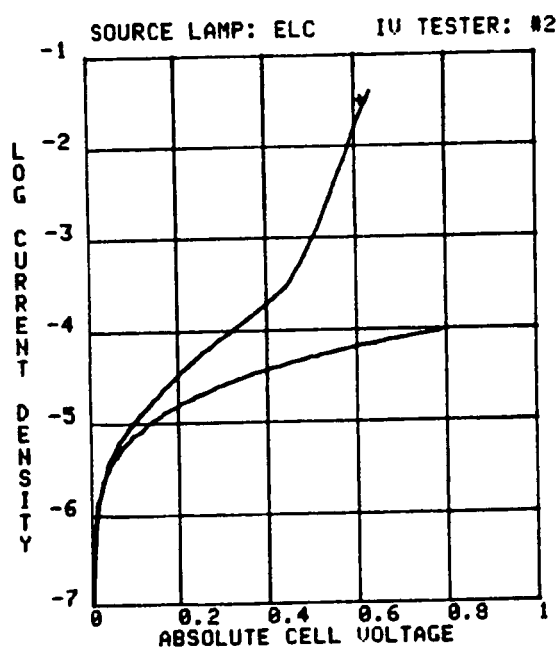
#### **4.2.2.3 Small Laser With Double Focus Lens**

The laser spot in the above experiments with single lens focusing was slightly "fuzzy." A second focus lens was installed to produce a sharper imprint. However, results were poorer compared with B26. Table 4-19 represents a typical example.



SINGLE/POLY  
 LIGHT IV AT 25C  
 OPERATOR: DW  
 CELL: B26 E2.5 #2  
 Date/time: 17-NOV-84 12:17:03  
 AREA: 4.00 (sq.cm)  
 Isc: 0.130 (amps)  
 Jsc: 32.45 (ma/sq)  
 Voc: 0.612 (volts)  
 Ipm: 0.123 (amps)  
 Jpm: 30.67 (ma/sq)  
 Upm: 0.514 (volts)  
 Pm: 0.063 (watts)  
 Cff: 79.51 %  
 Eff: 15.78 %

A/R BY ASEC  
 HEAT TREATED  
 P SUBSTRATE



SINGLE/POLY  
 DARK IV AT 25C  
 Date/time: 17-NOV-84 12:17:31  
 OPERATOR: DW  
 CELL: B26 E2.5 #2  
 AREA: 4.00 (sq.cm)  
 Gsh: 4.46E-004 (mho)  
 gsh: 3.81E-006  
 gsh: 1.11E-004 (mho/sq.cm)  
 Rsr: 9.93E-002 (ohm)  
 rsr: 3.97E-001 (ohm-sq.cm)

A/R BY ASEC  
 HEAT TREATED  
 P SUBSTRATE

Fig. 4-10. I-V curves of best cell from B26-2.5E.

Sample: B26 2.5E15, A/R BY ASEC, HEAT TREATED #2

Voltage: 0.000 Volts Light Bias: N

Date/time: 17-NOV-84 12:21:12 Operator: DH

System Calibrated 17-NOV-84 11:55:23 Standard Cell 0325

Data stored: CSR:QEJBTDCZ/B26\_2E15\_2\_00.DW

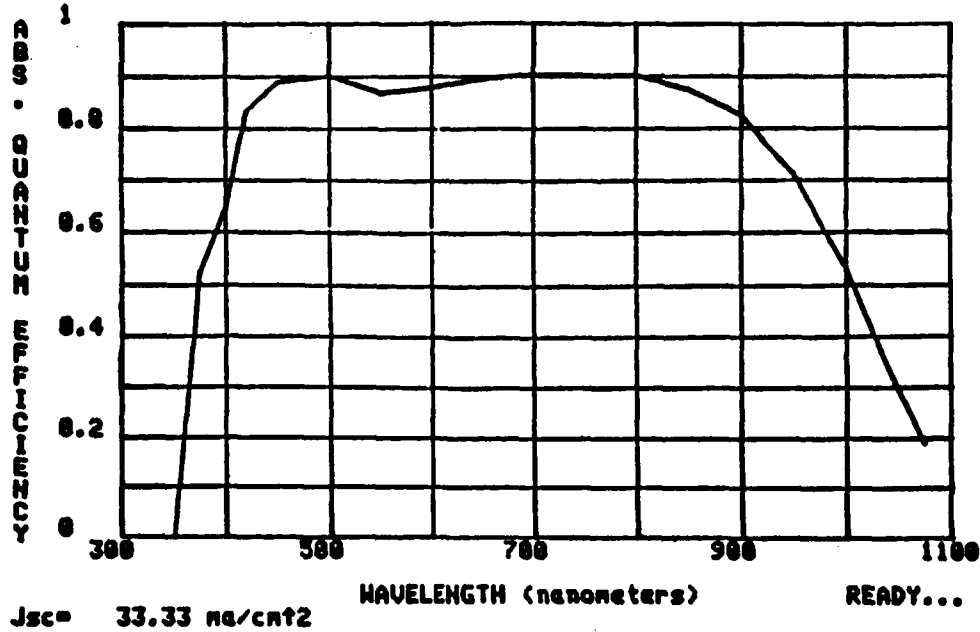


Fig. 4-11. Spectral response of best cell from B26-2.5E.

Table 4-17. ASEC-coated Cz cells; photolithographic gridlines. Implant energy 5 keV, ion fluence  $2.5 \times 10^{15}$  atoms/cm<sup>2</sup>, laser energy density 1.47 J/cm<sup>2</sup>, overlap 50%, and pulse duration ~30 ns.

Cell ID	Sheet Rho (ohm/sq)	J <sub>sc</sub> (mA/cm <sup>2</sup> )	V <sub>oc</sub> (V)	FF (%)	Eff (%)
B28 ASEC I					
#1	44-48	31.59	0.603	76.75	14.61
#2	"	31.42	0.605	79.09	15.04
#3	"	31.89	0.606	78.49	15.17
#4	"	31.22	0.606	80.46	15.23
-----					
B28 ASEC II					
#1	44-48	31.55	0.603	53.61	10.21
#2	"	31.98	0.605	75.71	14.66
#3	"	31.65	0.603	78.90	15.06
#4	"	31.13	0.597	74.89	13.93

Table 4-18. n-type substrates processed by small laser. Contacts were of the 18 gridline evaporated type. Ion implant energy 5 keV, ion fluence  $2.5 \times 10^{15}$  atoms/cm<sup>2</sup>, overlap 50%. Laser energy density 1.52 J/cm<sup>2</sup>.

Cell ID	Sheet Rho (ohm/sq)	J <sub>sc</sub> (mA/cm <sup>2</sup> )		V <sub>oc</sub> (V)		FF (%)		Eff (%)	
		Pre AR	Post AR	Pre AR	Post AR	Pre AR	Post AR	Pre AR	Post AR
B27N									
#1	53	22.03	31.73	0.583	0.595	77.68	77.84	9.98	14.70
#2	"	21.34	29.18	0.581	0.589	78.39	77.76	9.73	13.36
#3	"	22.02	32.68	0.582	0.597	77.21	76.93	9.89	15.00
#4	"	21.79	32.15	0.583	0.594	77.71	77.42	9.86	14.79

The lower V<sub>oc</sub> and poorer fill factor compared with B26 process with a single lens are due to more severe surface damage by the sharper beam structure. In addition, there are more microstructural defects observed in a rather consistent pattern. This is believed partly due to surface contamination and the defective kaleidoscope. In one later stage, as the kaleidoscope was replaced, such defects disappeared, leaving only sharp edge imprints of the laser beam. Results also suggested removal of the second focussing lens so as to reduce the edge damage.

### 4.3 SURFACE CONDITIONS

#### 4.3.1 Cleaning Procedure

As mentioned earlier, surface cleaning was observed to affect the performance in V<sub>oc</sub> and fill factor of laser annealed cells more seriously than conventional, thermally diffused cells. The main reason is that laser annealing is a process that brings the surface temperature to near melting and recrystallization. Dirt specks on the surface become nucleation sites for crystallographic defects during annealing. Figure 4-13 is a good example of such defects formed after 1.3 J/cm<sup>2</sup> laser annealing. Both epitaxial regrowth and free (no-constraint) recrystallization are clearly distinguishable by the (100) and (111) structures respectively at such defects.

Light scrubbing with cloth and detergent was found capable of reducing, but not totally removing, the surface contamination. However, such a cleansing procedure was detrimental to the ion implanted surface.

Samples of 3" diameter FZ p-type wafers with 5 keV 31p<sup>+</sup> ion implant were divided into lots to test for the effects of different surface preparation techniques (Fig. 4-14).

ORIGINAL PAGE IS  
OF POOR QUALITY

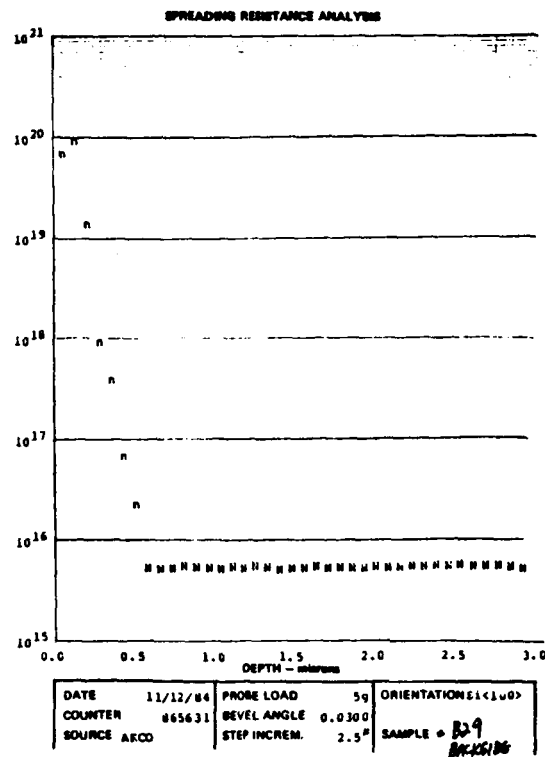
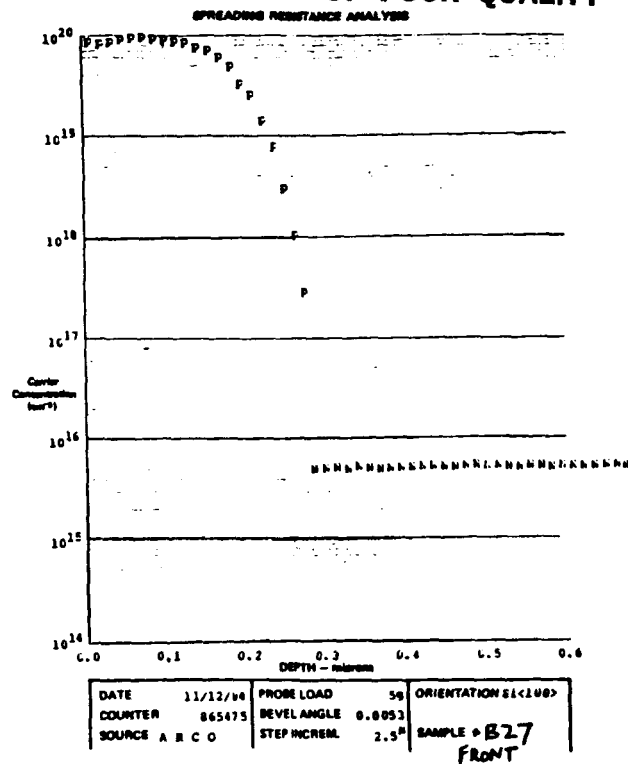


Fig. 4-12. Depth profiles of B27N and B29N.

ORIGINAL PAGE IS  
OF POOR QUALITY

**Table 4-19.** Typical experimental result with laser beam double-focused for a sharper beam structure.

Sample ID	$J_{sc}$ (mA/cm <sup>2</sup> )	$V_{oc}$ (V)	FF (%)	Eff (%)
B49A #1	19.97	0.570	70.71	8.04
A #2	20.86	0.582	74.40	9.03
E #1	20.70	0.582	77.50	9.33
#2	19.50	0.579	77.60	8.76
#3	20.83	0.583	76.72	9.30
#4	20.59	0.586	76.29	9.54
<hr/>				
F #1	21.33	0.586	76.29	9.54
#2	21.22	0.586	76.22	9.48
#3	21.36	0.586	75.12	9.41
#4	21.15	0.586	76.89	9.52



**Fig. 4-13.** Defects formed after 1.3 J/cm<sup>2</sup> annealing.

The in-house chemical cleaning included H<sub>2</sub>SO<sub>4</sub> + H<sub>2</sub>O<sub>2</sub> at elevated temperature followed by 10% HF + 15% HCl etching and rinsing before scrubbing with detergent. The light and hard scrubbing were defined respectively as with and without pressure during scrubbing. Wafers were examined under microscope after laser annealing at 1.3 J/cm<sup>2</sup> or 1.4 J/cm<sup>2</sup> (Fig. 4-15). Results suggest that hard scrubbing damaged the surface by introducing microscratches. However, hard scrubbing on wafers without ion implant did not show scratches after laser annealing, indicating the difference in hardness between the ion implanted layer and the crystalline silicon surface.



Surface damage on wafers cleaned by the vendor was even more severe (Fig. 4-16). Scratches were of the linear type. Microdefects ("haze"), on the other hand, were found to be of lower density than found with scrubbing.

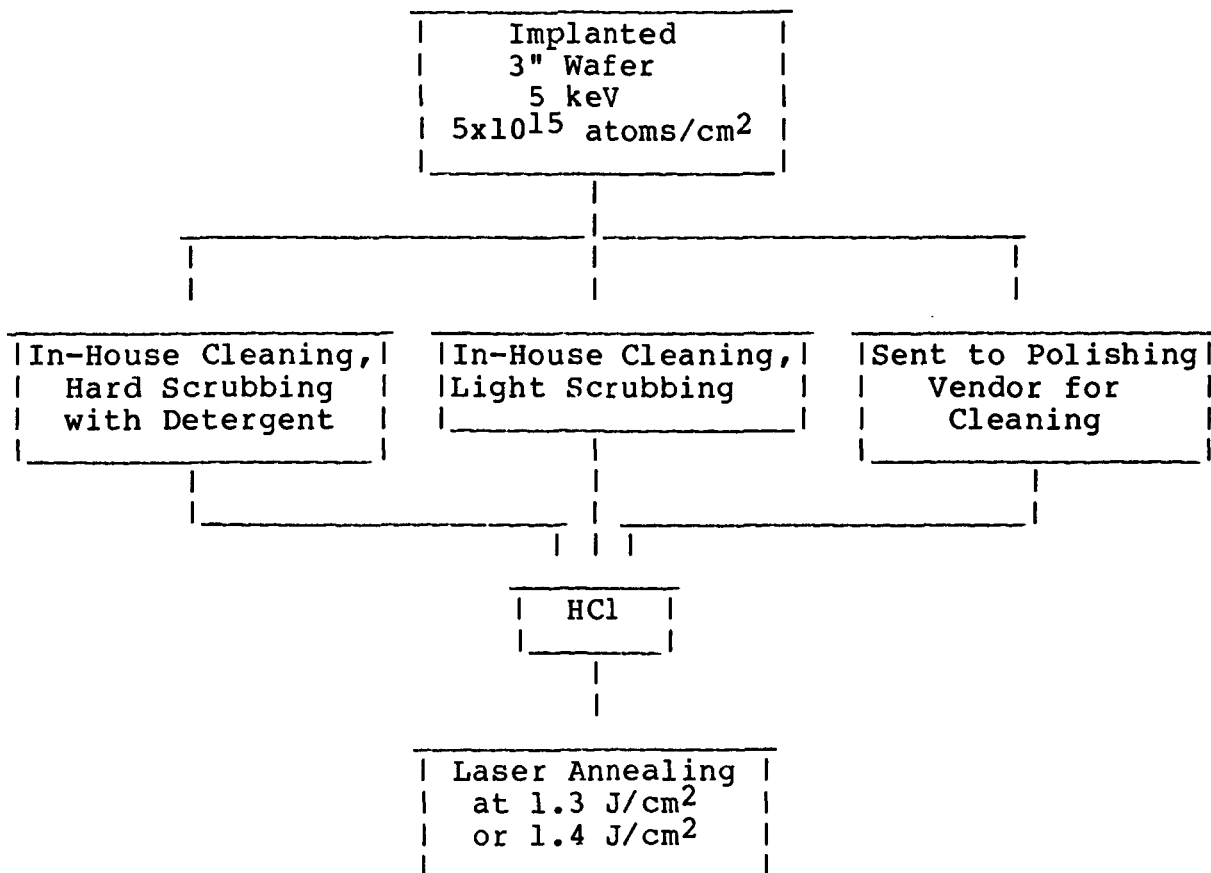


Fig. 4-14. Comparison of surface preparation techniques.

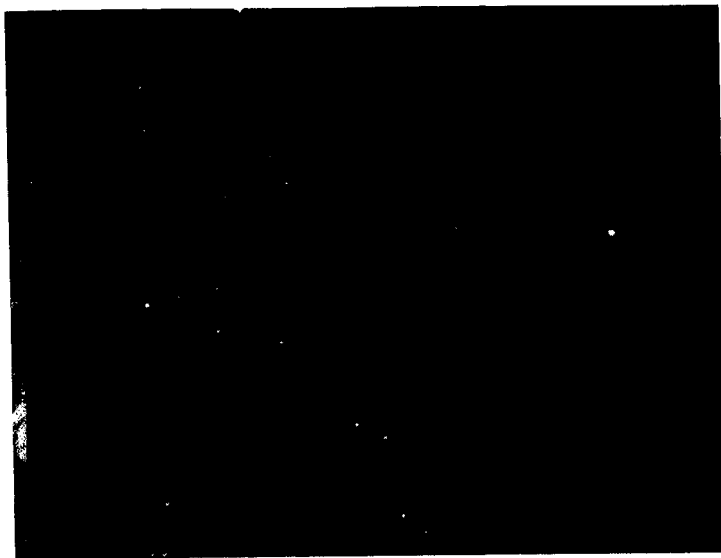
The results suggest, in general, that mechanical scrubbing causes surface damage on ion implanted wafers. However, surface damage defects were not observable prior to laser annealing. Apparently laser annealing of silicon surfaces may be used to reveal surface defects, as an alternative to using preferential etchants such as Sirtl and Secco.

Hard scrubbing on ion implanted wafers apparently almost removed the implant layer. The sheet rho of wafers cleaned with hard scrubbing often exceeded 200 ohms/square.

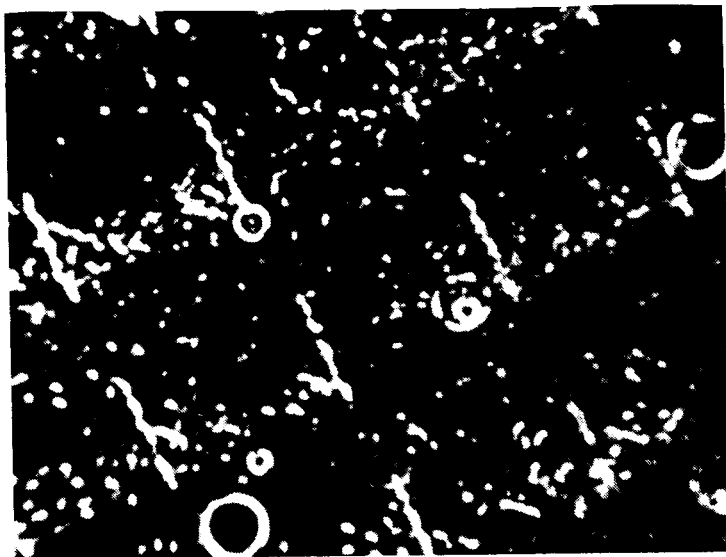
#### 4.3.2 Effects of DI Water

As the laser project progressed, the effects of surface condition and surface contamination on laser annealed cells became better understood.

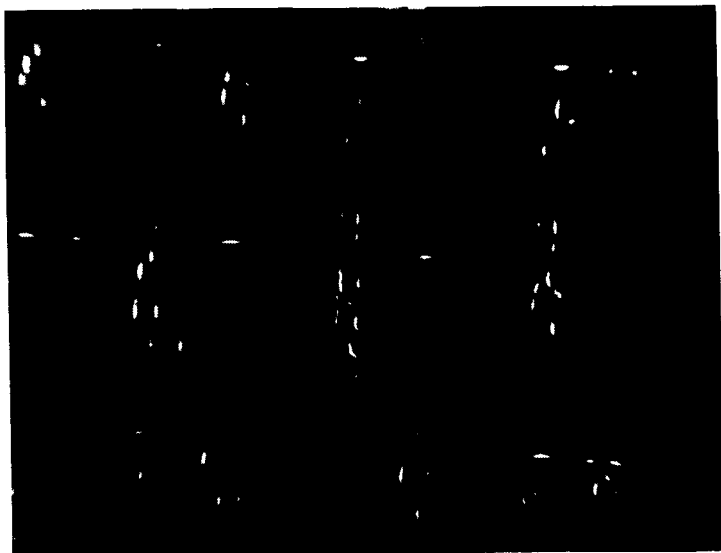
ORIGINAL PAGE IS  
OF POOR QUALITY



a. Light scrubbing; 1.3 J/cm<sup>2</sup>



b. Hard scrubbing; 1.3 J/cm<sup>2</sup>



c. Light scrubbing; 1.4 J/cm<sup>2</sup>



d. Hard scrubbing; 1.4 J/cm<sup>2</sup>

Fig. 4-15. Wafers cleaned in-house and then laser annealed.



Fig. 4-16. Wafer cleaned by vendor after ion implant.

The DI water system was redesigned to upgrade quality. As a result, the water resistance is as high as 18 megohms with 5 micron absolute filtration. Water of such high resistance is usually considered to be excellent DI water quality. However, analysis of accumulated data led to the discovery that water resistance is only one of the basic requirements. The other important factor is the presence of submicron particulates that are apparently non-polarizable and thus not conductive enough to be detected by the resistance probes. Such particulates may cause serious reduction in fill factor of laser annealed cells.

A clear example occurred during the cleaning of wafers before laser annealing, where the water resistance was observed to decrease from 16 megohms to 13 megohms. Water transparency was then tested by shining a coherent light through it. A column of haze was seen, indicating that the light was being scattered by fine particles. Installation of a 2.0 micron filter greatly reduced the haze. The 0.2 micron filter later was found to be completely blocked after 3 hours of water flow. Visual examination of the filter element revealed a slightly yellowish film. The particulates probably came from the incoming source of non-potable water. The particulates were found to contain calcium and iron as oxides.

The cells made from the experiments, with and without the use of a 0.2 micron filter, were electrically characterized (Table 4-20). Also included were control cells that were thermally diffused and metallized simultaneously.

**Table 4-20.** Wafers cleaned without and with 0.2 micron filter. DI water resistance ~16-13 megohms. Wafers ion implanted at 5 keV,  $3 \times 10^{15}$  atoms/cm<sup>2</sup>, laser energy 1.5 J/cm<sup>2</sup>, 50% overlap.

a. Wafers cleaned without 0.2 micron filter.

Sample No.	J <sub>sc</sub> (mA/cm <sup>2</sup> )	V <sub>oc</sub> (V)	FF (%)	Eff (%)
B44-1.5				
#1	20.05	0.580	61.66	7.17
#2	20.43	0.580	70.75	8.40
#3	18.19	0.582	64.35	6.82
#4	17.20	0.575	58.57	5.79
Control R59I				
#1	21.92	0.595	77.54	10.11
#2	22.15	0.596	77.65	10.25

b. Wafers cleaned with 0.2 micron filter.

Sample No.	J <sub>sc</sub> (mA/cm <sup>2</sup> )	V <sub>oc</sub> (V)	FF (%)	Eff (%)
B45-1.5				
#1	19.39	0.583	77.54	8.76
#2	20.26	0.583	76.24	9.01
#3	20.20	0.583	76.84	9.05
#4	19.89	0.583	77.54	8.99
Control B45 R59II				
#1	21.36	0.589	78.09	9.82
#2	21.89	0.591	77.83	10.07

As the data show, the main difference between these two groups of cells is in the fill factor, which is much poorer in cells cleaned without a 0.2 micron filter.

#### 4.4 FINALIZED ANNEALING PROCESS

Based on the experimental results obtained, the annealing process was finalized near the end of the project.

##### 4.4.1 Dopant Source and Methodology

For n<sup>+</sup> junction formation, only ion implant is suitable due to

its controllability and repeatability. Parameters recommended are:

5 keV  
2x10<sup>15</sup> atoms/cm<sup>2</sup>

Lower keV is more desirable if available.

#### 4.4.2 Surface Preparation

The front surface must be free of defects and contamination, meaning a chemically-mechanically finished condition. In addition, the cleaning procedure should include acid etching and spin rinse with high resistance DI water plus submicron filtering. The process is shown in Fig. 4-17.

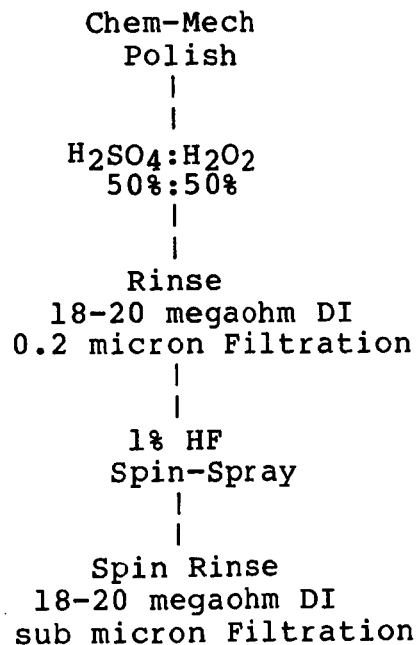


Fig. 4-17. Surface cleaning process.

Such cleaning should be performed before and after ion implant. The final 1% HF and spin etching-rinsing has been very effective in reducing surface contamination such as water spots and dirt.

#### 4.4.3 Laser Parameters

Due to the laser inhomogeneity, a kaleidoscope was added to improve the uniformity while 50% overlap was still necessary for complete annealing. Single lens focusing was found best in reducing edge and surface damage. The best energy density was about 1.4 J/cm<sup>2</sup> for 5 keV ion implant. Shallower implant required less energy density for complete annealing. The final selected process sequence is summarized in Fig. 4-18.

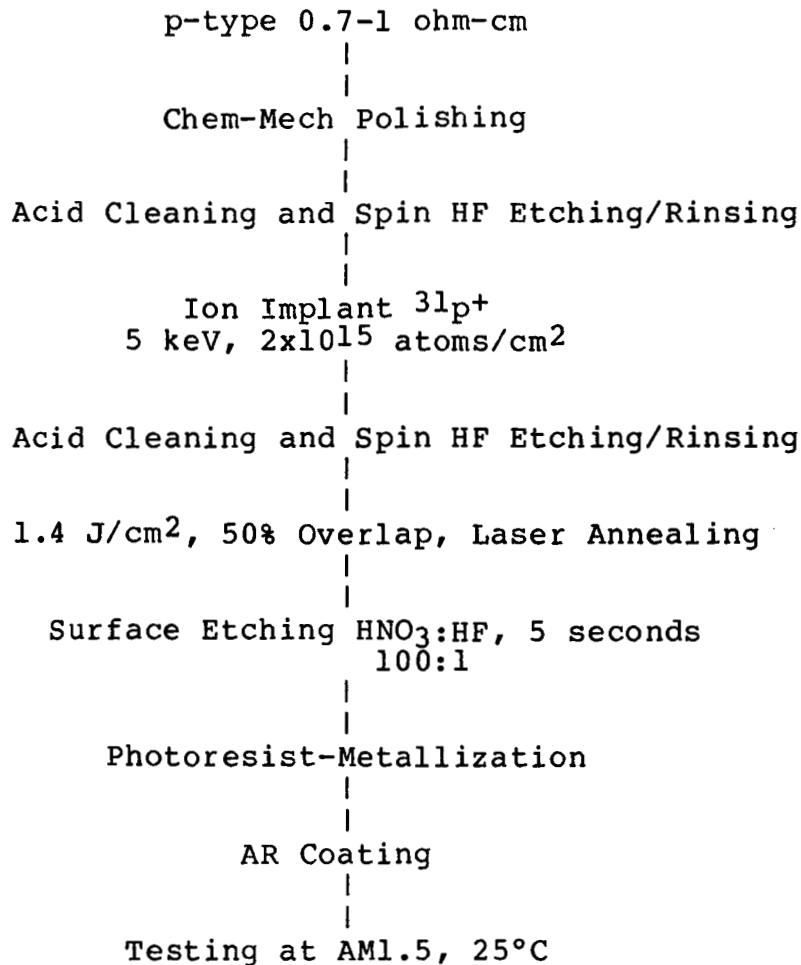


Fig. 4-18. Final processing sequence.

The last batch which contained 50 wafers (2 cm x 2 cm square) was processed as described. Peeling problems were encountered during metallization and caused the loss of most of the wafers. Wafers that passed the tape test after metallization had efficiency as high as 16%, demonstrating the fact that the process sequence is satisfactory.

#### 4.5 CELL CHARACTERIZATION (2 cm x 2 cm)

All 16 of the 2 cm x 2 cm cells survived the standard commercial metallization process. Average efficiency after AR coating was 15.4% with the highest above 16% at AM1.5. Table 4-21 summarizes the overall result. Figure 4-19a represents the best cell I-V characteristics. Average quantum efficiency (Fig. 4-19b) is superior to a companion 16% commercial space cell. The fill factor of the laser annealed sample is comparatively softer because of the shallow junction property that gives rise to higher current but is slightly shunted in fill factor.

Table 4-21. Electrical performance of the batch-processed cells.

Sample No.	$J_{sc}$ (mA/cm <sup>2</sup> )	$V_{oc}$ (V)	FF (%)	Eff (%)
<b>B61/62</b>				
#1	33.07	0.600	75.88	15.07
#2	33.20	0.600	75.92	15.12
#3	33.40	0.608	78.65	15.98
#4	33.85	0.610	77.77	16.06
#5	33.65	0.607	76.81	15.89
#6	33.80	0.608	77.87	16.01
#7	33.47	0.607	77.78	15.80
#8	33.59	0.607	76.12	15.52
#9	33.84	0.607	77.41	15.90
#10	33.88	0.605	78.09	15.54
#11	33.46	0.605	76.91	15.56
#12	33.35	0.605	77.79	15.69
#13	33.38	0.603	72.53	14.60
#14	33.15	0.607	71.96	14.47
#15	33.16	0.607	70.12	14.11
#16	32.09	0.607	75.15	15.02
<AVERAGE>	33.40	0.606	76.05	15.40

#### 4.6 LASER ASSISTED METALLIZATION

Three approaches were examined for the use of excimer lasers in the fabrication of fine line metallization. The first approach was based on laser assisted chemical vapor deposition, LCVD. In this approach, the wafer is put into a chamber containing a gas which contains a metal atom as part of its makeup, such as tungsten hexafluoride or trimethyl aluminum. A laser beam enters the chamber through a silica port aimed at the wafer surface. Two types of processes can take place. In the first, the metal containing molecules absorb the laser radiation and decompose forming the free metal which diffuses to the metal surface where it adheres. In the second process, the beam passes through the gas and hits the surface of the wafer, heating it up. Metal containing gas molecules which diffuse to the surface are then decomposed forming the free metal. In both of these LCVD processes, the local nature of the laser beam can be used to form a fine line.

The second approach examined was the use of a laser beam to reduce a coating of a metal containing organic to the metallic state. Experiments on this direct writing technique were conducted using wafers coated with silver neodecanoate. The coating was obtained by spin-on of solutions of silver neodecanoate in hexane onto silicon surfaces followed by evaporation of the xylene.

ORIGINAL PAGE IS  
OF POOR QUALITY

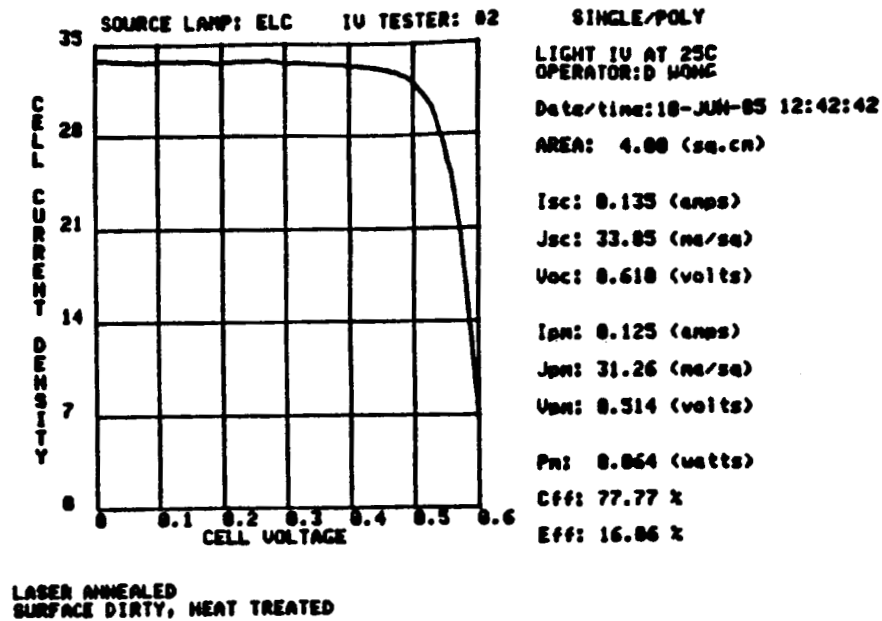


Fig. 4-19a. I-V of the best cell of the 16-cell group processed.

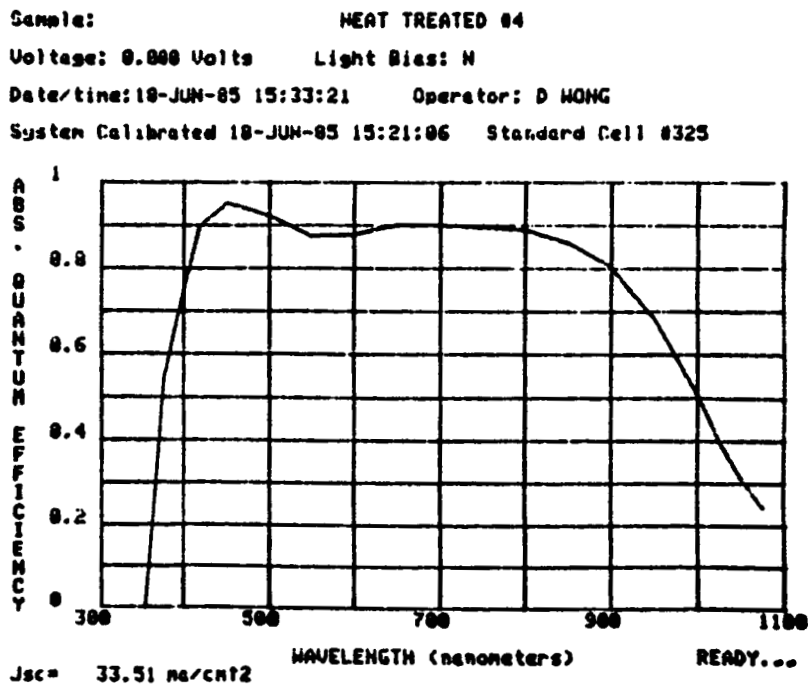


Fig. 4-19b. Quantum efficiency of the cell.



ORIGINAL PAGE IS  
OF POOR QUALITY

The third approach was to sinter previously deposited films of Ti/Pd/Ag with the laser beam causing the sintered regions to adhere preferentially to the silicon surface.

However, none of the above experiments yielded a grid pattern good enough for cell testing. The main problems were adhesion, metal purity and thickness, and deposition rate.

#### 4.6.1 Tungsten on Silicon (Batch 1) From WF<sub>6</sub> Gas

The sample from the first batch had distinct lines surrounded by a heavy white haze (Fig. 4-20). Line width ranges from 0.012" to 0.017" with height close to 1000Å (Fig. 4-21). Auger analysis was conducted on the line area (Fig. 4-22a). An AES spectrum of the deposited line area showed the surface composition to be WO<sub>2</sub> with traces of silver and ubiquitous carbon. The AES spectrum of the line area after sputter removal of about 100Å from the film revealed no tungsten metal (Fig. 4-22b). The haze area was found to be WO<sub>2</sub>, Ag, and Si. The SEM image of this area showed a flocculant-like surface deposit. Apparently the Si in the flocculant deposit came from the substrates that were sputtered by the high laser energy.

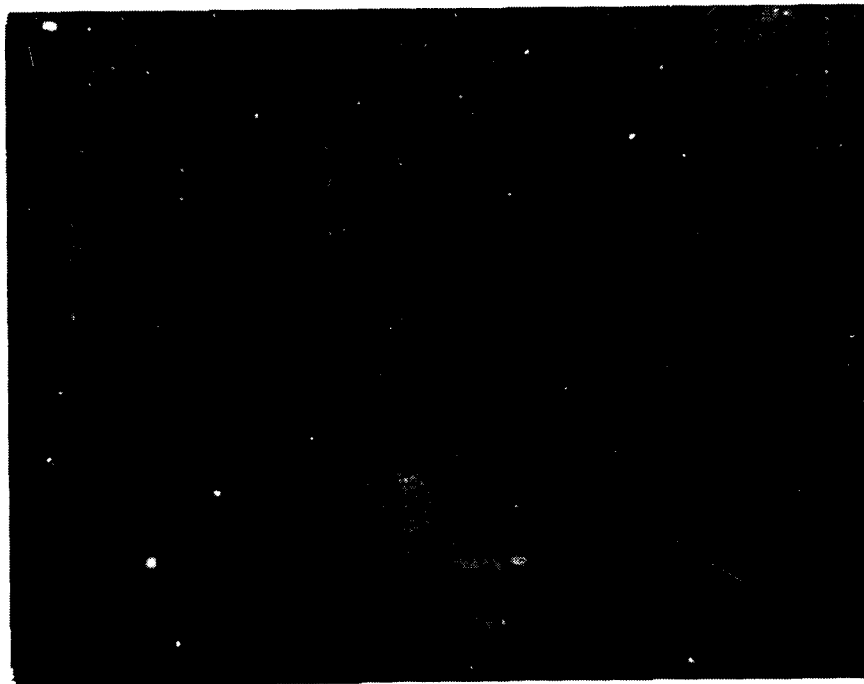
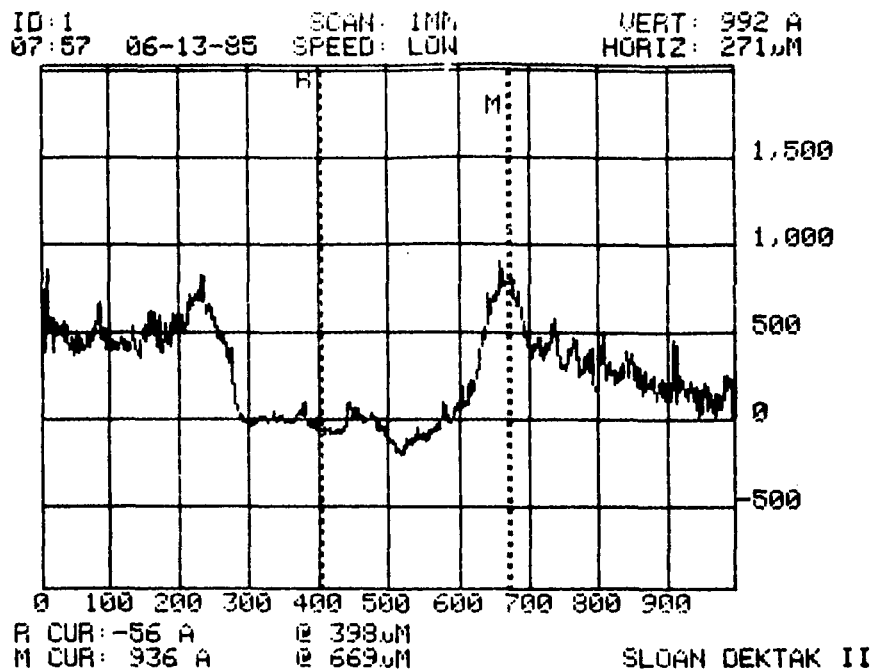


Fig. 4-20. Overall photograph of tungsten lines deposited. Note the hazy area is tungsten, tungsten oxide dust.



**Fig. 4-21.** Surface profile on tungsten lines deposited from  $WF_6$  by DEKTAK.

#### **4.6.2 Tungsten on Silicon - 250-500 Shots (Batch 2)**

Again, the deposition was found to be  $WO_2$ . No Ag was observed in this sample, leading to the conclusion that the Ag in the first sample was caused by external contamination during wafer handling.

#### **4.6.3 Aluminum on Silicon (Batch 8) from TMAL Gas**

Auger analysis of the initial sample revealed only aluminum oxide with traces of fluorine and a large quantity of carbon. After sputter removal of about  $100\text{\AA}$  from the film, elemental silicon was detected in addition to aluminum oxide. This indicates that the film deposited was fully oxidized (Fig. 4-23).

In general, no elemental metal was found in the deposited lines, whether  $WF_6$  or TMAL. The source of oxygen causing oxidation is as yet undetermined.

Experiments with various conditions as shown in Table 3-3 such as change in gas ratio, flow rate, substrate temperature, and exposure times were performed. However, no improvement on metal quality or adhesion was observed.

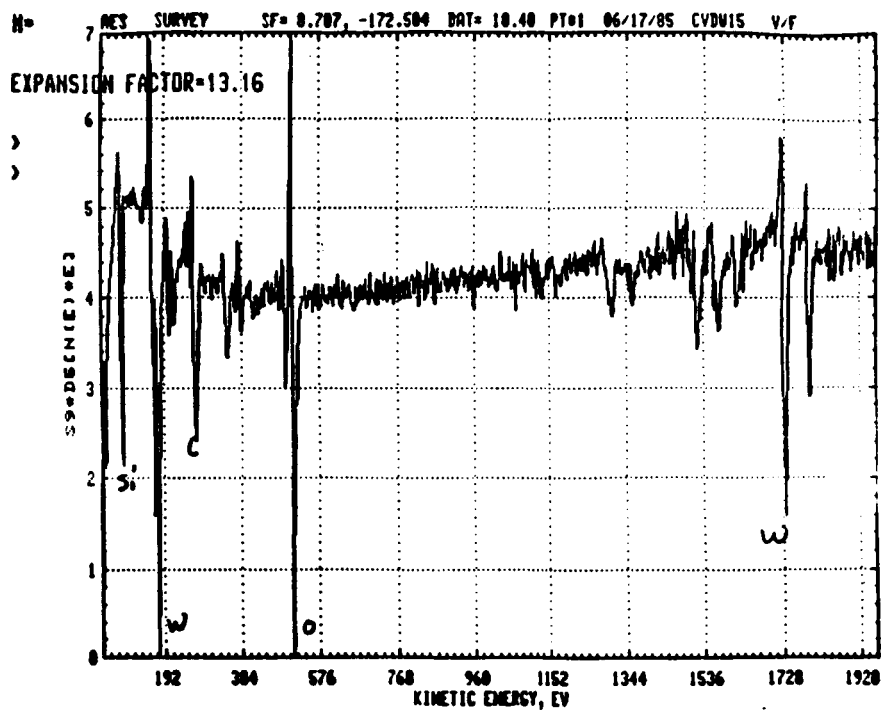


Fig. 4-22a. Auger analysis of CVD W on Si #W2LPD5.

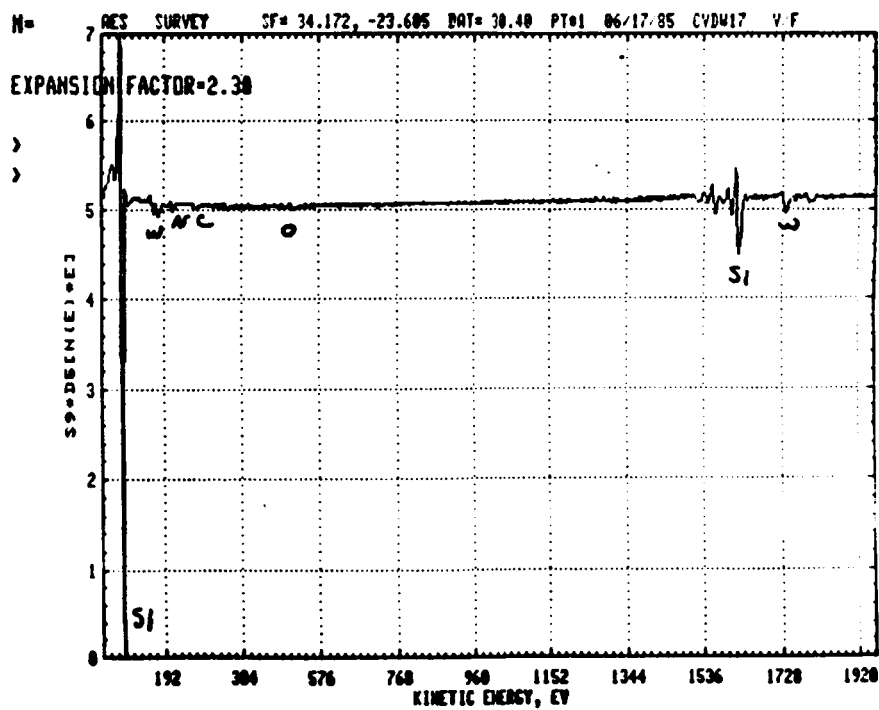


Fig. 4-22b. CVD W on Si #W2LPD5 line area after profile to ~100Å deep.

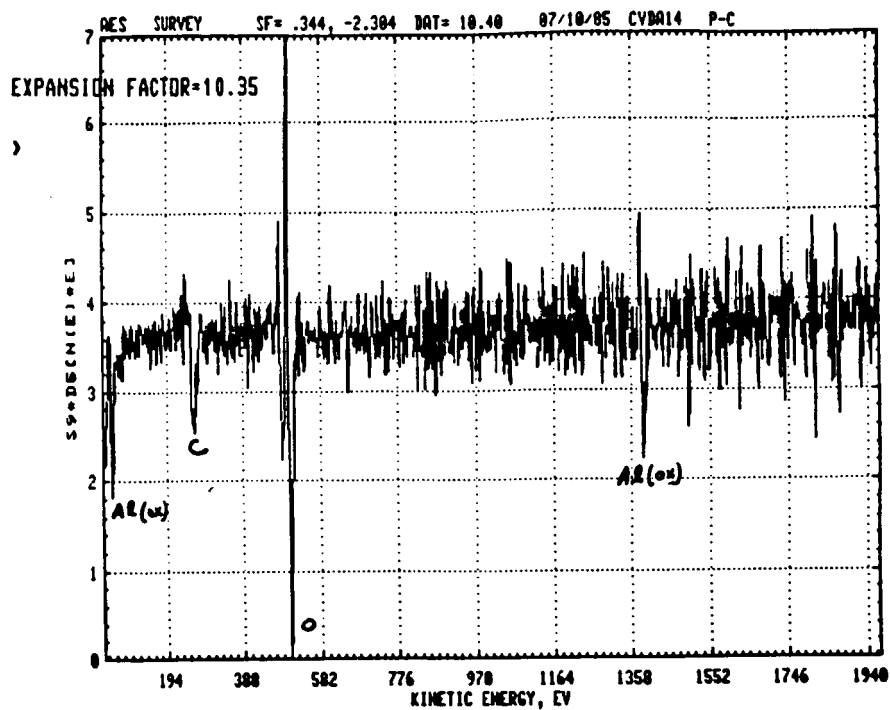


Fig. 4-23a. Laser CVD Al on Si.

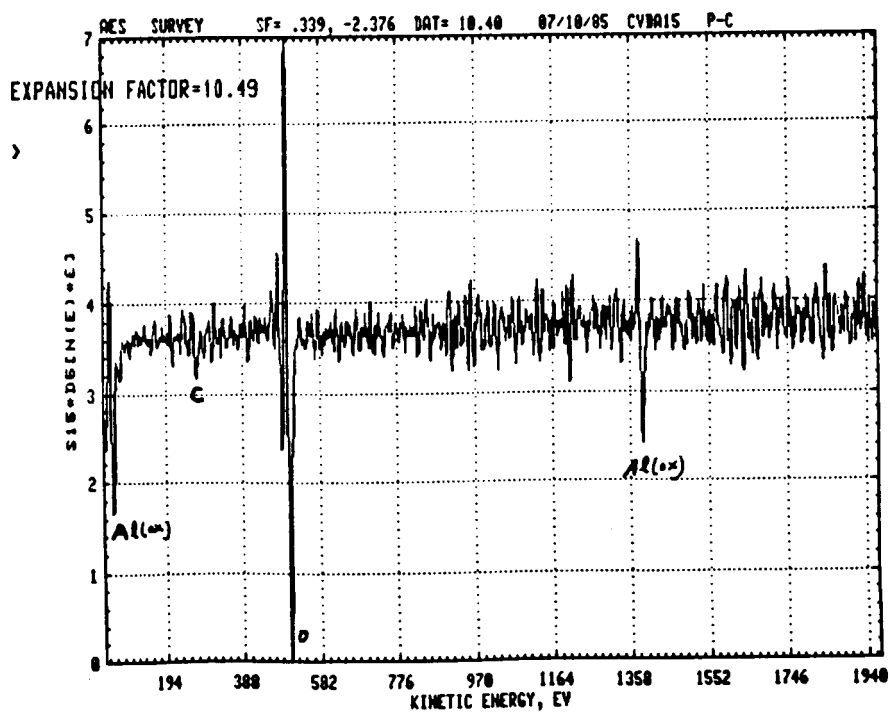


Fig. 4-23b. Laser CVD Al on Si after 100Å removed.

#### 4.6.4 Silver Neodecanoate

The solute was dissolved in xylene by the ratio of 1 gram per 100 cm<sup>3</sup>. Water content in the solution was removed by centrifugal processing. A few drops of the solution were applied to the spinning silicon wafer to produce a film about 10 microns thick. The film was then dried in the oven at 100°C for 10 to 15 minutes. Laser writing was performed in air with the laser beam sized at 0.1x12 mm. The number of pulses were 1, 10, 50, 100, and 250. (For parameter details, refer to Section 3.5.2, Table 3-2.) The grid pattern was as shown in Fig. 4-24. The ohmic bar is composed of multiple shots of lines overlapping each other to the width of 0.040". Figure 4-25 shows the remains of the pattern after dissolving the film in xylene. A close examination of the lines revealed a very small amount of metal on the surface where directly laser exposed, especially at the center of the beam. At the ends of the beam where laser intensity decreased sharply, traces of metal film were observable. This suggests that the laser energy used was too great.

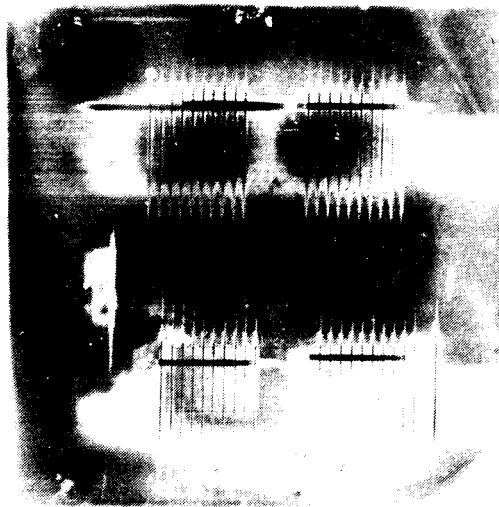


Fig. 4-24. Grid pattern for silver neodecanoate metallization.



Fig. 4-25. Remains of pattern after dissolving film.

#### 4.6.5 Direct Writing onto Ti-Pd-Ag Film

An experiment to sinter gridlines onto silicon by direct writing onto evaporated Ti-Pd-Ag film was also attempted, but without success. Preferential removal of Ti metal from the silicon leaving only the laser written gridline was found to be very difficult.

#### 4.7 SURFACE PASSIVATION

The last subject to be investigated was surface passivation by photodeposition of  $\text{SiO}_2$  onto processed silicon solar cells. A passivated surface would have lower surface recombination velocity for lower dark current,  $J_0$ , that would contribute to higher  $V_{oc}$ .

The concept of passivation by oxide deposition (instead of thermally grown  $\text{SiO}_2$ ) was first tested by sputtering oxide. 100Å oxide was sputtered onto four solar cells. Measurements before and after deposition as well as at 500°C annealing temperature are summarized in Table 4-22.

Results were so sporadic that no conclusion could be drawn. Slight  $V_{oc}$  improvement was noted in cell  $C_1$  to  $C_3$ . But  $C_4$  obviously was degraded for unknown reasons, either from stress or by a damaged surface, due to excessive handling.

Table 4-22. Results of passivation by sputtered oxide.

Sample No.	$J_{sc}$ (mA/cm <sup>2</sup> )	$V_{oc}$ (V)	FF (%)	Eff (%)
CzDWC <sub>1</sub>	20.10	0.574	76.75	8.85
+100°C $\text{SiO}_2$	20.51	0.564	75.66	8.75
+500°C	21.15	0.582	72.70	8.95
CzDWC <sub>2</sub>	20.17	0.574	78.06	9.04
+100°C	19.63	0.589	76.35	8.83
+500°C	19.65	0.591	77.00	8.94
CzDWC <sub>3</sub>	19.34	0.581	68.11	7.65
+100°C	19.62	0.586	70.49	8.11
+500°C	19.67	0.588	71.66	8.29
CzDWC <sub>4</sub>	19.33	0.589	78.42	8.92
+100°C	20.42	0.574	76.80	9.01
+500°C	20.76	0.579	75.36	9.06

Several experiments in laser deposition of  $\text{SiO}_2$  followed. The laser beam was perpendicular to the cell surface.

In the first experiment, oxide was deposited onto a bare silicon surface with 1000 and 2000 shots respectively. Spots of brownish color were observable. Adhesion was excellent. AES analysis indicated  $\text{SiO}_2$  compound with less than 6% of nitrogen (Fig. 4-26) and AES profile suggested that the oxide thickness was about 150Å (Fig. 4-27).

Three actual depositions followed thereafter onto finished solar cells. In the first experiment (B22), the sample was a laser annealed cell, B61RW, the laser energy at about 20 mJ/cm<sup>2</sup>. It took 45 spots to cover the whole area at 50% overlap. Each spot had 1500 shots of exposure. Figure 4-28 shows the I-V curves before and after passivation. While the dark I-V remained practically unchanged, the  $J_{sc}$  had an increment of 1.5 mA/cm<sup>2</sup> deposited oxide that enhanced the current due to increase in optical coupling. An actual passivation effect was not detectable.

The next experiment involved four solar cells. Laser parameters were similar to those in the previous experiment. The substrates were heated to 90°C during deposition. A faint brownish film was observable on the front surface. Ellipsometric measurements indicated that the film thickness was about 200 nm. Again, only optical enhancement was observed as indicated by the I-V measurement summarized in Table 4-23.

The last experiment in the passivation study was performed at an elevated temperature, different laser energy density, and various exposure pulses. The deposition parameters and electrical results for the three cells used in the experiment are given in Table 4-24.

In this experiment, the  $J_{sc}$  is only slightly improved both in 20 mJ, 1000 shots, and 50 mJ, 100 shots. The  $V_{oc}$ , on the other hand, shows an increase of a few mV in all samples. There is not much difference in increasing the energy density while decreasing the exposure pulses. In comparing with the previous experiment, it seems that deposition at elevated temperatures would cause some improvements in  $V_{oc}$ . Dark I-V measurement did not show improvement in  $J_{01}$  and  $J_{02}$ , but the dark reverse current was found to be lowered.

At this stage, there is no conclusive evidence to show whether laser assisted CVD  $\text{SiO}_2$  onto silicon solar cells will or will not passivate the surface states, similar to the experiment of sputtered  $\text{SiO}_2$ . However, considering the activation energy provided by laser, the LCVD appeared to be preferable when passivating the surfaces. The subject is definitely too immature to be abandoned at this stage. Experiments such as increased laser energy, substrate temperature, and post deposition annealing could be performed.

ORIGINAL PAGE IS  
OF POOR QUALITY

Laser CVD SiO<sub>2</sub> on Si  
From SiH<sub>4</sub> and N<sub>2</sub>O, 15A Ramped  
WILPD 19A 17000 Shots

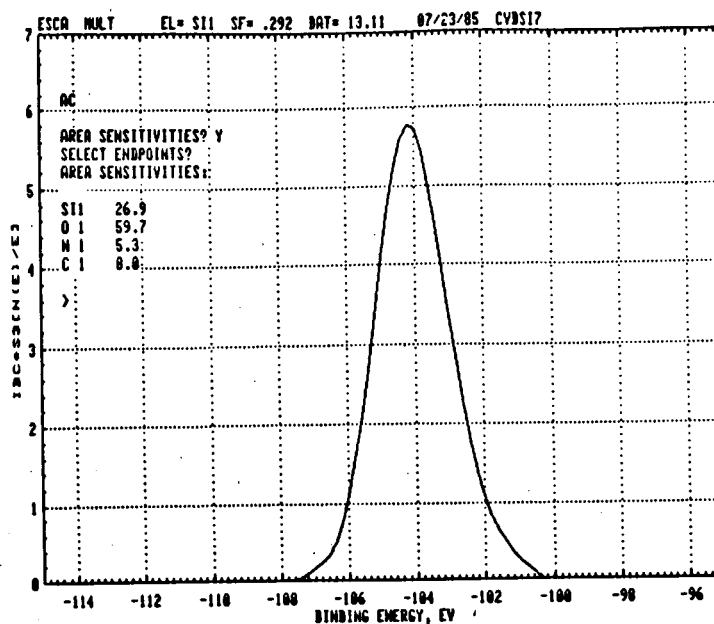


Fig. 4-26. AES analysis indicating SiO<sub>2</sub> compound has less than 6% nitrogen.

Laser CVD SiO<sub>2</sub> on Si  
WILPD 19A, 2000 Shots  
4x4mm ALT (~10A/min)

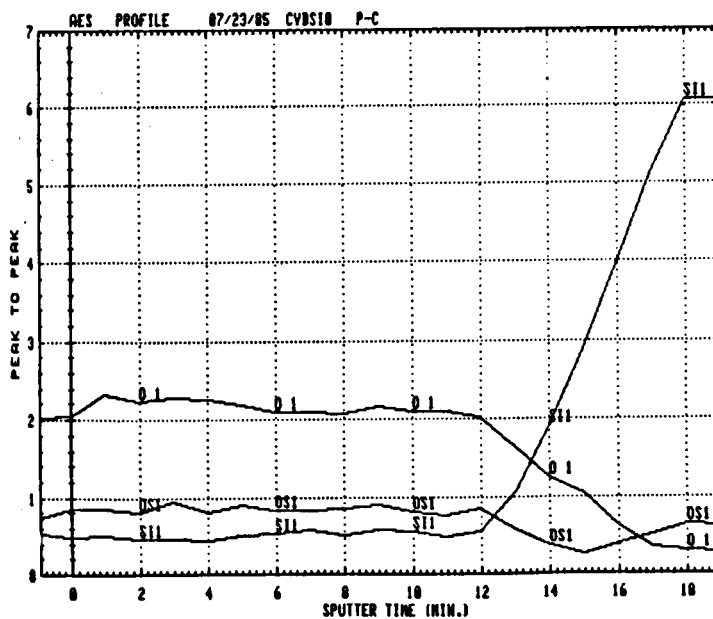
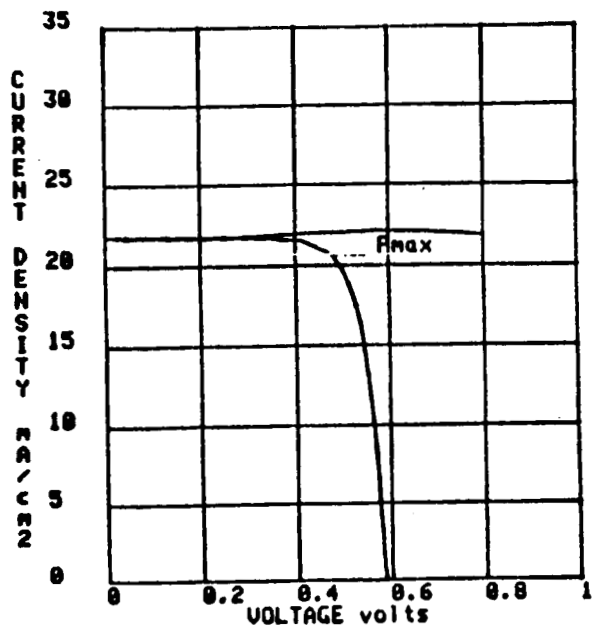


Fig. 4-27. AES profile suggesting oxide thickness about 150Å.

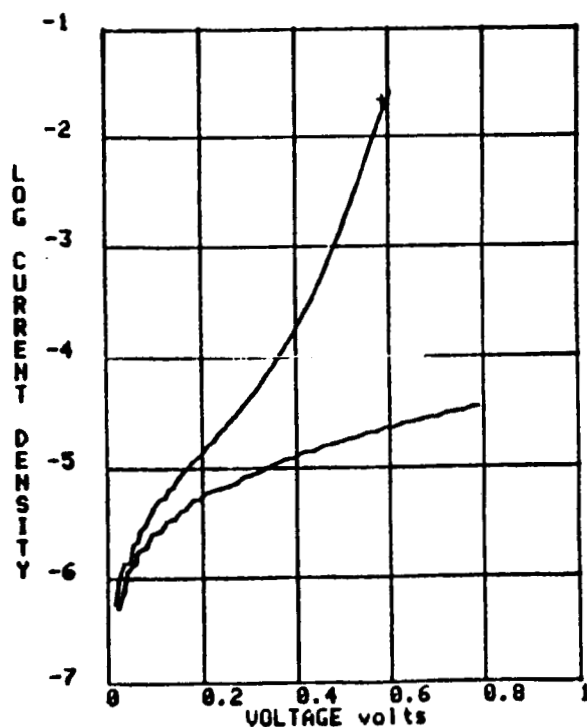


XT - 10 LIGHT I-V DATA 19-JUL-85 14:53:04  
 -Company Confidential-  
 Sample: B61RW Cell Number: 1② Area (cm<sup>2</sup>): 4  
 Operator: SCM Insolation (mW/cm<sup>2</sup>): 100 Cell Temp (C): 25.1  
 NO A/R, SINTERED 800C, RETEST



Jsc : 21.762 ma/cm2  
 Voc : 0.585 volts  
 Jpn : 20.676 ma/cm2  
 Upn : 0.478 volts  
 Pdm : 9.892 mw/cm2  
 FF : 77.7 %  
 Eff : 9.89 %  
 dU/dJ  
 @Voc : 1.55 ohm-cm2  
 Cor.C: 1.000  
 dJ/dU  
 @Jsc : 0.49 mS/cm2  
 Cor.C: 0.760

a. Light I-V



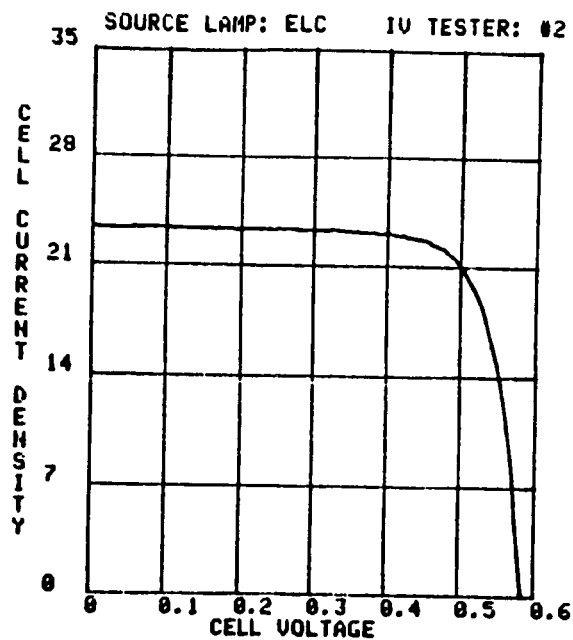
KEPCO/DARK  
 -COMPANY CONFIDENTIAL-

DARK IV AT 25.1 C  
 19-JUL-85 14:53:40  
 Operator: SCM  
 Sample: B61RW③  
 NO A/R  
 SINTERED 800C  
 RETEST

CELL : 1  
 Area(cm2): 4.00  
 Gsh(nho): 2.07E-004  
 ± 4.33E-006  
 gsh(nho/sq.cm): 5.18E-005  
 Rsr(ohm): 1.22E-001  
 rsr(ohm-sq.cm): 4.88E-001

b. Dark I-V

Fig. 4-28a and b. I-V curves before passivation.



SINGLE/POLY  
LIGHT IV AT 25C  
OPERATOR: DW  
CELL: B61RWSP  
Date/time: 25-JUL-85 13:09:15

AREA: 4.00 (sq.cm)

Isc: 0.094 (amps)

Jsc: 23.39 (ma/sq)

Voc: 0.585 (volts)

Ipm: 0.086 (amps)

Jpm: 21.60 (ma/sq)

Upm: 0.490 (volts)

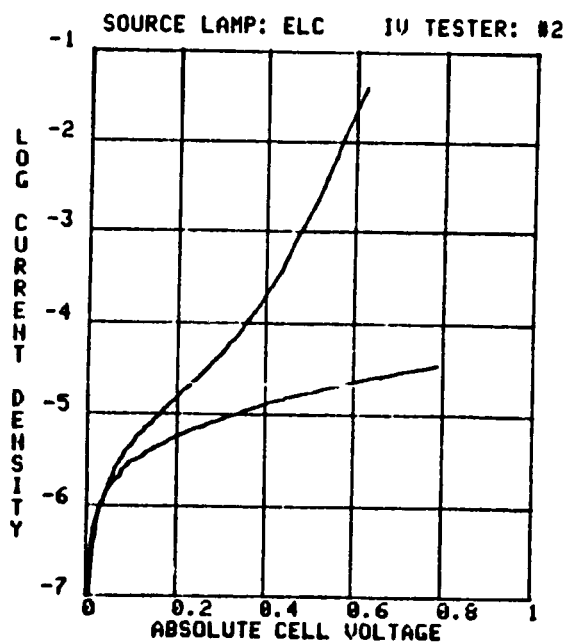
Pm: 0.042 (watts)

Cff: 77.33 %

Eff: 10.58 %

c. Light I-V

ORIGINAL 9.9%  
SURFACE PASS. 56 MJ/500 SHOT  
WILPD24



SINGLE/POLY  
DARK IV AT 25C  
Date/time: 25-JUL-85 13:10:44

OPERATOR: DW

CELL: B61RWSP

AREA: 4.00 (sq.cm)

Gsh: 1.59E-004 (rho)

$\pm$  1.54E-006

gsh: 3.99E-005 (rho/sq.cm)

d. Dark I-V

ORIGINAL 9.9%  
SURFACE PASS. 56 MJ/500 SHOT  
WILPD24

Fig. 4-28c and d. I-V curves after passivation.

**Table 4-23.** Electrical measurements of SiO<sub>2</sub> passivated cells. Energy density 20 mJ at 500 pulses. Substrates heated to 90°C.

Cell ID (R63)	J <sub>sc</sub> (mA/cm <sup>2</sup> )	V <sub>oc</sub> (V)	FF (%)	Eff (%)
RW #1	22.03	0.578	79	10.1
Passivated	25.97	0.583	78	11.8
RW #2	22.38	0.580	77	10.0
Passivated	26.36	0.583	75	11.6
RW #3	22.46	0.575	78	10.1
Passivated	23.84	0.576	76	10.5
RW #4	22.45	0.580	77	10.1
Passivated	24.10	0.576	71	9.9

**Table 4-24.** Deposition parameters and electrical results for cells passivated at higher temperatures.

Cell ID	Energy Density (mJ)	Pulses	Temp (°)	J <sub>sc</sub> (mA/cm <sup>2</sup> )	V <sub>oc</sub> (V)	FF (%)	Eff (%)
(A)							
B44R59I#1	--	--	--	21.73	0.587	78.8	10.1
SiO <sub>2</sub> coated	20	1000	180	23.00	0.593	77.7	10.6
(B)							
B44R59I#2	--	--	--	21.87	0.588	78.2	10.1
SiO <sub>2</sub> coated	50	100	180	22.61	0.590	77.8	10.4
(C)							
B44R59I#3	--	--	--	21.73	0.589	77.6	9.9
SiO <sub>2</sub> coated	50	100	180	22.82	0.593	77.7	10.5

## SECTION 5.0 DISCUSSION

While laser annealing is a true "cold" process that should not degrade bulk minority lifetime and is capable of producing high efficiency solar cells, it has many technical disadvantages in comparison with conventional thermal diffusion.

One disadvantage is that textured surfaces were found not suitable for the laser junction forming process because of difficulties in controlling the degree of surface melting. AR coatings must be employed in production for light absorption enhancement.

Another problem is that the process is extremely sensitive to surface conditions because the diffusion in laser annealing is carried out in the liquid state. Any scratches or defects on the surface are modified during the recrystallization. Surface defects/contamination increase the surface/bulk recombination rate which in turn decreases  $V_{oc}$ .

Ion implantation is a well-developed technology for integrated circuit processing, and is especially useful for fabricating deeply buried junctions. However, in the fabrication of solar cells, the implanted layer must be shallow with sufficiently high surface concentration. Solar cell junction formation requires low keV ( $\leq 3$  keV) with high ion fluence, while 5 keV is the lowest available through commercial services or equipment. Even at such low kinetic energy implantation, deep lattice damage unremovable by  $1.5 \text{ J/cm}^2$  laser energy density has been demonstrated in this phase of the project. Increasing the laser energy density for deeper melting might remove deep deposition damage defects, but heavy surface damage also takes place.

Metallization by dissociating metallic gas with the excimer laser was intended to provide sharp, well-defined metal gridlines for efficient current collection. Problems encountered: purity of deposited metal, adhesion, and the impractically slow deposition rate.

Surface passivation by LCVD of  $\text{SiO}_2$  has not shown effective results in electrically passivating the surface states; however, adhesion is excellent.

The individual topics are discussed below in more detail.

### 5.1 JUNCTION FORMATION

Through the experimental results obtained, it has been proven that laser annealing on Cz silicon can produce high efficiency solar cells comparable to commercially available space cells (Fig. 5-1a, b, c, and d). The concept of steeper and shallower

junctions obtainable in laser annealed cells than thermally diffused cells has also been demonstrated by comparing the quantum efficiency of the two. The better red response in the latter is due to higher base resistivity with the presence of a back surface field (BSF) while the former is a planar  $n^+p$  device with lower base resistivity. Higher  $V_{oc}$  should be obtainable if the laser were more uniform and required no kaleidoscope for shaping the beam spot which is believed to cause edge damage. However, it was also found that laser annealing is not yet an economic process for large volume cell fabrication. The tight requirement of flawless chemical-mechanically polished surfaces instead of textured surfaces, ion implant as the sole doping process, together with the additional AR coating required, elevates the cost far above the present thermal diffusion process. The use of production grade Cz material for the fabrication of high quality cells has been shown.

## 5.2 LASER ASSISTED METALLIZATION

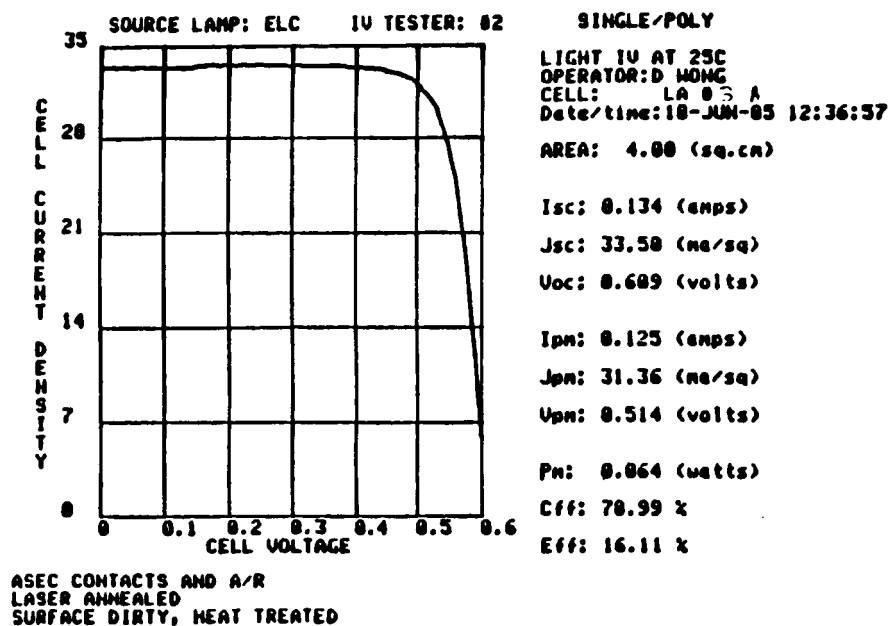
Despite the extensive research which has been carried out during the past five years on the use of UV lasers for photodeposition of thin metal film having high spatial resolution, such a technique has never been applied to solar cell fabrication in gridline deposition. In this program we tried to deposit metal gridlines by gas phase photodeposition of alkyl and fluoride metal. The first technical difficulty encountered was to obtain pure metal. Instead, only metallic oxide was obtained. Such metallic oxide did not adhere to the surface, and was also poor in conductivity. Above all, the deposition rate, whether of oxide or pure metal, was found far too slow a process. In our experiment, the maximum rate obtained was about  $600^\circ\text{A}$  per minute (500 pulses at 5 Hz).

Spatial resolution is another problem. As soon as the laser enters the gas cell, and photodeposition of the metal gas is initiated, flakes of metal (or metal oxide) start to fall onto the silicon surface at a solid angle of the incident beam. The line width becomes diffused an order of magnitude larger than the beam size. The more effective method for metallization could be the LCVD technique, in which a longer wavelength laser is used such as argon or  $\text{CO}_2$  that is less absorptive to the metal gas.<sup>6</sup> Chemical vapor deposition (CVD) starts primarily at the silicon surface which is heated by the laser. Thus the line definition is much sharper and would have no metallic flakes deposited.

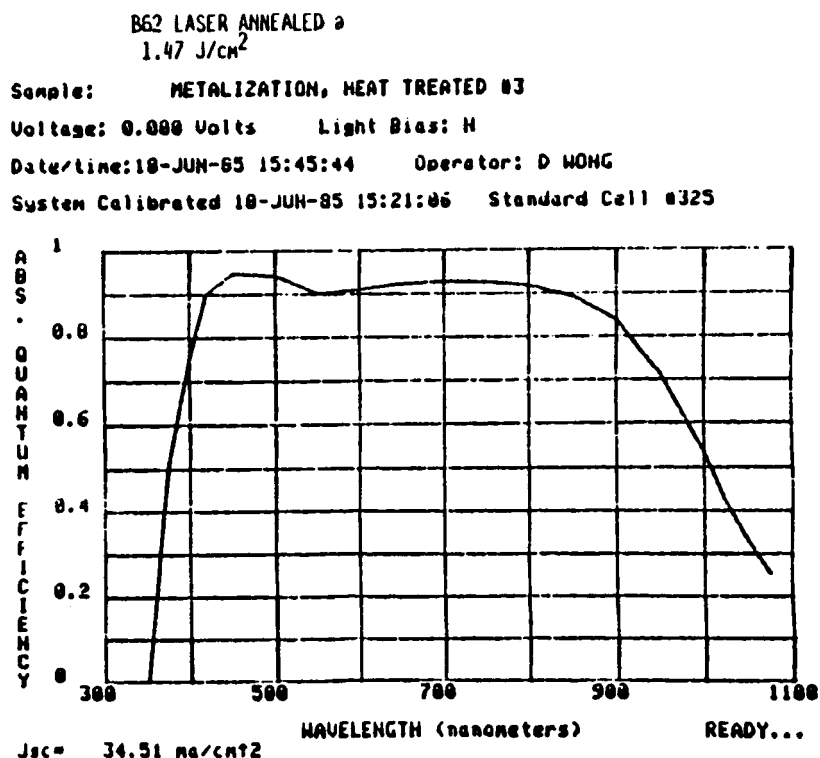
## 5.3 SURFACE PASSIVATION - LCVD $\text{SiO}_2$

Before the experimental work was initiated, major concerns about LCVD  $\text{SiO}_2$  deposition were adhesion, deposition rate, and effect in passivating the surface states to improve  $V_{oc}$ . In the limited experiments conducted, it was found that  $\text{SiO}_2$  deposited had excellent adhesion. The deposition rate was acceptable.

ORIGINAL PAGE IS  
OF POOR QUALITY



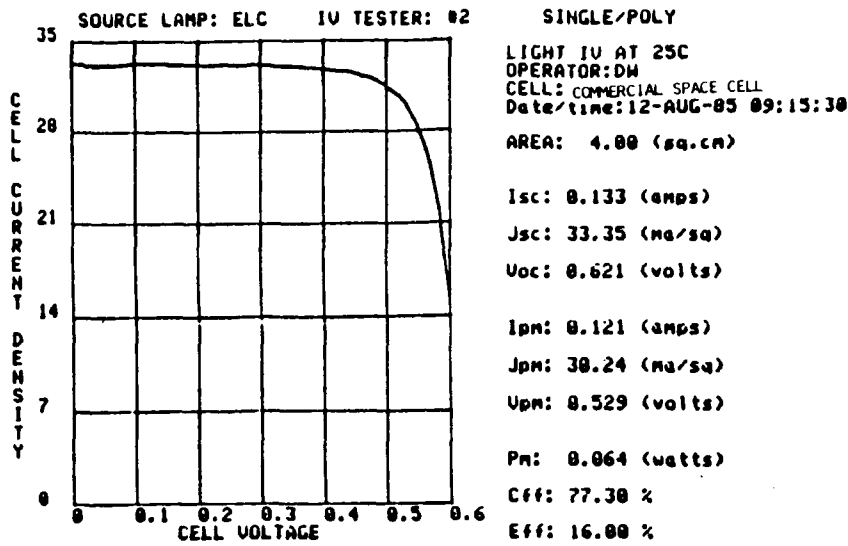
a. Light I-V of Cz cell.



b. Quantum efficiency of Cz cell.

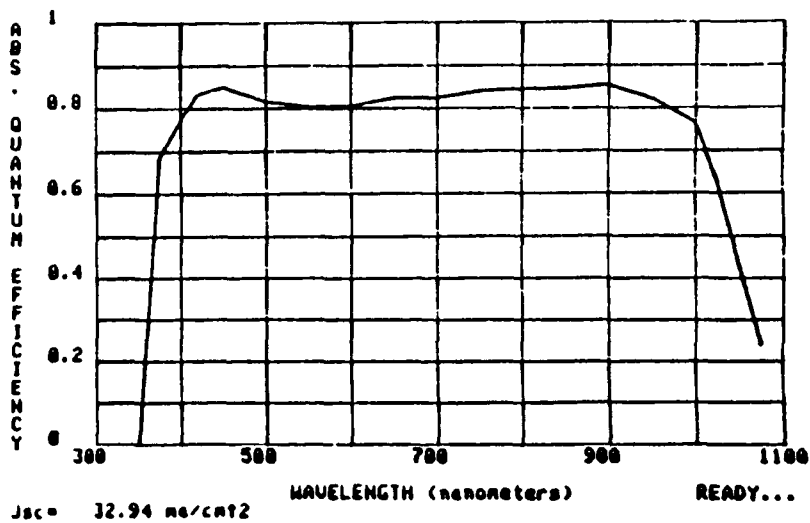
Fig. 5-1. Best efficiency of laser annealed cell and comparison with space cell.

ORIGINAL PAGE IS  
OF POOR QUALITY



c. Light I-V of commercial space cell.

Sample: COMMERCIAL SPACE CELL, 16% @ AL5  
Voltage: 0.000 Volts Light Bias: N  
Date/time: 02-NOV-84 12:59:22 Operator: DM  
System Calibrated 22-OCT-84 16:49:43 Standard Cell #325



d. Quantum efficiency of commercial space cell.

Fig. 5-1. Best efficiency of laser annealed cell and comparison with space cell

The film was also purely composed of  $\text{SiO}_2$  with only 5% detectable nitride. Processed cells, however, did not show passivation effects. Dark  $J_0$  was not changed, at least in these experiments. The improved  $J_{sc}$  is due to the AR effect of  $\text{SiO}_2$ . The main reason for ineffective passivation could be the lack of sufficient activation energy to deactivate the surface states by physically sharing the loose bonds on the surface. This could be investigated by varying the laser energy density incorporation with substrate temperature or post deposition low temperature annealing for stress relief.



## SECTION 6.0 ECONOMIC ANALYSIS

The intention of this project was to adapt pulsed excimer laser processing technology to fabricate cost-effective solar cells. The underlying assumptions in carrying out the project were as follows: that excimer laser processing steps in junction formation, metallization, and surface passivation could provide a cell performance benefit over more traditional processes; that the rates of carrying out the processes would be consistent with scaling the processes up to factory levels; that increased equipment and material costs would be compensated for by increase in cell performance; and that commercially available equipment would be available to carry out the development work in the project. Based on the realization of these assumptions, an economic analysis would then show the advantage of implementing the proposed processes.

Under the above assumptions, then, a processing sequence was proposed based on the use of Czochralski-grown material of appropriate resistivity that would demonstrate the project objective. This process sequence is shown in Fig. 6-1. It incorporates the use of an excimer laser to form and anneal a junction latently deposited using ion implantation technology. This process step was to be followed by a LCVD, high density fine-line metallization step to capitalize on the shallow junction formed. The LCVD step was proposed to be carried out using an UV excimer laser to cause photo-decomposition of a metallo-organic gas. Finally a passivation layer of silicon dioxide on the surface was to be fabricated using laser assisted photo-decomposition of silane and nitrous oxide.

The results of the work conducted in this project which are relative to the cost-effectiveness goals are as follows:

- Excimer laser junction formation on Czochralski silicon yields cells which are as good as the best cells made using diffusion furnace processing and high quality evaporated, fine-line evaporated contacts, but apparently no better.
- The ion implant process required for the best layer annealed cells requires fluences of  $3.0 \times 10^{15}/\text{cm}^2$  with commercially available machines to carry out this type of implantation. Future work in the semiconductor field seems to require higher energies rather than lower energies.
- The degree of surface cleanliness and lack of damage required for wafers before laser annealing is substantially higher than that required for thermal diffusion processing. Thus, costly surface preparation steps are required after implantation in order to obtain results comparable to those obtained with thermal diffusion.

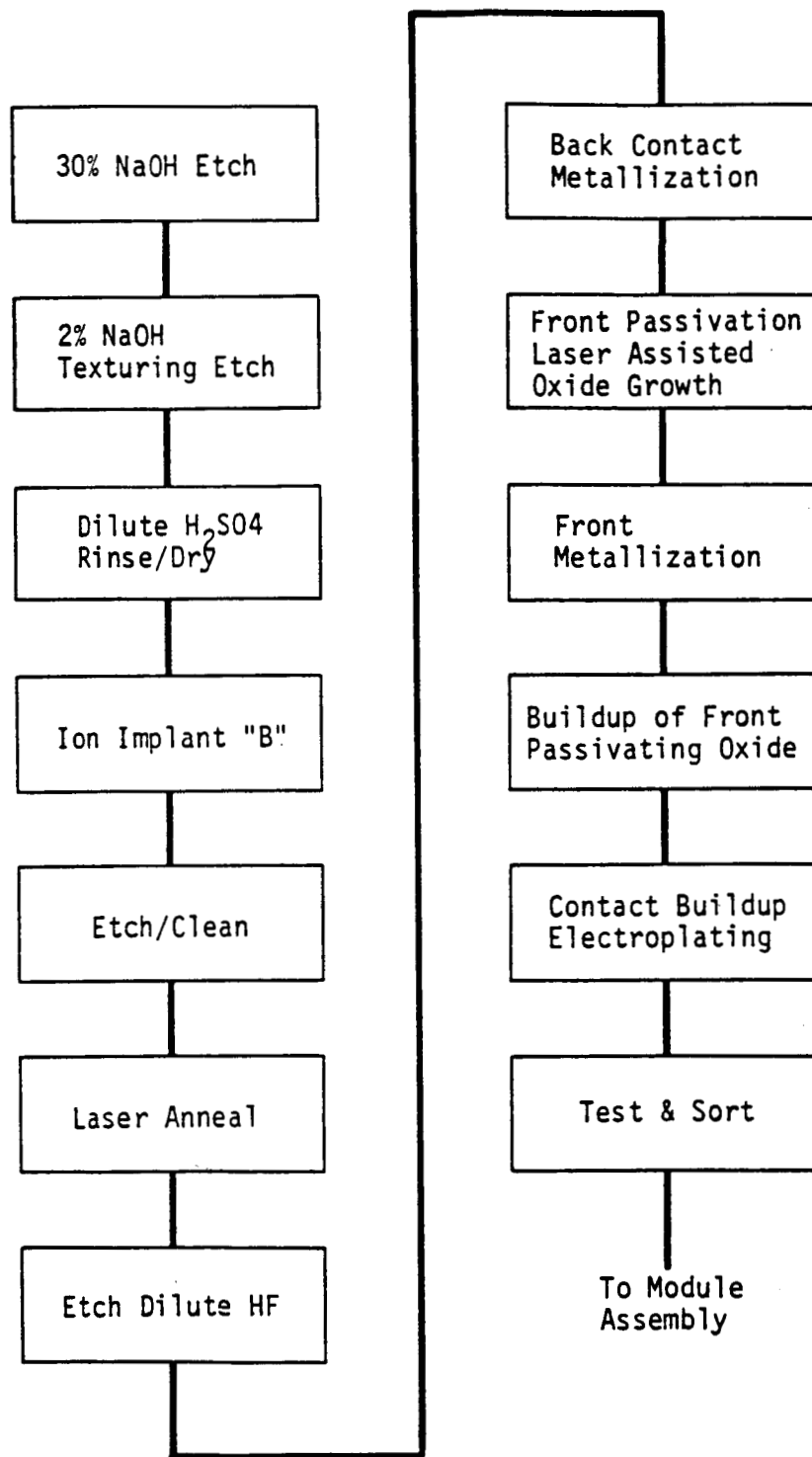


**Fig. 6-1.** Proposed Excimer Laser Process.  
n type (phosphorus doped) 0.3 ohm-cm Cz silicon.

- No practical, low cost processes for deposition of fine-line collection grids are available, including those based on excimer laser technology. In order to make use of the shallow junction fabricated in the excimer laser annealing process, a high density, (>25 lines/inch), grid is required. The low rates of deposition for LCVD lines preclude their use in large area applications.
- No surface passivation effects were observed using LCVD silica deposition techniques, which precludes the use of this process in solar cell manufacture.

Based on these considerations, it is clear that the assumptions underlying the goal of adapting excimer laser processing to the fabrication of cost-effective solar cells are not met in practice.

It has been considered useful to carry out an analysis of the comparison of the junction formation step between the thermal diffusion process and the ion implant/excimer laser annealing process. The JPL developed IPEG analysis tool has been used here to carry out this comparison. The process steps for the comparison methods are shown in Fig. 6-2.

**Thermal Diffusion  
Junction Process  
Baseline**

---

POCl<sub>3</sub> Diffuse  
Plasma Etch

**Excimer Laser  
Junction Process**

---

Ion Implant  
H<sub>2</sub>O<sub>2</sub>:H<sub>2</sub>SO<sub>4</sub> Etch  
Laser Anneal  
10:1 Clean

**Fig. 6-2.** Comparison of junction formation processes:  
thermal diffusion vs  
ion implant/excimer laser annealing.

Tables 6-1 and 6-2 show a summary of the IPEG cost comparison for the two processes based on data discussed below. The baseline process is assumed to yield an average of 13% cells, while the excimer laser junction formation process is assumed to yield cells at 17%. This efficiency assumption is based on the use of fine-line metallization and surface passivation processes, which are not expected to be available in an economic form in the foreseeable future. The difference in the cost of these two processes is, then, unfavorable on the order of \$0.16/watt as evaluated by the IPEG analysis method.

Table 6-1. Baseline Thermal Diffusion IPEG Cost Summary.

Process Step	EQPT	FT2	DLAB	MATLS	UTIL	IPEG EST \$/Mpk	EST YIELD	Remarks
POC13 DIFFUSE	JPL IPEG JUNCTION DIFFUSION PROCESS					0.040	0.988	ASSUME JPL SAMPLE SEQUENCE
PLASMA ETCH	180000	300	27000	92800	30000	0.069	0.980	
						0.109		

Table 6-2. Excimer Laser Annealing IPEG Cost Summary.

Process Step	EQPT	FT2	DLAB	MATLS	UTIL	IPEG EST \$/Mpk	EST YIELD	Remarks
ION IMPLANT	330000	50	35900	35980	1326	0.063	0.998	BASED ON VENDOR DATA
H2O2:H2SO4 ETCH	74000	240	24100	48000	2500	0.037	0.990	
LASER ANNEAL	272160	540	68120	330808	2700	0.152	0.995	
10:1 HF CLEAN	30000	200	19280	9000	1000	0.019	0.995	
						0.270		

## DISCUSSION OF COST ANALYSIS

### IPEG Analysis of Cost Elements

#### a. General

Each IPEG cost element is discussed below on a process-by-process basis. The following assumptions, consistent with IPEG procedures, were used throughout the analysis:

1. Equipment Capital Costs (EQPT) include installation and first year's major component spares, reduced by salvage and removal value.
2. Equipment has a 7 year life and uses straight-line depreciation.
3. Facility Area (FT<sup>2</sup>) includes equipment footprint area and required working space for normal operation.
4. Direct Labor (DLAB) includes, as applicable, factory manufacturing and maintenance personnel at the following hourly direct rates (excluding fringes):

Technician/Operator - \$ 6

Senior Processor - \$ 8

Maintenance - \$10

Process Engineer - \$12

5. Direct Material Costs (MATLS) are based on best estimates from actual laser operating experience and include scheduled maintenance materials.
6. Utility Cost (UTIL) is based on \$.075/kWh rate. KWh demand is calculated on basis of operation for estimated equipment availability factor of 0.85.
7. The factory is sized for 5 megawatts.
8. The following values were used for the IPEG coefficients:

C<sub>1</sub> = 0.59 for annual equipment cost (EQPT)

C<sub>2</sub> = 1.36 for annual factory area cost (FT<sup>2</sup>)

C<sub>3</sub> = 2.02 for annual direct labor cost (DLAB)

C<sub>4</sub> = 1.17 for annual material cost (MATS)

C<sub>5</sub> = 1.17 for annual utilities cost (UTIL),

to be used in the final cost equation:

$$\text{Final Cost} = \frac{C_1 \times \text{EQPT} + C_2 \times \text{FT}^2 + C_3 \times \text{DLAB} + C_4 \times \text{MATS} + C_5 \times \text{UTIL}}{\text{Annual Quantity}}$$

This final cost applies for comparison of a process or process group alternatives. The coefficients are based on values found in previous JPL work.<sup>7</sup>

**b. Laser Annealing**

1. EQPT - Process rates require six operating XeCl lasers with one additional spare unit in retrofit. The facility will be split into three operating groups, each with a dedicated microprocessor. Controlling laser operating parameters and a wafer positioning N/C table which provides accurate pulse pattern overlap. A single excimer gas reprocessor will serve all three groups from a common gas bottle bay. Wafer transportation is assumed to be cassette-to-cassette.

7 EXC-2 XeCl lasers @ \$25,000	\$ 175,000
6 precision N/C tables @ \$10,000	60,000
3 microprocessors @ \$3,000	9,000
1 gas reprocessor @ \$10,000	10,000
1 K-bottle/manifold bank @ \$2,000	2,000
3 wafer transport systems @ \$2,000	15,000
Installation - 2 man-months	8,160
Less salvage @ 1,000/laser	(7,000)
EQPT TOTAL =	\$ 272,160

2. FT2 - Approximate area for three side-by-side pairs of lasers, and above equipment is:

$$\text{FT}^2 \text{ total} = 18' \times 30' = 540 \text{ FT}^2$$

3. DLAB - The laser anneal facility is operated on two shifts by two technicians. All scheduled/routine maintenance is performed by skilled electro-mechanical maintenance technicians:

Operation, \$8,320/yr @ \$6 =	\$ 49,920
Maintenance, \$1,820/yr @ \$10 =	18,200
DLAB TOTAL =	\$ 68,120

4. MATLS - Principal direct costs are the replacement parts for the laser systems. Gas consumption assumes that the gas reprocessor can achieve a 20:1 extension of gas life over current art:

o Gas consumption, annual	\$ 520
o Thyatron replacement @ 6 week intervals: 7 lasers x 8.7/yr @ \$2,200	135,198
o Weekly part refurbish 3/month cost of \$417/laser (6)	90,090
o Part replacement monthly @ cost of \$1,250/laser	105,000
<hr/>	
MATLS TOTAL =	\$330,808

5. UTIL - Estimated electric demand for the laser anneal facility includes cell transport and location at 1 kW; control electronics at .2 kW; and the largest user thyatron heaters for each laser at 1.5 kW:

Annual kWh	\$ 35,986
Rate	x .075
<hr/>	
UTIL TOTAL =	\$ 2,700

#### Cost Elements of Excimer Laser Junction Formation Applications

##### a. Equipment Costs

The initial cost of present commercial excimer lasers ranges from \$10-15K for lower power devices (<1 watt) to \$40-50K for the highest power devices (20-30 watts). The higher power devices that are anticipated (50-100 watts) will range in cost from \$100-200K or even higher. Thus the normalized cost of near-term excimer laser equipment is approximately \$2,500/watt of laser output in the 10 to 100 watt range. The wavelengths available are 193, 248, 308, and 351 nm. For purposes of this cost analysis, an equipment cost of \$25,000 for an XeCl configuration is assumed.

##### b. Laser Operating Costs

There are three principal cost elements associated with excimer lasers: the consumption of excimer laser gas, the use of electricity and other utilities, and scheduled maintenance to replace or repair short lifetime components. Typical costs per watt-hour of excimer laser output are \$0.05 (ArF or XeCl) to \$5.0 (KrF) for laser gas, \$0.02 to \$0.05 for electricity, and \$0.2 to \$2.0 for scheduled maintenance. Reduction of gas consumption and maintenance costs is one of the critical development steps

required for the successful application of excimer laser technology to solar cell fabrication.

Recent promising developments in the United Kingdom in the area of excimer gas on-line reprocessing have demonstrated significant reductions in gas replenishment frequency, especially for ArF. A reduction of 20:1 in gas consumption is assumed in this cost estimate.

In the area of maintenance, the principal driving costs involve frequent refurbishment and replacement of internal parts affected by the excimer gas and the high switching pulse loads on the thyatron. In particular, efficient laser operation requires complete teardown of the laser optical system about every  $1 \times 10^8$  shots. This is approximately once a week for the application discussed here.

During the maintenance, which requires about four hours, the electrodes are refurbished, a new cathode screen is installed, the anode surface is refinished (buffed), and all uncoated internal optical surface flats are reground and polished. Approximately every 4th weekly maintenance, most of the above described components are replaced. An additional six hours are required every six weeks ( $1 \times 10^9$ - $10$  shots) to disassemble and replace the thyatron, which costs \$2,200. As a result of this very high maintenance level, the direct material costs reflected in the summary tables are higher than desirable. As experience is gained in using these lasers in high production mode applications, operating and maintenance strategies can be expected to evolve that will reduce these costs.



## SECTION 7.0 CONCLUSIONS

Solar cell fabrication by utilization of an excimer laser in junction formation, fine gridline metallization, and surface passivation has been investigated. Junction formation by laser annealing showed as good, if not better, quantum efficiency on the average as thermally diffused cells because of the shallow and sharp gradient in the dopant profile. The best efficiency obtained was about 16% at AM1.5. A higher efficiency may be obtainable from a more uniform laser that requires no homogenization plate. The results obtained in this study using Cz material are comparable to those obtained in the studies using FZ material. Also shown was that homogeneous beams with small spot size give comparable results with large beam sizes. Surface passivation by laser assisted silicon oxide deposition has yet to be shown to be effective. However, both processes of oxide deposition and junction formation by excimer laser have the potential to be applied in integrated circuit fabrication of shallow junction devices. They can provide a truly cold process in junction diffusion and preserve the bulk minority carrier lifetime. Junction depth and oxide thickness can be specifically tailored by varying the laser energy density.

Because of excellent spatial resolution of the laser, both diffusion and oxide deposition can be selectively accomplished in area, an asset that thermal diffusion lacks.

Fine gridline metal deposition by excimer laser, on the other hand, is found not to be feasible yet for solar cell production.

The final recommendation based on the results of this study is that laser assisted cell processing requires more research before it can be implemented in low cost solar cell production.

## REFERENCES

1. List of some publications on the subject of laser annealing:
  - a. Harold Hovel. Semiconductors and Materials 2, 40, 1975.
  - b. Lockheed Quarterly Report No. 2, JPL Contract 955696, 1980.
  - c. A.G. Cullis, D.T.J. Hurle, H.C. Webber, N.G. Chew, J.M. Poate, P. Baeri, and G. Foti. "Growth Interface Breakdown During Laser Recrystallization From the Melt." Appl. Phys. Lett. 38 (8), 642, 1981.
  - d. R.T. Young, G.A. van der Leeden, J. Narayan, W.H. Christie, R.F. Wood, D.E. Rothe, and J.I. Levatter. IEEE Electron Device Letters, EDL-3 (10), 1982.
  - e. R.T. Young, G.A. van der Leeden, R.L. Sandstrom, R.F. Wood, and R.D. Westbrook. Appl. Phys. Lett. 43 (7), 666, 1983.
  - f. S.R. Wilson, W.M. Paulson, R.B. Gregory, G. Tam, C.W. White, B.R. Appleton, A.K. Rai, and P.P. Pronko. "Thermal Stability of Electrically Active Dopants in Laser Annealed Silicon Films." J. Appl. Phys. 54 (9), 5004-13, Sept. 1983.
  - g. R.T. Young, J. Narayan, W.H. Christie, G.A. van der Leeden, J.I. Levatter, and L.J. Cheng. "Semiconductor Processing with Excimer Lasers." Solid State Technology, 26 (11), 183-9, Nov. 1983.
  - h. Robert Campbell. Westinghouse report presented at JPL Project Integration Meeting, 1984.
2. K.N. Tanner and A.B.F. Duncan. J. Am. Chem. Soc. 73, 1164, 1951.
3. D.J. Ehrlich, R.M. Osgood, Jr., and T.F. Deutsch. IEEE J. Quant. Electron. OE-16, 1233, 1980.
4. P.K. Boyer, G.A. Roche, W.H. Ritchie, and G.J. Collins. Appl. Phys. Lett. 40, 716, 1982.
5. Y. Miahim, M. Hirose, Y. Osaka, Y. Ashida. J. Appl. Phys. 55, 1234, 1984.
6. S.D. Allen. Proceedings of the Materials Research Society Symposium, Vol. 17, pp. 207, 1983.

7. JPL, "Interim Price Estimating Guidelines: A Precursor and an Adjunct to SAMIS III Version One." JPL 5101-33, September 10, 1977.

## ACKNOWLEDGMENTS

The authors would like to thank Dorothy Houk, Mari Kristiansen, Evelyn Greenwood, and Mary McLaughlin for their assistance in report preparation. The sponsorship of JPL who made the project accomplishable is also greatly appreciated. Technical discussions with Douglas Lowndes of Oak Ridge National Laboratories were beneficial to the project progress.

The authors would also like to thank Frank Ho of ASEC and Mark Spitzer of Spire Corporation for their generous technical assistance.